Citation for published version

Melle-Franco, Manuel (2000) Computer simulation of ionic solids of technological interest. Doctor of Philosophy (PhD) thesis, University of Kent.

DOI

https://doi.org/10.22024/UniKent%2F01.02.94525

Link to record in KAR

https://kar.kent.ac.uk/94525/

Document Version

UNSPECIFIED

COMPUTER SIMULATION OF IONIC SOLIDS OF TECHNOLOGICAL INTEREST

A THESIS SUBMITTED TO
THE UNIVERSITY OF KENT AT CANTERBURY
IN THE SUBJECT OF CHEMICAL PHYSICS
FOR THE DEGREE
OF DOCTOR OF PHILOSOPHY.

By
Manuel Melle-Franco
July, 2000

Dedicated to Dad, who would not believe his eyes, Mum and Angeles.

May the Force be with You

Obi Wan Kenobi

Contents

List of Figures

List of Tables

Memorandum

The work presented in this thesis has been carried out at the Centre for Materials Research of the University of Kent at Canterbury, UK, the Physics department of the University of the North, South Africa, and the Materials Science department of the University of Milano-Biccocca, Italy, between November 1996 and April 2000 under the supervision of Professors A.V.Chadwick and G. Pacchioni.

The contents are the results of some original research by the author. No part of the material submitted has previously been submitted by the candidate for a degree at this or any other University. Where use has been made of the results and conclusions of other authors in relevant studies, the source of the information has been clearly indicated, unless the information is of such a general nature that indication would be impractical.

Manuel Melle-Franco

Acknowledgments

My most sincere thanks to the two people that has supervised me in these years; Professors Alan V. Chadwick and Gianfranco Pacchioni. I cannot find words that can express my gratitude to any of them. Without their patience, guidance, advice, help, and friendship this thesis would not be here.

The rest of the academic acknowledgments go to: Dr. Grant Morrison for good, although unfortunately short, supervision. Dr. G.D. Becker and Prof. A. Aboukais for sending articles and good discussions. Prof. C.R.A. Catlow, Dr. M. Matsui, Dr. J. Harding and Prof. S. Parker for sending articles. Dr. J.D. Gale for support with GULP. The Chemistry Computational Working Party and EPSRC for computational time in central facilities. Prof. R.J. Newport and Prof. P. Ngoepe for allowing me to use their computational facilities and software. Dr. Kevin Kennedy, Dr. Raffaela Soave and Davide Ricci for some nice pictures.

Thanks to the Royal Society and the South African Foundation for Research and Development for funding my trip and my stay in South Africa and the European Union for funding this Ph.D. and my travel to Italy.

To all the people that have been so unfortunate as to share with me a working place, and friendship, in the UK: Gavin, James, Didier, Jacqui, Dave, Kate, Georgios, Georgina, Nuria, Mark, Mustafa, Steve, Kevin, all the people of the old department of Chemistry and the School of Physical Sciences at Kent University. Special thanks go to Gavin, James and Didier by kind hospitality in the last stages of this thesis.

To my Italian colleagues, che ancora mi prendeno in giro per il mio italiano: Raffy, Livia, Davider, Davidee, Fabiano, Chiara and Silvia. And all my friends in the department that have made my stay at Milano something I will always remember.

And, last but not least, to all the good friends that in all these places far from home in one way or another have been there, through the good and the bad times, and to the bit of luck that makes anything possible.

Preamble

This thesis has been written in Milano (Italy) in the months from April to July 2000. Our initial objective was to write around 100 pages in a way that the key calculations could be reproduced without much effort by anyone in the field. This we found to be impossible. If you happen to read this thesis and you are interested in further details please contact me (via any of my supervisors) and I will be happy to help you. One of the things we had to cut short were introductions. It has been reduced to the minimum possible, otherwise, due to the extension and the heterogeneous nature of the work presented would further increase the, already excessive, number of pages. We have in many cases also fallen into redundancy, in most of the cases this was due to a specific concern about clearness, that, anyway, we doubt, we reached.

And, well, this is it. This is the end of my trip and the beginning of yours.

Abstract

In the present study we have applied Quantum Mechanical (QM) and Molecular Mechanics (MM) computational methods to solid state materials of interest, specifically: metal hydrides, olivines, ceria and tin oxide crystals.

A new empirical potential set has been derived for the following metal hydrides; NaH, LiH, MgH_2, CaH_2 and BaH_2. Studies of atomic diffusion have been performed in LiH and CaH_2 and agree well with the available experimental data. MM simulations of cation diffusion in olivines have been performed. Diffusion has been found to come mainly from M_1-M_1 nearest neighbour jumps with a smaller contribution by site exchange, M_1-M_2 and M_2-M_1, jumps. The spatial exploration of non-linear diffusion paths has been shown crucial in order to yield correct estimations of the activation energy of diffusion. MM calculations of solution and clustering of Cu^{2+} in ceria show that, on the contrary to previous work, it is quite likely that the dopant enters in interstitials sites and, consequently all clusters observed experimentally may be formed by Cu^{2+} interstitials.

QM cluster and periodic slab simulations have been performed on the CO and CO_2 adsorption on the (110) perfect surface of SnO_2 with HF and DFT methods. These calculations show that, for CO, the molecule adsorbs on pentacoordinated cations on, ideal, truncated bulk, and relaxed surfaces. The interaction with the surface is mostly electrostatic and well described by uncorrelated methods. In the CO_2 case, the molecule adsorbs perpendicularly to the surface on the same site, but the main bonding contribution is the polarization of the CO_2 and DFT methods are necessary to properly describe the binding. Carbonates have been shown to be formed only as metastable species on the perfect (100) SnO_2 surface.

Part I

Introduction

Chapter 1

Interatomic Potentials

1.1 Bonding in solids

Most of the chemical elements and their compounds are solids at room temperature. The study of solids, and of all the factors which determine their structures and properties, forms a very important part of chemistry and physics.

Most solids appear as crystals, where the atoms or molecules are packed in regular arrays. The systems we will study are all crystalline, and relatively ionic. In order to understand some of the approximations undertaken in the use and formulation of interatomic potentials for ionic systems, it is necessary to have an idea of the bonding, or interactions they try to mimick.

1.2 Chemical classification of solids

From a chemical point of view, solids are most conveniently classified in terms of the kind of interaction which holds the component atoms or molecules together:

- Molecular solids (Xe, N_2, benzene)
- Ionic solids (NaCl, MgO, CaF_2)
- Covalent solids (Diamond, SiO_2)

- Metallic solids (Na, Fe, Cu).

1.2.1 Molecular solids

Molecular solids are composed of individual atoms or molecules which mainly retain their identity. In other words, the electron distribution of these atoms or molecules is very similar to the one they possess in the gas phase.

In the simplest case, non-polar atoms or molecules, the principal interaction is the van der Waals' dispersion force, which is an attractive interaction due to the dipole fluctuations arising from the correlation in the motion of electrons of neighbouring atoms. This interaction is completely non-directional and falls off very rapidly with distance. The main structural driving force for solids based on this interaction is the efficient packing of the molecules or atoms as closed as possible.

1.2.2 Covalent solids

Covalent bonds are very directional. In a very general definition, covalent bonds can be seen as a very localized enhancement of the electron density that depends strongly on the relative 3D position of the contributing atoms. The structure of solids based on this interaction might be seen as a very large covalent lattice, for instance diamond or quartz (SiO_2), where atoms are held together by covalent bonds which are essentially similar to those in small molecules and, therefore, the resulting structures are determined by the same factors that determine the structure of gas phase molecules.

1.2.3 Ionic solids

Ionic solids are ideally composed by electronegative and electropositive atoms, which when brought together, exchange electrons to form positive and negatively charged ions. The ions of opposite sign are strongly attracted by a Coulomb electrostatic potential while same sign ions are strongly repelled, most of the binding in ionic solids is made up of electrostatic interactions. This Coulomb interaction falls off very slowly imposing the long range ordering observed. In very ionic systems, the charge distributions obtained are mostly spherical[1] and Pauli exclusion principle makes up for the short-range repulsive interaction that effectively separates the ions. In these systems, the equilibrium anion–cation distance is mainly determined by the balance between these two factors.

1.3 Interatomic potentials

1.3.1 Introduction

Interatomic potentials are a crude approximation to the Quantum Mechanical (QM) reality of the interaction between atoms. This is possible, as in most QM calculations, due to the Born-Oppenheimer approximation that considers the electronic and nuclear motion of atoms completely uncoupled. The Born-Oppenheimer function, i.e. the time-independent Schrödinger function of the electrons with fixed nuclei for all the nuclei and electrons of the system can be considered as a many-body global energy.

Classical mechanics describes the energy of a thermodynamically isolated assemble of N interacting particles, with a N-body energy. This energy can be decomposed into a series of terms containing the different N-body parameters, which may be written:

$$E(1,...,N) = \sum_{i} E(i) + \sum_{i,j} E(i,j) + \sum_{i,j,k} E(i,j,k,) + ... \tag{1.1}$$

The first term can be assumed to be constant in all the simulations that do not deal with the intrinsic energy of any single particle or its kinetic energy and since we are not interested on the calculating of the global energy of a system, but the different energies of interaction for different configurations of particles, its

---

[1] Closed shell free atoms show spherical symmetry.

presence can be neglected.

In the generic values expected from this equation, the differences between non-covalent bonded[2] and bonded materials arise again. In non-covalent bonded systems, the terms of order three and higher, can be truncated since the pair term is expected to be the dominant contribution to the binding energy. In systems with covalent bonding on the other hand, higher order terms may be crucial to model the material.

1.3.2 Pair and three body potentials

For non-polar van der Waals solids and strongly ionic materials, the order two term will, mainly, determine the final value of the N-body energy, and we can approximate these systems with an effective[3] two body potential.

In the simplest model, atoms are consider as point particles whose interaction is defined with a relatively simple function or a sum of simple functions.

One of the short-range elementary potentials that has been more widely used, specifically in ionic solids and simple liquids, is the Buckingham potential. This potential tries to mimick the interaction between two closed shell atoms i and j and corresponds to the following function:

$$\phi(r_{ij}) = A_{ij} \cdot exp\left(\frac{-r_{ij}}{\rho_{ij}}\right) - \frac{C_{ij}}{r_{ij}^6} \tag{1.2}$$

where r_{ij} is the distance between the i^{th} and j^{th} particles, and all the other terms are constants.

The first, exponential term, generally called the Pauli term, reflects the fact that the repulsion is largely determined by the overlap of atomic wave functions (i.e. atomic orbitals) which at large distances from the nucleus show an exponential radial dependence, and that dominate, as the equation shows, at shorter distances.

---

[2] We refer here as non-covalent bonded materials only to van der Waals and ionic solids.

[3] Strictly, the terms obtained by only considering the two body potential have not to be equal to the terms obtained for the N-body potential in the two body terms.

The second term models the attractive dispersion interaction or, more commonly called, van der Waals interaction. This is a universal atomic weak interaction occurring between closely spaced atoms, that arises from electronic correlation effects in the non-homogeneous, in time, spatial distribution of the electrons surrounding the nucleus of an atom. These fluctuations have an effect on the surrounding atoms electronic structure, changing their distribution from the equilibrium.

In simpler terms, we can say that the uniform charge distribution can be distorted, creating a momentary dipole which interacts with the electrons of a near atom, disturbing its charge distribution, and inducing a dipole of complementary orientation resulting in a net momentary attraction between the two dipoles. The fluctuating dipole moment varies rapidly in amplitude and orientation averaging an attractive interaction, that changes as a function of r_{ij}^{-6}.

In a, simpler, Lennard-Jones, LJ, potential, the exponential, repulsive, term, is replaced by an algebraic term:

$$\phi(r_{ij}) = \frac{A_{ij}}{r_{ij}^{n}} - \frac{C_{ij}}{r_{ij}^{6}} \tag{1.3}$$

Where n= 8–10 is used for ionic systems, while n=12 for liquids. The first term of the LJ potential, A_{ij}/r_{ij}^{n}, is just a pre-computational era approximation to the exponential Pauli term[4] and consequently the values of n will steeply depend on interatomic distance. This potential has been widely used in the modeling of simple atomic liquids. One of the early successes in computer modeling was the surprisingly good description attained for argon, not only the equilibrium averages as radial distribution function, but dynamic, processes as diffusion, were close to the values observed experimentally [1].

However, these potentials although giving relatively accurate descriptions of many properties cannot fully describe the system, and, for instance, a model for argon that could, accurately, describe more than one phase, had to be derived

---

[4] In those days an exponential was more difficult to evaluate numerically than a power term.

based on the analysis of many experimental results from a wide variety of techniques over gas and solid phases that allowed the very accurate BBMS17 potential, whose functional form is considerably more complex [2], to be developed.

In fully ionic solids, the interaction energy of two atoms can be written as the addition of the long range Coulombic interaction plus the short range interactions described by the Buckingham potential:

$$V(r_{ij}) = \frac{Z_i Z_j e^2}{r_{ij}} + A_{ij} \cdot exp\left(\frac{-r_{ij}}{\rho_{ij}}\right) - \frac{C_{ij}}{r_{ij}^6} \tag{1.4}$$

where Z_i is the i^{th} particle charge, equal to the formal charge of the i^{th} ion in an ionic solid, and e is the charge of the electron.

When modeling ionic solids, at equilibrium distances the Coulomb interaction is at least one order larger in magnitude than the resultant of the short range terms. Close to zero distances, the exponential term tends to A, the pre-exponential value, and, the dominant term is mainly the dispersion term which makes the energy tend to minus infinity. However, in most cases, there is a barrier that prevents the atoms in the model to collapse on each other. It is important to check consequently that all the interactions have the proper curvature. This is the two body potential form used in all of the presented, Molecular Mechanics (MM) studies.

1.3.2.1 Three body potentials

The three body potential represents one possible way to include the directionality of the bonding in relatively covalent systems, like SiO_2 [3]:

$$V_{(3-body)} = \frac{1}{2}k \cdot (\theta - \theta_0)^2 \tag{1.5}$$

where k is a harmonic spring constant, and θ and θ_0 are the particles three-body angle, and the reference three-body angle, respectively. This three body potential allows us to introduce a penalty energy deviation, as a constraint, over the bond angles in the range of, relatively narrow, permitted values of covalent solids. This potential will only be used in this thesis on magnesium and iron silicates however its presence, at least in these systems, it is not fundamental to describe the structures which can be described very well by two body potentials alone [4].

1.3.3 Rigid and core-shell ions

The rigid ion model is the most simple way to model with MM an ionic crystal. Basically the atoms are considered point charges that interact via equation 1.4. The Short Range (SR) potentials are calculated for all the distances under a user defined cutoff, typically in the range of 10 Å, while the long range Coulomb interaction, which is only conditionally convergent in real space, is treated with an Ewald summation [1].

The rigid ion model, although fairly successful in many applications does not include the possibility of polarization, i.e. distortion of the electronic clouds, of the atoms. This lack, implies that easy to measure experimental properties and calculation of defects energies according to the Mott-Littleton model [5] in which partial polarization of the atoms may have a vital contribution have to be ignored.

The core-shell method established by Dick and Overhauser [6] tries to overcome this problem. The ion is represented by two particles, a core with subsumes all the mass of the ion surrounded by a massless shell linked to it by an harmonic spring. The charges of core and shell are different and can be obtained based on free polarization formulas or fitted to high frequency dielectric constants. The sum of core and shell charges constitutes the charge on the ion. In absence of a net polarizing electric field both particles are concentric, fig.1.1.

When the ion is polarized, the shell is displaced on the direction of the polarizing field until until the energy is minimized according to the following equation:

$$E_{(core-shell)} = \frac{1}{2}k \cdot r^2 \tag{1.6}$$

where k is a harmonic spring constant, and r is the distance between core and

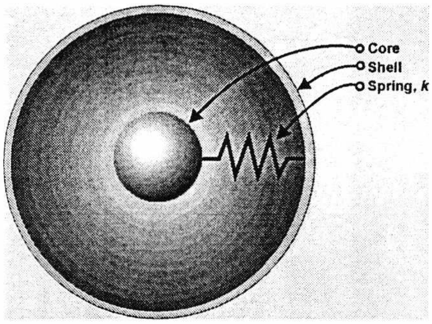

Figure 1.1: Core-shell model

shell.

Although this model can be conceptually interpreted with the core representing the nucleus and the inner core electronic orbitals, while the shell represents the electronic outer orbitals, there is not any physical evidence supporting this. This is a phenomenological model [7].

The SR atomic interactions in this model, as supposed arising from interactions between electronic clouds of the neighbouring atoms, are only applied over the shells while the long-range Coulomb interactions are applied over cores and shells. This allows the decoupling of SR and core-shell interactions.

The core shell model can approach the model of a significantly covalent material using an intrinsically ionic model, modeling the covalency as a localized vectorially opposed polarization between the two atoms. This may be of special interest when the ionicity of a system, its characteristic physical charges, are not even approximately known and formal ionic charges may be assumed to try the modeling [8].

1.4 Molecular mechanics software

1.4.1 Introduction

All of the MM bulk static simulations and interatomic potential development presented in this work have been performed with the General Utility Lattice Program, GULP [9]. GULP performs calculations on 3D periodic solids considering fully the underlying symmetry of the modeled crystals. Although, it can also do Molecular Dynamics, MD, and free energy calculations under the quasi-harmonic approach, it is mostly used to calculate static energy minimizations of crystal structures and properties based on interatomic potentials. GULP can also be used to fit potentials to experimental data by least square fitting to experimental properties and crystal structures.

1.4.2 Interatomic potentials development

When considering the developing of empirical, or *ab initio* obtained, interatomic potentials, a good starting point comes from understanding that, as pointed out by Stoneham [7], an interatomic potential always exists, since there is always an underlying *real* interatomic interaction. However this *real* interaction may be better or worse accounted for, or reproduced, by the chosen potential functions and parameters.

Interatomic potentials may be fitted to *ab initio* obtained data or to experimental data (or to both). Fitting to *ab initio* data implies the prior calculation of energies of different spatial configurations of the system with an *ab initio* method. Although this can be quite expensive computationally, it has the advantage, compared to empirical fitting, that it allows the potentials to be fit to specifically biased regions of configurational space that can be chosen as a function of the problem. Consequently, they can be far more representative when suitable experimental data is not available.

In contrast, empirical fitting implies fitting the potentials to experimental structures and, when available, elastic constants and low and high frequency dielectric constants[5]. Cohesive energies may also be introduced in the fit, however in many systems they are not easy to fit. Also, the meaning of these fits in non-ionic

---

[5] Ideally phonon frequencies can be also fitted, but, there is not any certainty that each frequency would correspond to the correct normal mode and seems to be only practical in cases where the frequencies are effectively separated or can be easily identified [10].

systems, assuming formal charges, is obviously wrong.

All static calculations are athermal, in the 0 K approximation, and therefore all the experimental data should be, ideally, at the lowest possible temperature. Unfortunately, most experimental data are taken at room temperature, resulting in most cases, in a model that effectively is a temperature weighted average of the properties of the crystal [8].

The fitting to the structure defines mostly where the most stable local configuration should be (i.e. the balance between Coulomb, fixed, and SR potentials), while the elastic and dielectric constants, define the curvature of this minimum. This, in relatively symmetric structures[6], constrains the fitting to a relatively small region of configurational space, which implies an uncertainty in the applicability of the derived potentials to not very similar atomic configurations. For instance, in point defects calculations, where interatomic distances which are not, and cannot be, included in the potential fitting are sampled [11].

The number of simultaneously fittable potential parameters, i.e. variables, is equal to the number of independent observables which depends on structure symmetry and available properties. It can be as low as one in the very symmetric rock-salt structure. Although, the lifting of the symmetry constraint would allow an increase in the number of fittable variables, since the crystal structure can be generated based on only one observable, fitting more than one variable at a time would result in an overfit, i.e. like fitting a parabola to a point. This strongly constrains the fit, and the simultaneous fit of all the potential variables may imply the introduction of other structures with, at least in principle, similar bonding and/or crystal properties.

In contrast, a full set of potentials can be fitted simultaneously to medium-low symmetry structures, for which, usually, properties are not available. Although the potential set may show minima that may be very structure dependent, it may

---

[6] Buckingham potentials have spherical symmetry, so statically the space-group symmetry constraint allows a reduction in the number of variables reducing consequently CPU and memory use.

also show more generality of application due to the higher number of different distances that are sampled.

Asymmetry usually implies a relative degree of covalency in crystal bonding that may not be very well described by a purely ionic model. In these cases, a dipolar core–shell model might be crucial in order to absorb the covalency.

1.4.2.1 Gradient versus relaxed fitting

Fitting *empirical* potentials in GULP can be performed in two different ways:

- Gradient fitting: the potentials fitted try to minimize the gradients of energy with respect to the atomic coordinates[7] for the experimental structure.
- Relaxed fitting: the potentials fitted try to minimize the displacements of structural parameters, rather than the gradients, with respect to the experimental structure. In this case the structure is relaxed on each step, so the properties of the relaxed geometry, according with the current optimizing potentials, are fitted.

Relaxed fitting is more expensive computationally and needs to be started from partially refined potentials. Gradient minimizations are rather more robust, however in asymmetric structures they do not normally yield very good results.

Typically, potential fitting is first approached by a gradient fitting with potentials from a similar system, to be further refined by a relaxed fitting in order to obtain the final set of potentials.

1.4.3 Transferable potentials

The use of a common potential for more than one system implies assuming that this potential is transferable between both systems. Really what is in doubt is

---

[7] In a crystal at an ideal static equilibrium, all symmetry independent gradients of energy with respect to coordinates should be zero.

not that the modeled potential may be transferable but that the interactions in the two systems are similar enough to be treated, or approximated, by the same function and parameters. Regarding this matter some general points should be highlighted:

- Self-consistency implies that potentials from different parameter sets, where common potentials are different, are not interchangeable.
- All potentials should be carefully tested in the systems they have been calculated from prior to any use in new systems. The field of interatomic potential development spans more than 30 years. Different short range cutoffs or short range interaction treatment, fixed volume optimizations, different convergence criteria, etc, may cause a more than negligible discrepancy in perfect crystal results and the potentials parameters may need to be readjusted.
- Interatomic potentials for the very same structure/s have been developed and compared. In some cases, in spite of being all but different exponents of an approximation to the same *real* interaction they have been shown not only to quantitatively diverge but also to qualitatively differ [11]. This shows clearly the complexity of potential variables space and the need for certain care in all preliminary calculations.

A common potential fitting should, *a priori*, approach better, within the limitations of the model a possible common *real* interaction. Tests in this respect have been developed and embodied in the, to our knowledge, novel multifit method.

1.4.4 Multifit method

Potential fitting, as any minimization routine applied to a physical problem, presents a number of specific limitations:

- Local minima.

- A better minimization factor[8] but not necessarily a better reproduction of experimental values.

The minima obtained with asymmetric structures normally depend strongly on the very initial guess points (initial values of potential parameters to optimize). The availability of reasonable initial guess points[9] for relaxed fitting is a very limiting factor in the development of potentials.

Standard minimization procedures must start from relatively good guess points, non-standard procedures comprise the Genetic Algorithm (GA) search methods. These are search algorithms for a minimum where a number of simultaneous search parameters are mixed and randomly changed in order to evolve to a minimum. These were tried in systems where potentials were difficult to fit with the standard procedures, namely $PbBr_2$, α-PbF_2, $PbCl_2$, without success. GA, as implemented in GULP [10] can only evolve based on gradient minimizations[10], however it is only needed when gradient fits cannot not reach any further refinable potential set.

In order to tackle these or similar problems we have developed and implemented what we call the multifit method. The idea underlying the method is quite simple; an external program generates different starting potential parameters on a user specified grid. The potentials are fitted (relaxed or gradient fitting) starting from each different single point. Once all the runs are finished, other programs order and filter the results by a factor that compares calculated observables with experimental ones and automatically prepare the best files for further refinement.

This method, as GA, in an infinite number of steps will reach the global minimum, but it is far more flexible; all the runs are *simultaneous*, in the way that they are done completely independently, and therefore unstable minimizations/fittings

---

[8] In our case the square of the difference between input experimental properties and structural parameters and the ones calculated by the model.

[9] From systems where the interactions are supposed to be fairly similar.

[10] Since relaxed minimization from potentials that have not been partially refined tends to stop abnormally breaking the evolution line.

do not affect the "evolution" to the final result.

The multifit method intrinsically allows us to explore the parameter fitting space and extract, qualitative and quantitative information of its complexity. However, the dimensionality of space has to be reduced and, therefore chosen carefully. Practical grids are relatively coarse since the number of runs scales to the power of number of parameters in the grid. For instance, a typical exploration, around 6000 simulations corresponds only to 8 intervals (9 values) of 4 changing parameters. Coarse exploratory griddings can be done in order to see the correlation of parameters with fitting factors and once the most promising ranges are obtained these can be further explored with a finer grid interval.

The advantages of the multifit method are:

- Very flexible and fully parallelizable.
- Gives an idea of the complexity of potential space.
- Reduces the bias of initial values for the fitting.
- Yields direct numerical evidence of the transferability of potentials.
- Allows a systematic exploration of parameter space.

The disadvantages are:

- Very bad scaling.
- It can be lengthy and time consuming.

Chapter 2

Quantum Mechanical Techniques

2.1 Introduction

Within the so-called first principles calculations, there are many methods, modifications, parameterizations, algorithms, programs, etc. In this chapter we try to make an extremely general introduction to the most widely used molecular orbital quantum mechanical methods, specifically Hartree-Fock and Density Functional Theory methods, since they have been used quite extensively in all the quantum mechanical calculations presented in this work. More detailed information can be found, for instance, in [12] (Hartree-Fock) and [13] (Density Functional Theory).

2.2 The Hartree-Fock Method

The energy and other observables of a physical system can be computed by solving the Schröndiger equation which, for the case of a potential independent of time, can be written as:

$$H\psi(x) = E\psi(x) \tag{2.7}$$

Where H is the Hamiltonian operator given by the sum of the kinetic and potential energies, H=T(X) + U(x), $\psi(x)$ is the wave function and E is the energy eigenvalue of the state $\psi(x)$.

Neglecting relativistic effects, the Hamiltonian for a system of M atoms and N electrons can be written in the following way:

$$H = -\frac{1}{2}\sum_{i=1}^{N}\nabla_i^2 - \frac{1}{2}\sum_{A=1}^{M}\frac{1}{M_A}\nabla_A^2 - \frac{1}{2}\sum_{i=i}^{N}\sum_{A=1}^{M}\frac{Z_A}{r_{iA}} + \frac{1}{2}\sum_{i\neq j}^{N}\frac{1}{r_{i,j}} + \frac{1}{2}\sum_{A\neq B}^{M}\frac{Z_A Z_B}{r_{AB}} \qquad (2.8)$$

where Z_A is the atomic number of the nucleus A, M_A is the mass of the nucleus A, and r is the distance between electrons (ij), nuclei (AB) and an electron and a nucleus (iA).

This Hamiltonian operator includes, from left to right, the kinetic energy of electrons and nuclei, and the potential energy operator for the Coulomb interactions among all particles (specifically: electron-nucleus, electron-electron and nucleus-nucleus). Solving equation 2.8 poses a complex problem. However, since the mass of the nuclei is much larger than that of electrons and in fact their motion is much slower, it can be assumed that the electrons distribution responds instantaneously to any motion of the nuclei, an consequently both motions can be uncoupled. This approximation is known as the Born-Oppenheimer approximation and is present in almost all quantum mechanical methods used to date. For each configuration of stationary nuclei one has to solve the eigenvalue equation:

$$H^{elect}\psi(1,2,...,N) = E\psi(1,2,...,N) \qquad (2.9)$$

2.2.1 Hartree self-consistent field

Equation 2.9 can be transformed into the sum of N one electron Schröedinger equations. Each one of the N solutions is the wave function of a single electron subject to the field created by the M nuclei and the remaining N-1 electrons. The many-body wave function $\psi(1,2,...,N)$ can be expressed as the product of the single electron wave functions:

$$\psi(x_1, x_2, ..., x_N) = \prod_1^N \phi_i(x_i) \tag{2.10}$$

To obtain a complete solution it is necessary to derive the $\chi_i(x_i)$ which are solutions of the single one electron equations:

$$H_i^0 \phi_i(x_i) = \varepsilon_i \phi_i(x_i) \tag{2.11}$$

$$\left[h_i^0 + V_i^{eff}\right] \phi_i(x_i) = \varepsilon_i \chi_i(x_i) \tag{2.12}$$

Where H_i^0 is the Hartree operator, and h_i^0 contains the kinetic term and the nuclear term interactions and:

$$V_i^{eff}(x_i) = \sum_{j \neq i}^{N} \int \frac{\phi_j^*(x_i) \cdot \phi_j(x_i)}{r_{|i-j|}} dx_i = \sum_{j \neq i} \left\langle \phi_j^*(x_i) | \frac{1}{r_{|i-j|}} | \phi_j(x_i) \right\rangle \tag{2.13}$$

represents the Coulomb interaction between the two electronic distributions.

For atoms with closed-shell electron configurations the potential can always be expressed in spherical symmetry. It is possible then to assume that the orbitals are the product of a fixed spherical harmonic function (the shape of the orbital) and an adjustable radial part (its spatial extension). In order to solve the problem, assuming we have chosen appropriate functions, we just have to find the values for the radial part of all the one electron wave functions solutions to eq. 2.12. However, the V_i^{eff} depends on the orbitals, $\phi_i(x_i)$, and to derive these orbitals an iterative process is needed; from an appropriate zero-order approximation of the orbitals, $\phi_i^{(0)}(x_i)$, a first approximation of the Coulomb interaction is obtained which gives a first approximation of the Hartree operator H_i^1. Solving the N equations with these quantities a new set of orbitals, $\phi_i^{(1)}(x_i)$, is obtained, the process is repeated until self consistency is achieved:

$$H_i^n \simeq H_i^{n+1} = H_i^{SCF} \tag{2.14}$$

$$\phi_i(x_i)^n \simeq \phi_i(x_i)^{n+1} = \phi_i(x_i)^{SCF} \tag{2.15}$$

At this point, the orbitals, i.e. the electronic charge distribution, produce a self-consistent field (SCF). The total energy of an N-electron atom in the Hartree SCF approximation is given by the expectation value of the exact Hamiltonian, not the SCF Hamiltonian, with the wave function constructed with the product of the self-consistent Hartree orbitals. The role of the SCF Hamiltonian is only to generate the SCF atomic orbitals, the total energy of the system is:

$$\langle H\rangle = \langle\psi|h^0 + \sum_{i<j}^{N}\frac{1}{r_{ij}}|\psi\rangle = \langle h^{(0)}\rangle + \sum_{i<j}^{N}\Big\langle\frac{1}{r_{ij}}\Big\rangle \tag{2.16}$$

For normalized SCF orbitals one has:

$$\langle h^{(0)}\rangle = \sum_{i=1}^{N}\langle\phi_i(x_i)|h_i^0|\phi_i(x_i)\rangle = \sum_{i=1}^{N}\varepsilon_i^{(0)} \tag{2.17}$$

where $\varepsilon_i^{(0)}$ is the energy of a single electron in the nuclear potential. The second part of the total energy is given by:

$$\Big\langle\frac{1}{r_{ij}}\Big\rangle = \sum_{i<j}^{N}\Big\langle\phi_i(x_i)\phi_j(x_j)|\frac{1}{r_{ij}}|\phi_i(x_i)\chi_j(x_j)\Big\rangle = \sum_{i<j}^{N}J_{ij} \tag{2.18}$$

where J_{ij} is the coulomb integral that represents the electrostatic energy due to the interaction of the two charge distributions $|\phi_i(x_i)|^2$ and $|\phi_j(x_j)|^2$. The total Hartree-SCF energy can be expressed as:

$$E = \sum_{i=j}^{N}\varepsilon_i^{(0)} + \sum_{i<j}^{N}J_{ij} \tag{2.19}$$

2.2.2 Electron-electron interaction

Electrons are fermions and as such any wave function describing them has to behave according the antisymmetry principle. This states that on any interchange of electrons the wave function has to change sign. This is a consequence of the Pauli exclusion principle. A Slater determinant satisfies this principle:

$$\psi = \frac{1}{\sqrt{N!}} \begin{vmatrix} S_1(1) & S_1(2) & ... & S_1(N) \\ S_2(1) & ... & ... & ... \\ ... & ... & ... & ... \\ S_N(1) & S_N(2) & ... & S_N(N) \end{vmatrix} \tag{2.20}$$

where $S_i(i)$ are spin-orbitals, product of a spatial and a spin part. With a wave function of this type, to the energy obtained with the Hartree method has to be added an exchange term, K_{ij}, with no classical analog which takes into account the Pauli principle:

$$K_{ij} = \left\langle \phi_i(x_i)\phi_j(x_j)|\frac{1}{r_{ij}}|\phi_j(x_j)\phi_i(x_i) \right\rangle \tag{2.21}$$

The implementation of this method is due to Fock and the energy which is obtained with the Hartree-Fock approach is therefore:

$$E = \sum_{i=j}^{N} \varepsilon_i^{(0)} + \left[\sum_{i<j}^{N} J_{ij} - \sum_{i<j}^{N} K_{ij} \right] \tag{2.22}$$

A Fock operator, f, can be constructed considering this, and the function to minimize is:

$$\langle \psi_0 | f \psi_0 \rangle \tag{2.23}$$

with the orthonormality constraint

$$\langle S_i | f S_j \rangle = \delta_{ij} \tag{2.24}$$

This leads to the set of equations known as the Hartree-Fock equations,

$$f(1) S_i(1) = \varepsilon S_i(1) \tag{2.25}$$

The Hartree-Fock equations are aimed at the determination of a set of one-electron wave functions, $S_1, ..., S_N$ which define the best possible approximation of the ground state in terms of the Slater determinant, eq. 2.20.

The Hartree-Fock method treats exactly, without any approximation, the exchange correlation but does not explicitly consider the electron correlation. This is a serious limitation in many applications. To introduce electron correlation effects one can correct the results obtained at the HF level using various techniques, like perturbation theory and the configuration interaction approach, or DFT methods.

2.3 Correlated Methods

In the SCF approach the electrons move in the average potential of the nuclei and of the other $n-1$ electrons so that the model cannot account for the fact that the instantaneous position of one electron is affected by the vicinity of other electrons. Actually, this is the basis of the van der Waals interaction, sect. 1.2.1, whose effect increases the interaction energy between atoms and is the origin of, for instance, the formation of solids of noble gases.

The energy due to electronic correlation is defined as the difference of the exact non-relativistic energy of the system, ε_0 and the HF energy E_0 obtained in the limit of a complete basis set:

$$E_{corr} = \varepsilon_0 - E_0 \tag{2.26}$$

The correlation energy is thus negative since E_0 represents an upper bound for the exact energy.

2.3.1 Density Functional Theory

Hohenberg and Kohn [14] proved that ground state energy, wave function and all other electronic properties are uniquely determined by the electron density $\rho(x, y, z)$. Consequently, if we know the ground-state electron density $\rho(r)$, it is possible to calculate all the electronic properties from ρ alone. This theorem, however, does not tell how to calculate the E_0 or how to find ρ without first finding the wave function ψ. Kohn and Sham [15] showed that the exact ground state energy E_0 with density ρ is given by:

$$\begin{gathered} E[\rho_0] = T[\rho_0] + \int \rho_0(r)v(r)dr + \\ +\frac{1}{2}\int\int \rho_0(r)V(r,r')\rho_0(r')drdr' + E_{xc}[\rho_0] \end{gathered} \tag{2.27}$$

where the exchange correlation energy $E_{xc}[\rho_0]$ is explicitly present. The electron density is described by means of the Kohn-Sham orbitals as:

$$\rho(r) = \sum_{i=1}^{n} |\psi_i|^2 \tag{2.28}$$

The Kohn-Sham orbitals are found by solving one-electron Kohn-Sham equations (formally similar to the Hartree-Fock equation):

$$\left[-\frac{1}{2}\nabla_i^2 + V_i^{eff}\right]\psi_i(r) = \varepsilon_i\psi_i(r) \tag{2.29}$$

The V^{eff} term is a one body effective potential which contains the interaction term with the external potential, the Hartree potential and the local exchange correlation potential V_{XC}.

The KS equations describe a system of n non-interacting electrons in an effective potential having the same electron distribution of the system under consideration. The Kohn-Sham orbitals have no physical significance other than in allowing the exact ρ to be calculated from eq. 2.28. Rigorously, their eigenvalues do not have the same physical meaning of ionization potential and electron affinity that they have in HF[1]. While the HF method is exact only in the treatment of the exchange, the DFT method is exact for both the exchange and the correlation terms provided that one knows the exact expression of the exchange

---

[1] Koopman's theorem.

correlation functional $E_{xc}[\rho_0]$. This form is not known and therefore approximations have to be introduced. The most widely used scheme for many years has been the so-called local density approximation (LDA) where it is assumed that at each point the exchange-correlation functional has the same form of that of an electron gas with the same (local) density. More recently, new approximations to the exchange functional have been introduced which take into account also the gradient of the spin density (Generalized Gradient Approximation, GGA). The GGA approach is essential for a correct description of quantities like the bond strength, the formation energy and in general all related thermodynamic quantities. Various forms of gradient-corrected exchange correlation functions have been proposed in the literature. The one which is largely used in this work is the Becke's three parameters hybrid non-local exchange functional [16] combined with the Lee-Yang-Parr gradient-corrected correlation functional [17] (B3LYP). The key theoretical concept in this functional is the role of exact exchange. Becke proposed that the mixing of exact exchange energy (as evaluated in HF theory) with that from LDA yields improved results and introduced a semi-empirical generalization to determine the extent of mixing of exact exchange based on fitting a series of thermochemical data on a series of molecules [16].

2.4 Basis sets

One of the methods to solve practically the eigenvalue equation

$$f(1)\psi_i(1) = \varepsilon_i\psi_i(1) \tag{2.30}$$

relies in the expression of the molecular orbitals $\psi_i(1)$ as a linear combination of a set of known basis functions, χ_i.

$$\psi_a = \sum_{i=j}^{K} C_{i,a} \cdot \chi_i \tag{2.31}$$

For $K \rightarrow \infty$ the basis will be complete and ψ_a will have the maximum accuracy of the method (the so-called Hartree-Fock limit). However, not only a finite number, but a certainly small one has to be used for any non-trivial size calculation. Consequently, the basis set chosen to adequately describe the molecular orbitals has to be selected with care.

2.4.1 Gaussian type orbital (GTO) basis sets

The molecular orbitals are generally described as Linear Combinations of Atomic Orbitals (LCAO). The atomic orbitals can be described by means of Slater functions which have a radial component that, for s type orbitals, is of the form:

$$e^{-\alpha r} \cdot r^{n-1} \tag{2.32}$$

However, the analytical form of this expression leads to difficulties in the calculation of the integrals so that usually Slater functions are expressed in terms of Gaussian type functions, $e^{-\alpha r^2}$, since the product of Gaussians is still a Gaussian this allows the integral evaluation at a much lower computational cost. When the basis set is formed of only one Gaussian per atomic orbital it is called *primitive* or *non-contracted*; when it is formed by a linear combination of more Gaussian functions, with fixed coefficients, it is called *contracted.* The use of more than one Gaussian in a contracted function gives a better description of the Slater functions. The simplest basis set is that in which, for the radial part, any Slater function is constructed with a contracted function with N Gaussians and the angular part is based on the spherical harmonics of the hydrogen atom. The family of basis sets so constructed is called Minimal STO-NG where N denotes the number of Gaussians for any contracted function.

The bigger the number of Gaussians, in principle, the better description of the system that may be attainable, as shown in fig. 2.20. In the STO-3G the number of Gaussians is fixed, so for systems in the right side of the Periodic Table (O, F) STO-3G sets are fairly inadequate for the description of valence electrons since

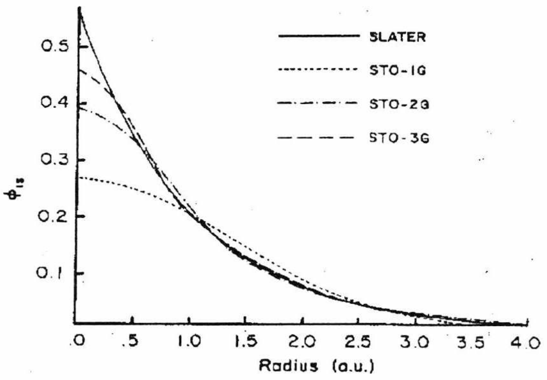

Figure 2.2: Description of a Slater function with the linear combination of one, two or three Gaussian functions

these sets are not flexible enough. This basis set can be improved by the addition of diffuse functions (with smaller coefficients, and larger radii) that alleviate this problems.

Gaussian functions are constrained to be centred on the nuclear positions. However, highly polar molecules require some allowance to be made for the possibility of non uniform displacements of charge away from the atomic centres [12], i.e. polarization. This is usually obtained by functions of higher angular quantum number that are needed by the atom in its electronic ground state, forming the so-called polarization basis sets.

2.4.1.1 Basis set nomenclature

The basis sets constructed by doubling the number of all the contracted functions of the minimal set are called Double Zeta (DZ), when tripled, triple zeta, etc. The basis sets doubling only the valence part of the basis set are called Split Valence (SV) and their name follows the following convention: L–NMG where L is the number of primitive Gaussians in the inner-core orbitals, and N and M are the number of primitives per orbitals in the valence shell for contracted and diffuse functions respectively. The addition of an extra diffuse function is denoted with "+" while a polarization function is denoted by a "*" [12]. For instance with a 6-31G any inner shell orbital is represented by 6 primitive functions while the contracted and diffuse functions are 3 and 1, respectively.

2.4.2 Basis Set Superposition Error, BSSE

The interaction energy of two interacting systems A and B can be calculated as follows:

$$E_{int.} = E(AB) - E(A) - E(B) \tag{2.33}$$

where $E(AB)$ is the energy of the system $A + B$, and $E(A)$ and $E(B)$ the energy of the isolated systems.

However, the fact that the number of basis set is finite, and usually incomplete, implies that under the LCAO approximation the binding energy will be partly overestimated. This is due to the fact that part of the difference in energy is not only due to the *real* interaction A–B but to the partial occupation of B basis sets by A electrons and vice versa due to incompleteness of the corresponding basis set, this is called Basis Set Superposition Error, BSSE. This overestimation can be partially accounted for by the Boys-Bernardi procedure, [18]:

$$E_{int.}(BSSE) = E(AB) - E(A + b.s.(B)) - E(B + b.s.(A)) \tag{2.34}$$

Where $E(A + b.s.(B))$ is the energy of the isolated fragment A with the Basis sets of B in the AB geometry, and $E(B + b.s.(A)$ is the energy of the isolated fragment B with the basis set of A in the AB geometry.

The difference between $E_{int.} - E_{int.}(BSSE)$ amounts in the systems studied in this work to around 0.1-0.2 eV, about 20% of the binding energy.

2.5 Modeling a crystalline solid

A widely quoted estimate for the number of atoms needed to pass from a microscopic, atomic, scale, to a macroscopic one is the Avogadro number, $\sim 10^{23}$ atoms. This number gives an idea of the large number of atoms that form a real crystal. Calculations of so many particles regardless of the computational technique are not feasible, but, at the same time, at least for atomic processes, are not needed.

A perfect crystalline solid can be represented as an infinite replication of a parallelepiped unit cell containing a relatively small number of atoms. This is the most simple representation of real crystals as obtained from X-ray or neutron diffraction experiments, and actually represents a spatial and time average of the parts of the crystal probed by the experiment.

Although, regardless of the temperature, there cannot be static crystals, i.e. crystals where the constituent atoms are completely at rest[2], generally, as a question of feasibility, most Quantum Mechanical, QM, calculations[3] and many Molecular Mechanical, MM, calculations are completely static, in the so-called 0 K approximation. Although the dynamic information that this approximation may yield is certainly limited, it has been shown to work extremely well in many cases.

In order to make any calculation on a crystalline solid, some kind of strategy may have to be adopted in order to introduce the long range ordering with the minimum use of computational resources. Two diverse approaches are available:

- Periodic approach.
- Cluster approach.

---

[2] There is always an intrinsic ground vibrational state, as a consequence or evidence of the uncertainty principle.

[3] At present any QM dynamic study on any interesting system needs powerful parallel computers.

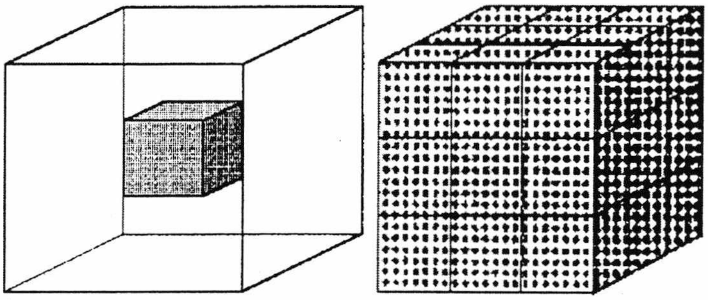

Figure 2.3: Cluster and periodic approaches

2.5.1 Periodic calculations

In a periodic calculation 3/2/1D periodicity can be specified so that the system, mathematically *sees and interacts with itself* in order to reproduce the long range ordering and consequently the Madelung potential created by the rest of the crystal.

For bulk crystal calculations the unit cell, or its representation in the model, is mathematically replicated to infinity. This is possible since due to the size of the real systems termination or superficial effects on bulk properties are virtually negligible. In other words, infinite (ideal) and extremely large (real) can be considered equivalent.

This is ideal for bulk perfect crystal calculations. However, in the presence of localized perturbations, for instance crystal point defects, also the perturbation will be replicated periodically creating an unusually high defect concentration. This is problematic since charged defects interact strongly and give, if not compensated, convergence problems.

The volume surrounding each perturbation can be increased, as to decrease the interaction between perturbations, using supercells where the unit cell is doubled, tripled, etc [19].

All periodic quantum mechanical calculations reported in this thesis were performed with the CRYSTAL98 package [20].

2.5.2 Cluster calculations

Cluster calculations for crystalline solids are nowadays used only in QM calculations. In these calculations only a cluster of atoms is treated quantum mechanically. This cluster might be in vacuum, with suitable terminations, or embedded in something that tries to mimick the rest of the crystal and the potential that this generates. Using clusters allows us to introduce perturbations in the dilution limit, where the perturbations do not interact. As well, it allows us to calculate[4], for any molecule, vibrational frequencies of *any* adsorbed species. Cluster calculations are molecular orbital calculations, and they speak in the chemically more intuitive orbital language. This makes them a powerful tool for bonding studies.

The embedding is not always needed and it is very dependent on the type of system to be studied. For instance, in covalent solids, like SiO_2, most of the work done to date [21] is done with relatively small clusters terminated with fixed[5] hydrogen atoms. *Ab initio* cluster methods have been crucial on the assignment of experimental features of an electronic origin like EPR and optical spectra to specific defects of SiO_2.

In one of the most simple cases of embedding, a fully ionic solid like MgO, clusters are embedded first, by nearest neighbours of border oxygen anions, with bare nuclei with a electronic core pseudopotentials, ECP, [23], that avoids an unphysical polarization of the anions, and the rest in a bigger cluster of point formal charges. This approach has shown to work extremely well in diverse oxides [24].

All cluster quantum mechanical calculations reported in this study were performed with the HONDO 8.5 [25] (HF calculations and CSOV analysis) and Gaussian98 (HF and DFT calculations) [26] packages.

---

[4] Actually, this also is possible for periodic systems in MD calculations, i.e. Car-Parinello techniques, since there is the evolution of the coordinates with time.

[5] Mechanically constraining the cluster to be embedded in the crystal.

Chapter 3

Defects in Ionic Solids

3.1 Point defects in ionic solids

3.1.1 Introduction

An ideal crystal in thermodynamic equilibrium at any temperature greater than 0 K will show a number of perturbations of its, otherwise perfect, three dimensional array of atoms. These perturbations might be very local or, extended to many atomic positions and are generally called, since they alter the "perfection" of the crystal, defects.

Defects in crystals can be classified according to their spatial extension, from point defects, involving only one atom, to extended defects, where point defects are grouped in specific patterns, for instance, dislocations, where an extra plane of atoms is inserted part-way into the ionic lattice.

The extended defects content in a crystal depends on its thermal history, i.e. it is extrinsic, and it is not accurately measurable, although their concentration affects the atomic diffusion and the mechanical properties of the crystal.

Point defects are rather more simple and have been computationally studied with atomistic, molecular mechanics, techniques for a long time [11]. Three of the results chapters of this thesis are dedicated to the study of the energetics of formation, diffusion and clustering of point defects.

3.1.2 Point defects

Point defects appear intrinsically in all crystals at any finite temperature. The content of point defects in an ideally pure crystal increases exponentially, showing their intrinsic thermodynamic nature.

In the simplest case, a pure monoatomic crystal, there can be only two kinds of point defects; atomic vacancies, formed when one of the atoms is missing from its site, and interstitials, formed when one of the atoms moves to an interstitial position of the lattice, fig. 3.4. When the crystal is not pure, extrinsic defects, i.e. impurities, may sit on two possible positions, on a normal atomic site, substitutionally or on an interstitial position, fig. 3.5.

Figure 3.4: A vacancy and an interstitial in a 2D monoatomic solid

Figure 3.5: A substitutional and an interstitial impurity in a 2D monoatomic solid

Although the configurational energies[1] of formation of isolated defects are always endothermic with respect to the perfect crystal, the free energies are negative and therefore they occur spontaneously. The formation of defects is an entropy driven thermodynamic process. Basically, the higher number of defects the higher is the number of possible different ways of arranging them, this configurational

---

[1] Enthalpies without the PV value.

entropy, increases strongly the free energy. In fact, at any give temperature the number of defects will be such as to to maximize the free energy in a balance between the increasingly endothermic enthalpy and the increasing of configurational entropy.

From all these considerations, it can be shown that the free energy for a single electronic state, pure monoatomic solid with non-interacting defects at a specific NPT conditions will show a maximum with respect to the concentration of defects corresponding to the following equations:

$$c_v = \frac{n_v}{N + n_v} = exp\left(\frac{-g_v}{kT}\right) \tag{3.35}$$

$$c_i = \frac{n_i}{\beta N + n_i} = exp\left(\frac{-g_i}{kT}\right) \tag{3.36}$$

Here the subscripts v and i represent vacancies and interstitials respectively, c is the fraction site, or molar fraction of defects, n is the number of defects, N is the number of atoms, g the free energy of formation of a defect, k is the Boltzmann's constant, T is the temperature and β, is the number of interstitial sites associated with a specific atomic site.

3.1.3 Point defects in ionic solids

The formation of point defects in ionic solids, especially in fully ionic crystals[2], imply that since defects have to maintain the overall charge neutrality of the crystal, they have, statistically, to be formed in multiplets.

For instance in a generic MX solid, three types of defects, are in principle possible:

- Schottky pairs: One cation and one anion move to surface sites creating one cation and one anion vacancy fig. 3.6.

---

[2] In *semi*-ionic crystals, as transition metal oxides, charge compensation may occur by the "creation" of an electron or a hole.

- cation Frenkel pairs: A cation leaves its regular site to go to an interstitial one, fig. 3.7.
- anion Frenkel pairs: An anion leaves its regular site to go to an interstitial one, fig. 3.7.

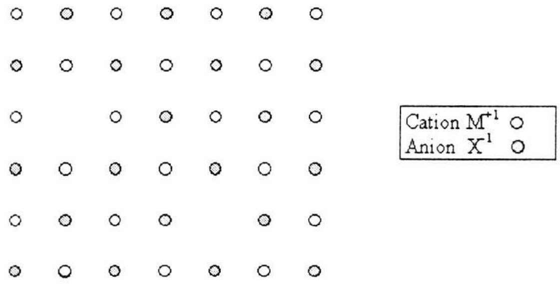

Figure 3.6: Schottky defect in a 2D ionic diatomic solid

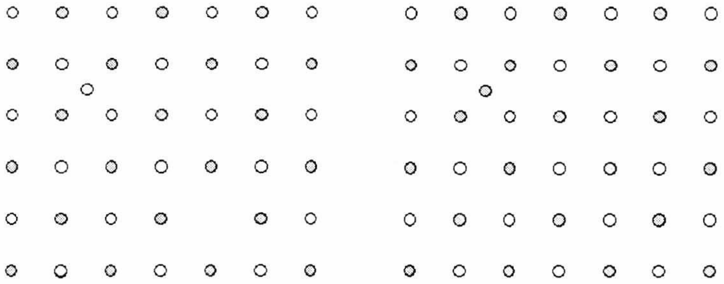

Figure 3.7: Frenkel defects in a 2D ionic diatomic solid

Although, theoretically, the charge could be compensated by creating one cation and one anion interstitials, the so-called anti-Schottky defect, this defect has not yet been found in real systems.

It can be mathematically shown, that the relationship of site fractions for a perfect pure crystal, for non interacting defects in thermodynamic equilibrium is related with temperature, the concentration of pair defects is constant and its equilibrium constant for a Schottky and cation Frenkel pair can be described by the equations:

$$c_{cv} \cdot c_{av} = K_S = exp\left(\frac{-g_{vs}}{kT}\right) \tag{3.37}$$

$$c_{cv} \cdot c_{ci} = K_{cF} = exp\left(\frac{-g_{cf}}{kT}\right) \tag{3.38}$$

Here c_{cv}, is the site fraction of cation vacancies, c_{av}, site fraction of anion vacancies, K_S, equilibrium constant for the formation of Schottky defects, g_S, free energy of the formation of isolated point defect of the corresponding Schottky, c_{ci}, site fraction of cation interstitials, K_{cF}, equilibrium constant for the formation of cation Frenkel, and g_{cF}, the free energy of formation of an isolated cation vacancy and an isolated cation interstitial. Two good reviews of point ionic defects in ionic solids can be found in [27, 28].

3.1.3.1 Extrinsic and intrinsic regions: conductivity studies

Basically, the conductivity of a material is the quantitative capacity of the material of transporting an electric current when under an electric field.

In ionic compounds the conductivity is due to the motion, i.e. diffusion, of point defects within the bulk of the solid. This is due to the fact that each isolated defect has an effective charge. From measurement of conductivity information about the mobility and the concentration of defects can be obtained.

The temperature dependence of ionic conductivity is usually given by the Arrhenius equation:

$$\sigma = A \cdot exp\left(\frac{-E}{kT}\right) \tag{3.39}$$

Where A is the pre-exponential factor that, among other things, involves the frequency of vibration of the atoms over the lattice positions and σ is the conductivity. Formally, this equation describes the dependence of kinetic processes with temperature. This emphasizes the fundamental microscopic thermally[3] activated phenomena, atomic diffusion, underlying macroscopic conductivity. According

---

[3] The exponential factor comes naturally from the Boltzmann statistical distribution.

with equation 3.39 if we plot the logarithm of the specific conductivity against the temperature we should obtain a straight line. Actually this would be the case for ideal crystals with non-interacting defects and only one charged species diffusing and reality is slightly more complex. From a complete range of temperatures, from close to zero Kelvin to temperatures near the melting point, for a crystal of a strongly ionic diatomic ionic solid, NaCl (Schottky defective) four zones are observed (fig.3.8):

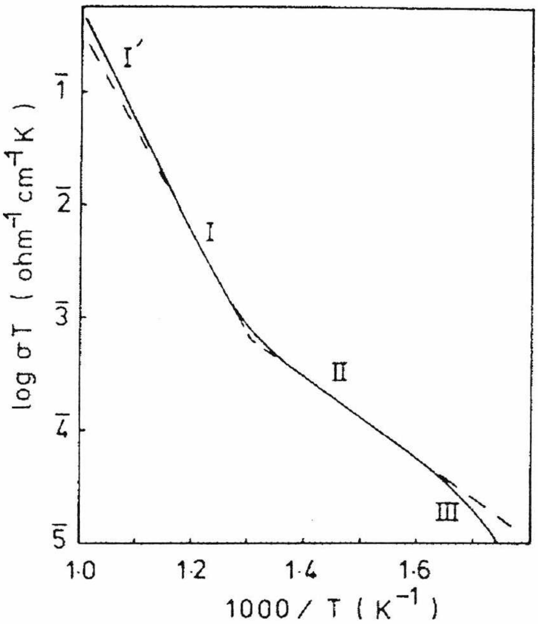

Figure 3.8: Ionic conductivity of nominally pure NaCl versus temperature [29]

- Zone III, the conductivity trend observed in this zone is due to clustering of defects. The defects of opposed charges are grouping, so the number of free charge carriers is reduced, reducing drastically the conductivity with decreasing temperature.

- Zone II, the extrinsic zone, this is defined as the zone where the content of aliovalent impurities is much larger than the thermodynamic correspondent defects content of a pure crystal. The increase of temperature increases negligibly the content of defects and the conductivity increases due to an increase in the number of mobile defects, or atoms jumping on defects, that can overcome the activation barrier of the diffusion path. The slope in this region yields the activation energy for defect migration.

- Zone I, the intrinsic zone, in this case the increase of temperature increases the number of defects and the number of diffusing atoms. The slope in this region yields the sum of the activation energy for defect migration and half the energy for defect formation.

- Zone I', the other species, with a higher activation barrier, begins to diffuse quantitatively.

The relative position of the intrinsic and extrinsic zone depends on the level of present impurities of the materials, although the slopes should be, ideally independent of this. Experimentally the results in the intrinsic region are quite reproducible, i.e. intrinsic, while in the extrinsic zone this depends on the degree of purity of the particular specimen employed and to some extent on its thermal and mechanical history.

A more detailed description of the conductivity regions and the Arrhenius equation for ionic conductivity can be found in [27, 29].

3.2 Defects energies: the Mott-Littleton method

Single point defects in ionic solids are in most cases charged. The Coulomb potential implies that there is a $1/r$ long range interaction arising from the charge of the defect that might be difficult to converge with a computationally feasible number of atoms.

The problem can be simplified by assuming some approximations according to the method due to Mott and Littleton [5] in which a spherical region surrounding the defect is divided into three concentric spherical regions, I and IIa, of a discrete size, and IIb that comprises the rest of the crystal to infinity, fig.3.9.

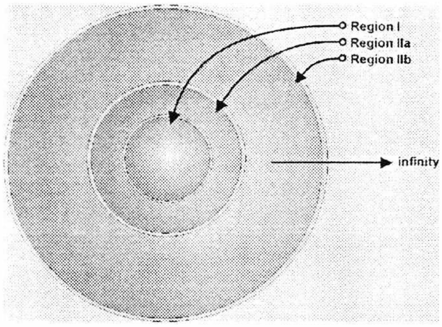

Figure 3.9: Mott-Littleton regions

Region I atoms surround directly the defect and interact strongly with it. In this region the atoms are relaxed to minimum strain (not minimum energy) at the very same level of approximation a bulk crystal relaxation is calculated [10].

Region II is divided in two zones, regions IIa and IIb, in both the atoms interaction with region I as a whole and with the defect, if charged, are treated in a approximate way.

In Region IIa, the ions are assumed to be situated in a harmonic well and they relax responding to the force due to the perturbation accordingly. It is important to emphasize that the ions have to be in the bulk equilibrium position set by the potentials so that the harmonic approximation holds (the smaller the displacement the better the approximation, all equilibrium potential wells are quadratic very near the minimum). Only long-range interactions are considered, and in the less approximate way implemented in GULP [9], the forces come from electrostatic forces of region I screened by the dielectric constant of the model.

In Region IIb, the ions are not allowed to relax, and only polarization of the sublattices is allowed. Polarization arising from the defect charge screened by the dielectric constant. More specific details of the calculations and approximations can be found in [10].

It is important to note that this method yields configurational defect energies, and no direct evaluation of defect entropies[4] is included. This should be considered when comparing the calculated energies with experiment.

3.2.1 Regions radii versus defect energy convergence

In defect calculations the Mott-Littleton regions radii are increased until a certain relative convergence in energy is achieved. Absolute convergence is not computationally achievable.

We have performed some test calculations with GULP that yield very interesting results. For instance, calculations on MgO with a shell model for a Mg vacancy converge to differences <0.01 eV, mostly at region I radius of 8 Å and region IIa radius of 16 Å (actually the convergence is mostly due to region I, the region IIa could be much smaller). With these radii region I contains 250 ions and region IIa 1558 ions[5]. In the optimization, the number of parameters can be constrained with symmetry and with an appropriate centring of the regions substantially reduced. Convergence depends strongly on the parameter set and model. For instance the explicit presence of polarization, embodied in a shell model allows a much faster convergence than a similar calculation with a rigid ion model on CdF_2.

---

[4] The presence of an interstitial or vacancy will change the vibrational frequencies of the closer atoms hence altering the entropy.

[5] The number of particles in the calculations is doubled when using a shell model.

However, this convergence might be apparent: we have performed computations on both systems, shell model MgO, and rigid ion CdF_2, with different radii for region I up to 16 A and 22 Å, respectively. In these calculations, the energy convergence between different sizes was not found to continuously decrease with increasing sizes showing large oscillations after a certain, relatively large region I radius[6]. This has been never been observed before, however until quite recently these calculations were rather too expensive for the current hardware.

Although, more work is still needed to be able to clarify the source of these findings, it seems that relative convergence is not achievable in these type of computations and the widely cited in literature "convergence with radius size" might be just an artifact.

---

[6] Different for both systems.

Part II

Molecular Mechanics Simulations

Chapter 4

Alkali and Alkaline Earth Hydrides

4.1 Introduction

Metal hydrides have been object of a high research activity due to various technological applications as well as an intrinsic scientific interest. Most of the research has been focussed on CaH_2, LiH and MgH_2 (mainly due to their relative chemical stability [31]). Hydrogen has shown a very interesting prospect for fuel cells, and the metal hydrides are the most convenient carriers of hydrogen, among which the light-metal hydrides are considered to be the best candidates because of their high weight percentage of hydrogen.

4.1.1 Objectives

CaH_2 when heated suffers a phase transformation at 1053±10 K [32] from the more dense $PbCl_2$ contunite structure to the fluorite structure, and melts at 1089 K (H_2 atmosphere). With the change of structure a dramatic increase in electrical conductivity [33] is observed. Fluorite structured solids have been known from Faraday's time for their high liquid-like conductivity at temperatures near the melting point [34] and are classed as fast-ion conductors; materials with unusually high ionic conductivities. Fast ion conductors are technologically interesting for applications as solid electrolytes in batteries and fuel cells.

Fast ion conduction in fluorites has been extensively studied with Molecular Dynamics, MD, techniques with remarkable success with quite simple models; for instance in CaF_2, Gillan et al. [35] with a rigid ion model obtained basically the same results that Madden et al. with a high quality *ab initio* derived compressible ion model [36].

In comparison to CaF_2, CaH_2 is a very interesting system, since due to the lightness of the H atom, diffusion should be much faster and, at the same time, strongly dependent of isotopic content (a brief section of why this cannot be studied with static methods can be found in appendix C).

The main objective of this study is to develop an empirical potential to model the CaH_2 diffusion and defect stability on both phases statically and dynamically. The two phases, by analogy with PbF_2, will be called α (lower temperature orthorhombic) and β (high temperature cubic).

4.1.2 Bonding in hydrides

The H atom when combined with other atoms may form compounds with three qualitatively different ways of bonding; protonic, anionic or covalent bonding.

- Protonic bonding, where the H atom has lost his only electron, with electronegative atoms like Cl or F, or molecules (acids).
- Covalent bonding, where it shares its electron with a neighbouring atom to form a covalent bond, like in water, methane, etc.
- Ionic bonding, where the H atom gets one electron from electropositive atoms, like Li or Na.

All these different bonding models have been used to explain materials properties as function of bonding nature in, metal hydride (MH) crystals. The purely anionic model is found to work well for the typically ionic alkali-metal hydrides.

For alkaline earth-metal hydrides, BeH_2 has been shown to be completely covalent, while CaH_2 and MgH_2 are known to be largely anionic with little covalency [37, 38]. For some transition-metal hydrides such as TiH_x [39] the protonic model was found to be fairly successful. For some other systems such as NbH_x [40] different properties of the system cannot fit with a single model.

The chosen method of calculation for this study, molecular mechanics, does not include specifically the calculation of electronic charge distributions and the oxidation state of the atoms is fixed through all the calculations. Although, different formal charge of the ions could be used. From a fundamental point of view the H^+ and a H^- are very different ions and so will be the interaction with other atoms. Our calculations, consequently, will be restricted to materials whose H anionic character is known or can be assumed.

4.1.3 Alkali and alkaline earth metal hydrides structures

For this study, the CaH_2, NaH and LiH structures were taken from neutron diffraction experiments [41, 42, 43], while the MgH_2 and BaH_2 were taken from X-ray diffraction experiments [44, 45] (the criteria used for selection of structures can be found in appendix B).

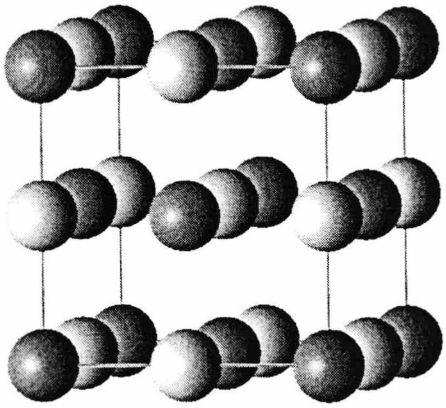

Figure 4.10: LiH and NaH structure

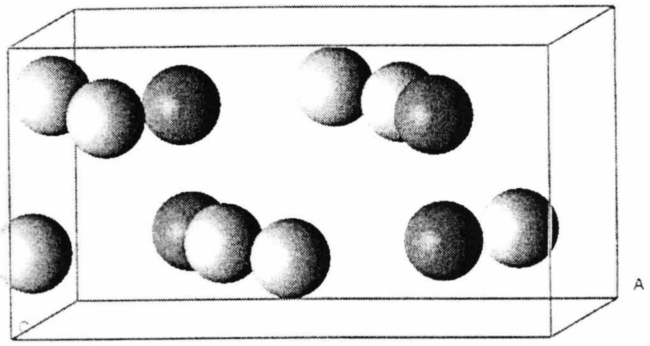

Figure 4.11: α-CaH_2 structure, Ca atoms darker spheres, H atoms: lighter spheres

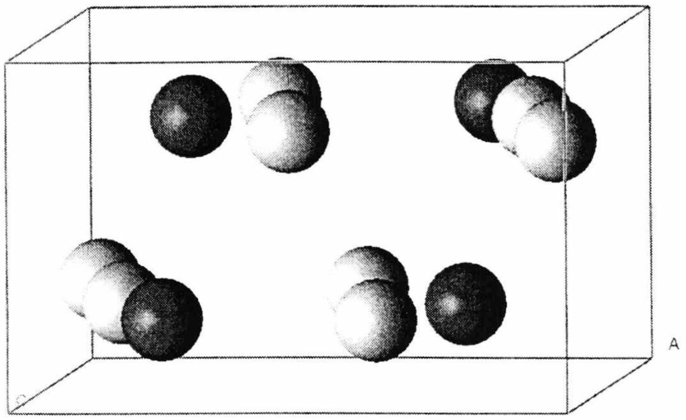

Figure 4.12: BaH_2 structure, Ba atoms: darker spheres, H atoms: lighter spheres

At room temperature, NaH and LiH are both cubic with the rock-salt structure, fig. 4.10. CaH_2 and BaH_2 are orthorhombic with the layered $PbCl_2$-contunite structure, figs. 4.11 and 4.12 respectively, while MgH_2 is tetragonal, fig. 4.13.

A qualitative comparison of the presented structures can be obtained from the number of nearest neighbours, nn, atoms and the distances to the metal cation. From table 4.1, it is clear that symmetry, and coordination decreases in the alkaline earths with increasing atomic number, suggesting an increase in the degree of covalency in the M–H bonding.

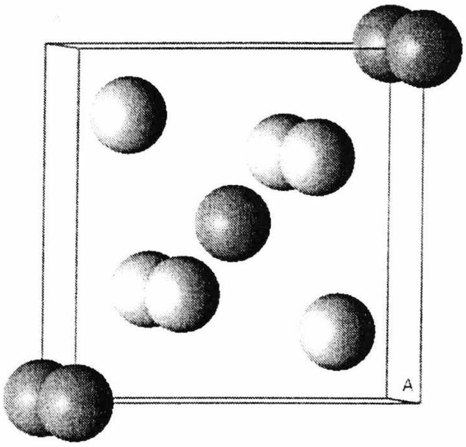

Figure 4.13: MgH_2 structure, Mg atoms: darker spheres, H atoms: lighter spheres

Metal Atom	Z	$r_{MH}/\text{Å}$
Li	6	2.04
Na	6	2.44
Mg	4	1.95
Ca	3	2.31
Ba	1	2.50

Table 4.1: Nearest neighbour MH distances and coordinations numbers, Z

4.2 Developing of H-H interatomic potentials

4.2.1 Introduction

In the initial step, a fitting of CaH_2 with the H-H potentials of A.K.M.A. Islam et al. [46] was tried, however a reasonable reproduction of the structure with the H-H potential fixed was not achievable. Furthermore, these potentials in fitting in LiH (the system they were developed for) were not stable and the parameters diverged to unphysical values, which might be interpreted by an intrinsic instability of the potential set.

Previous work on $PbCl_2$ structures potential developing has been proven relatively difficult [47]. At the same time, there is no experimental data available, besides the structure, for the fitting. For simplicity and speed of calculations in our initial model all ions will be unpolarizable (i.e. rigid) and only short range interactions between M–H ions and H–H ions[1] will be considered.

All the fitting of potentials and subsequent calculations have been performed with the program GULP [9], sect. 1.4.1.

4.2.2 Rigid ion H-H potential

Traditional methods of potential development, for instance starting from similar systems potentials, i.e. CaF_2, or genetic algorithm sampling, failed. Therefore a new approach had to be adopted. We opted for what we consider an extension, at least of methodology, of the work of Bush et al. [30] in metal oxides. In that work, a relatively high number of oxides was *simultaneously*[2] fitted with a common O-O potential. Further work with that parameter set predicted the previously unknown structure of Li_3RuO_4 [48] and in a very interesting work by Woodley et al [49] the mechanical[3] phases predicted by interatomic potentials in oxides achieved a

---

[1] The M–M distances for any of the compounds used in the fitting is rather too large to be fittable empirically, i.e. the value of the SR potential at those distances is too small.

[2] The potential fitting is performed with respect to all structures contemporaneously.

[3] Mechanical, since they are calculated statically, for more information see [50].

notable success.

A multifit, sect 1.4.4, exploration of interatomic potentials for CaH_2 was performed. In order to reduce to a minimum the number of starting parameters without restricting the dimensionality of the exploration, we have undertaken two different sampling strategies. In the first one, the A and ρ starting parameters are systematically changed while C values are fixed and equal to zero. In the second one, the ρ and C initial parameters were sampled, although the C was fixed in the fitting[4]. The total number of fittings-optimizations was around 12000, and all fittings were gradient based. The selection criteria for further refining of potentials was based upon structural convergence and not on structural gradients. This choice was reinforced by the fact that the optimized structures that better resembled the experimental structures obtained from gradients least square fitting were not the ones that showed a better convergence[5]. This emphasizes the need of a multifit approach for a full development of potential sets for/with asymmetric structures, since relaxed fitting cannot converge from starting points far from the minimum and genetic algorithms are gradients based. The most promising potentials sets from the multifit were further refined with a relaxed fitting in order to obtain the final potentials.

A similar procedure was undertaken with the isomorph BaH_2, the grid used was more coarse in the A value (resulting in only 1200 simulations) and only variations on A and ρ were tried. Although there was not any bias (apart from the range and constraints of the sampling) the final H–H potential was extremely similar to the one obtained from CaH_2. This strongly suggests the reliability of a common H–H potential for both systems.

In order to further explore the transferability of the H-H potential, a multifit exploration on other systems was undertaken in which a *simultaneously* refined,

---

[4] C parameters are very unstable in fitting and tend to go either to 0 or to unphysical values, [10].

[5] This comes from the harmonic approximation in the fitting [10].

CaH_2, BaH_2, H–H potential was fixed in the fitting and the grid of starting parameters was only applied to the metal–H interaction. Three non-highly symmetric di-hydride ion systems were tried: ZrH_2, SrH_2, MgH_2. MgH_2 was the only one for which potentials reasonably reproduced the experimental structure. Further multifit calculations with a finer gridding interval, less constraints and relaxed fitting for both other systems were tried without success.

In the ZrH_2 case this can be rationalized by the bonding being not very ionic. However, in the SrH_2 case, the reasons are not clear, since the BaH_2 and CaH_2 systems, comprising the next and previous alkaline earth cations, have been readily fitted (although the quality of the structural determination analysis may be the cause[6]).

The number of structures with a common H-H potential was increased to include NaH and LiH. Both structures are highly symmetric and there was no need of a multifit. In the final step, a simultaneous relaxed fitting with respect to all the crystals where all the potential variables, A, ρ and C_{H-H}, were optimized was performed to obtain the definitive potential set.

The optimized structures with the final potential set resembled quite closely the experimental ones. However the static dielectric constant for LiH in our model presented a unphysically high value, 10 times larger than the reported value from experiment, 12.9±5 [51].

It has been pointed out by Gillan[7] et al. [35] that a reasonable reproduction of the experimental dielectric constant of the material can be a crucial point for a reliable simulation of defects. At the same time the defects obtained with a very high dielectric constant model should be much more stable due to a more extensive screening of the charge.

The definitive potential refinement was performed also with respect to the

---

[6] The structure was determined in 1935 and needs to be re-studied.

[7] Arising from an empirical rule in fluorite structures fast ion conductors that correlates the fast ion conduction transition temperature and dielectric constants of different compounds.

dielectric constant of LiH. Although this, in comparison, resulted in worse structural values for CaH_2 and BaH_2, the values for the LiH dielectric constant were much more similar to experiment. The results obtained with this potential set, are summarized in table 4.2, the difference in LiH and NaH structures with optimization were negligible, the angles of all structures were not distorted (even when the symmetry constraint were, as a test, removed). All the translational phonon frequencies show very good values (between -0.1 and 0.1).

It is worth noting, from table 4.2, that, qualitatively, the goodness of the fit decreases with increasing covalency (which cannot be subsumed by a rigid ion model).

MgH_2	exp.	calc.	diff.	diff. %
Volume/Å^3	61.623	61.752	0.130	0.2
a/ Å	4.517	4.506	-0.011	-0.2
b/ Å	4.517	4.506	-0.011	-0.2
c/ Å	3.021	3.041	0.021	0.7
CaH_2	exp.	calc.	diff.	diff. %
Volume/Å^3	146.125	143.735	-2.390	-1.6
a/ Å	5.936	5.890	-0.046	-0.8
b/ Å	3.600	3.548	-0.052	-1.4
c/ Å	6.838	6.878	0.040	0.6
BaH_2	exp.	calc.	diff.	diff. %
Volume/Å^3	222.453	219.974	-2.478	-1.1
a/ Å	6.792	6.803	0.011	0.2
b/ Å	4.168	4.098	-0.070	-1.7
c/ Å	7.858	7.891	0.033	0.4
LiH	exp.	calc.	diff.	diff. %
ε_0	12.9±0.5	11.1	1.8	13.7

Table 4.2: Comparison of experimental and calculated properties on MgH_2, CaH_2, BaH_2 and LiH

Ions		A/eV	ρ /Å	C/eV · $Å^6$	Cutoff/Å
H	H	46942.02	0.2115	67.496	12.000
H	Li	215.78	0.3137	0.000	10.000
H	Na	199.30	0.3743	0.000	10.000
H	Mg	777.63	0.2837	0.000	12.000
H	Ca	5875.79	0.2424	0.000	12.000
H	Ba	754.67	0.3666	0.000	12.000

Table 4.3: Short range rigid ion model MH and HH potentials

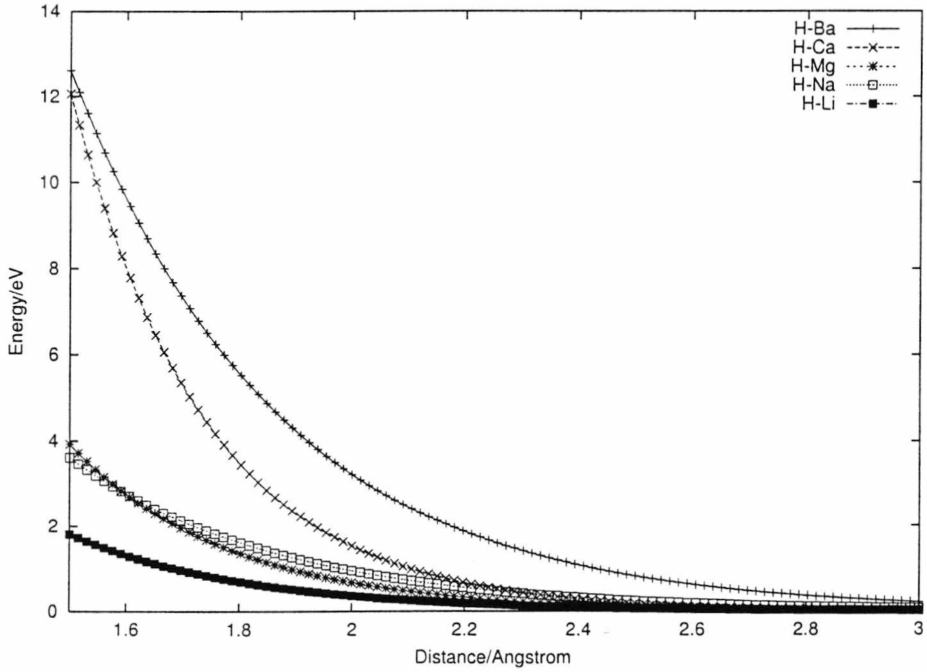

Figure 4.14: Short range rigid ion model MH potentials

4.2.2.1 Trends on rigid ion MH potentials

In table 4.3 we present the values for the rigid ion potentials set and cutoffs used[8]. The error in energy due to the H-H SR cutoff was $< 3 \cdot 10^{-5}$ eV.

The plot of the M-H SR potentials in a meaningful range[9] against distance shows a clear trend in repulsive energy, fig. 4.14; $BaH_2 > CaH_2 > MgH_2 \simeq NaH > LiH$. This is associated with the Pauli repulsion and can be interpreted as coming from an increase of the effective ionic radius[10]. Mg and Na, isoelectronic in a fully ionic hydride, show very similar potentials, with, as expected, Na being slightly more repulsive due to the lower ionic charge[11].

The observed trend may apparently be *a priori* expectable, since, the fit of potentials is mainly performed for structures that show the same trend in distances, table 4.1. However, the structures fitted are quite heterogeneous and, although the distance trend exists, distances for MgH_2 and NaH are quite different[12]. The presence of this trend reinforces the good quality of the potentials, and the method to derive them.

4.2.3 Shell model H-H potential

Rigid ion models have been very succesfully used in MD simulations applied to similar problems [35]. However, an explicitly polarizable ion model is important for the energetics of defects and will allow the partial introduction of covalency in the model, sect 1.3.3.

The very low percentage of succesful reproduction of the structures in the multifit in asymmetric structures, $< 10\%$ of all the different starting points, shows

---

[8] These are the cutoffs used in the development of potentials, note that since C_{MH} is zero they could be further reduced in the M–H potentials.

[9] The range containing distances of the first shell of coordination of the metal ions around the H.

[10] The ionic electronic distributions radially expands going down in the Periodic Table.

[11] The electronic distribution of a closed shell atom radially contracts the higher the nuclear charge.

[12] Not surprisingly since Mg ion has a formal charge twice of Na one.

that even with rigid ion interactions, the fitting space for the asymmetric structures is very complex and depends strongly on starting points.

In shell models, for non-cubic structures, the shells are displaced from the cores resulting in further difficulties in the fitting due to the increase in complexity. We have consequently used the rigid ion potential set as the starting point for the shell model potentials fitting. This is justified from the fact that in the cubic structures, namely NaH and LiH, the interatomic potentials for the rigid ion model and the shell model are fully equivalent. The shell parameters, since they account for polarization, are mainly fitted to the high frequency dielectric constant[13]. Since data of this kind is only available for LiH, we have tried the fitting with different, pre-derived, shell-core split charges and its correspondent springs, from similar metal fluorides and oxides.

- Li: from LiF [52].
- Na: from NaF [52].
- H: from LiH [46] and [51].
- Mg: from MgO [30]
- Ca: from CaF_2 [53] and CaO [30].
- Ba: from BaF_2 [53] and BaO [30]

All the potentials were simultaneously re-fitted after any change on shell parameters. Due to the lack of experimental properties for CaH_2, we have developed two potentials sets differing only in the Ca shell parameters, they will be referred to as set I, from CaF_2, and set II, from CaO. In the Ba case only the fit with the shell parameters from BaO reasonably reproduced the structures.

The presence of the LiH high-frequency dielectric constant and the LiH elastic constants destabilized the potential fit and the only non-structural parameter included was the LiH static dielectric constant.

---

[13] Which is, ideally, related only to the electronic polarization.

The spring constants and shell charges used are shown in table 4.4. Set I and II shell–shell potentials are shown in tables 4.5 and 4.6,

Ion	k / eV · Å^{-2}	$Y\|e\|$
H	3.23	-0.999
Na	∞	1.000
Li	250.00	0.705
Mg	349.95	0.420
Ca (set I)	34.05	1.281
Ca (set II)	390.90	5.240
Ba	34.05	1.831

Table 4.4: Spring constants, k, and shell charges, $Y|e|$, for MH potentials

Ions		A/eV	ρ /Å	C/eV · Å^6	Cutoff/Å
H	H	48784.64	0.2102	63.094	12.000
H	Li	188.33	0.3218	0.000	10.000
H	Na	187.25	0.3704	0.000	10.000
H	Mg	947.81	0.2744	0.000	12.000
H	Ca	4681.08	0.2486	0.000	12.000
H	Ba	432.92	0.4013	0.000	12.000

Table 4.5: Set I short range shell model pairwise MH and HH potentials

The resulting potentials are, as expected, similar. In spite of this, it is important to notice how sensitive the potential fit is to the change of the shell parameters, emphasizing the need of simultaneous fitting of all the potentials with all structures.

The resulting LiH structure and LiH properties are in worse agreement than the ones obtained with the Islam potential, table 4.7. In contrast, the fitting with the H-H Islam potential as a starting point was not achievable with a shell model for any of the asymmetric structures, as also observed with the rigid ion model. This may arise from a general lack of flexibility of the Buckingham potential; the function is rather too simple to simultaneously fit the curvature (properties) and the nn distance (structures).

Ions		A/eV	ρ /Å	C/eV · Å^6	Cutoff/Å
H	H	52596.22	0.2133	53.093	12.000
H	Li	194.579	0.3732	0.000	10.000
H	Na	322.64	0.2851	0.000	10.000
H	Mg	711.36	0.2778	0.000	12.000
H	Ca	6731.17	0.2343	0.000	12.000
H	Ba	582.13	0.3790	0.000	12.000

Table 4.6: Set II short range shell model pairwise MH and HH potentials

	exp.	Islam[46]	Set I	Set II
C_{11}/10 GPa	7.41±0.2	7.89	12.20	13.84
C_{12}/10 GPa	1.42±0.03	4.41	7.16	8.67
C_{44}/10 GPa	4.84±0.18	4.41	7.16	8.67
ε_0	12.9±0.5	16.65	12.94	13.07
ε_∞	3.61±0.5	3.61	3.56	3.56
a/Å	4.083	4.083	4.087	4.095

Table 4.7: LiH properties with different shell–potential sets

Set I gives closer agreement to the properties of LiH than set II. In contrast, tables 4.8 and 4.9, the structures for CaH_2 and MgH_2 are better described by Set II (BaH_2 structures are fairly similar with both sets).

MgH_2	exp.	calc.	diff.	diff. %
Volume/Å^3	61.623	61.587	-0.035	-0.06
a/ Å	4.517	4.506	-0.011	-0.25
b/ Å	4.517	4.506	-0.011	-0.25
c/ Å	3.021	3.034	0.013	0.44
CaH_2	exp.	calc.	diff.	diff. %
Volume/Å^3	146.125	143.884	-2.242	-1.53
a/ Å	5.936	5.894	-0.042	-0.72
b/ Å	3.600	3.550	-0.050	-1.38
c/ Å	6.838	6.877	0.039	0.56
BaH_2	exp.	calc.	diff.	diff. %
Volume/Å^3	222.453	221.186	-1.267	-0.57
a/ Å	6.792	6.825	0.033	0.49
b/ Å	4.168	4.128	-0.040	-0.95
c/ Å	7.858	7.850	-0.008	-0.10

Table 4.8: Comparison of experimental and calculated properties for MgH_2, CaH_2, BaH_2 optimized with parameters set I

MgH_2	exp.	calc.	diff.	diff. %
Volume/Å^3	61.623	61.548	0.130	0.130
a/ Å	4.517	4.519	-0.011	-0.011
b/ Å	4.517	4.519	-0.011	-0.011
c/ Å	3.021	3.014	0.021	0.021
CaH_2	exp.	calc.	diff.	diff. %
Volume/Å^3	146.125	145.260	-0.866	-0.59
a/ Å	5.936	5.914	-0.022	-0.36
b/ Å	3.600	3.583	-0.017	-0.47
c/ Å	6.838	6.854	0.016	0.24
BaH_2	exp.	calc.	diff.	diff. %
Volume/Å^3	222.453	220.994	-1.459	-0.66
a/ Å	6.792	6.818	0.026	0.39
b/ Å	4.168	4.124	-0.044	-1.04
c/ Å	7.858	7.858	0.000	0.00

Table 4.9: Comparison of experimental and calculated properties for MgH_2, CaH_2, BaH_2 optimized with parameters set II

4.2.3.1 Trends on Shell model MH potentials

The trend in repulsive energies observed for our rigid ion potential still applies for the shell model, figs. 4.15 and 4.16, appearing more clearly in set II. Although this is not surprising due to the similarity of H–H potentials in all sets, fig. 4.17.

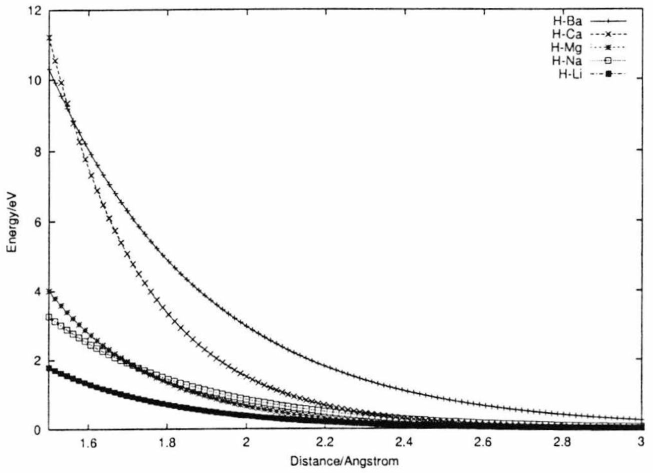

Figure 4.15: Set I short range shell model pairwise MH potential

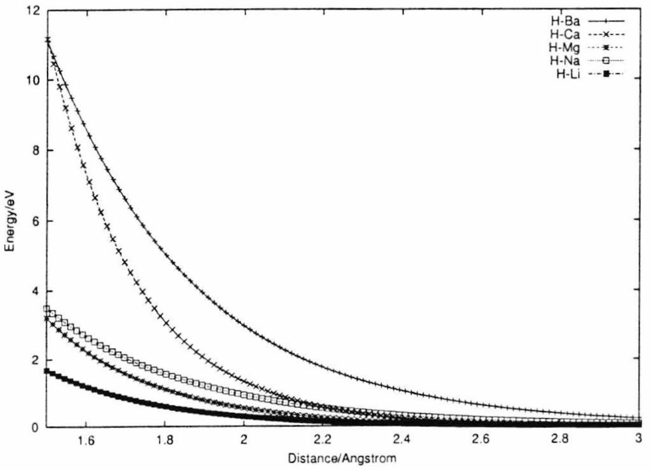

Figure 4.16: Set II short range shell model pairwise MH potential

4.2.4 Comparison of different H–H potentials

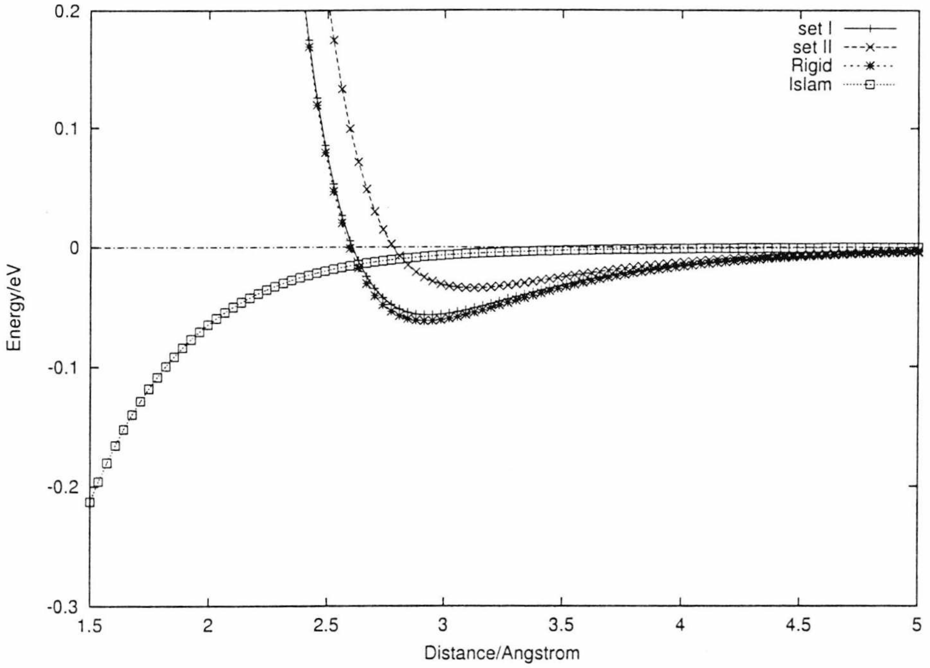

Figure 4.17: Set I, set II, rigid and Islam H–H potentials

Islam potentials [46] were fitted to the properties and structure of LiH and NaH. With symmetry constraints this translates to the sampling of just two H–H distances, 2.9 Å and 3.5 Å, respectively. At those distances the contribution to the total lattice energy by this SR potential is very small, <0.01 eV per H-H pair (less than 0.5% of the cohesive energy of the model) and consequently any variation in the potential parameters must contribute mostly to the right curvature of the structural minimum. A plot versus distance of the Islam potential, fig. 4.17, shows it to be virtually flat at long–medium distances to become more and more attractive at decreasing distances (which is completely unphysical). Furthermore, an optimization of the LiH structure without the H-H potential did not yield very different results, showing explicitly that this potential has a relatively small contribution to the properties of the model. In view of all this, we can conclude that the use of the Islam potential is very limited for any non-perfect crystal calculation. The comparison of calculations of LiH point defects, sect. 4.3, with experiment will further confirm this.

In our fitting, on the contrary, 11 H–H distances from 2.5 to 2.9 Å are sampled resulting in a repulsive, *physical*, potential at short distances, fig. 4.17. In the developed potential sets, the H–H potentials for the rigid ion and the best, reproduction of structures, shell model, set II, are very similar, while set I is slightly different but not significantly.

To conclude this section, we would like to point out that LiH, as a test, has been fitted starting from our set II potential to a similar reproducibility of properties and structure as obtained with the Islam potential. However, the same problem was encountered; the fitting the potential tends intrinsically to minimize the H-H repulsion, yielding a very similar potential to the Islam potential. This confirms that the problem is due to lack of flexibility of the Buckingham potential function, and not due to a *wrong* derivation of potentials.

4.3 Testing the potentials; defect calculations on LiH

All previous MM theoretical works in LiH [51, 54, 55] have obtained a similar value for the activation energies for diffusion of both atoms, Li^+ and H^-.

This does not agree with all the experimental results which have been specifically discussed, doubted and, somehow, misquoted by some authors [54, 55], and will be reviewed in the following section.

4.3.1 Experimental studies

Single crystal conductivity studies by Ikeya [56] show that the doping with Mg^{2+} ion increases the extrinsic electrical conductivity of LiH without affecting the slope (i.e. the activation energy) of this region. Assuming Schottky defects[14], the aliovalent doping would form cation, Li^+, vacancies that would increase the

---

[14] The normally found intrinsic defects in rock-salt structures.

conductivity with respect to the pure material. The obtained activation energies for Li^+ diffusion, 0.54 eV, agrees extremely well with the works on nominally pure polycrystalline LiH samples [57] and LiH and LiD single crystals [58].

The hydrogen diffusion at high temperature studied by NMR gives an Arrhenius energy of 1.1 eV [59]. Assuming the crystal is pure and the behaviour intrinsic, this value is the sum of two contributions: the energy for anion vacancy creation and the activation energy for vacancy migration, the values for H^- self-diffusion are estimated to be around 1 eV or less. Since, hydrogen tunneling[15] is discarded at any of the temperatures we are considering, the anionic diffusion will be due to ions hoping into vacancies. So at least at high temperatures the anions are mobile, as well as the cations. However, in the extrinsic region there is no doubt that the conductivity comes from cations, since its absolute value depends on concentration of the dopant, and this consequently should be the activation energy we measure. It is important to emphasize that there is no observable curvature in the conductivity data that could imply two different simultaneous diffusion processes, as suggested by some authors [54, 55], and therefore the activation energy for H^- diffusion must be higher than the activation energy for Li^+ diffusion. This is also expected from the fact that the Li^+ radius is much smaller[16] (0.6 Å) than H^- (2∼1.4 Å.) [56].

4.3.2 Computational simulation of defects

4.3.2.1 Energy of formation of defects

A priori, LiH may show three kinds of intrinsic defects: Li Frenkel, H Frenkel and Schottky pairs, according with the following equations (Kröger-Vink notation [60]):

$$Li_{Li}^{X} + H_{H}^{X} \rightleftharpoons V_{Li}^{'} + V_{H}^{\cdot} + LiH \tag{4.40}$$

---

[15] Where there would not be activation energy as such!.

[16] As our potentials show in the previous section.

$$Li_{Li}^{X} + H_{H}^{X} \rightleftharpoons V_{Li}^{'} + Li_{i}^{\cdot} \tag{4.41}$$

$$Li_{Li}^{X} + H_{H}^{X} \rightleftharpoons V_{H}^{\cdot} + H_{i}^{'} \tag{4.42}$$

The energetics for all the defects, have been calculated , table 4.10, with regions I and IIa radii of 7 (~ 200 ions) and 15 Å, respectively. Since the LiH is known to be strongly ionic we have considered calculated cohesive energies (the calculated cohesive energies with our sets differ between themselves by less than 0.2 eV). Interstitials were calculated on the 0.25 0.25 0.25 fractional position (the most stable position). In all cases Schottky pairs are predicted to be the most stable defects. Our results for the Schottky energy are in very good agreement with experiment. Although, in comparison with previous similar MM works [11], this is very likely to be fortuitous.

	Islam	Rigid	Set I	Set II	exp.
Schottky pair/eV	1.58	2.53	2.38	2.40	2.30±0.30 [56, 57]
Frenkel H/eV	2.85	4.13	3.95	3.18	—
Frenkel Li/eV	12.32	14.17	13.93	14.30	—

Table 4.10: LiH calculated and experimental defect formation energies
The Islam potentials results are recalculated with our conditions

4.3.2.2 Activation energy for diffusion

It seems surprising that a method that does not specifically consider any dynamic process, can be used for studying the atomic diffusion, an intrinsically kinetic process. The approach used is the Absolute Rate Theory [61], which assumes that the activation energy for the atomic migration is equal to the energy of the saddle point configuration, i.e. the maximum in the energy profile for the migration path relative to the energy of the point defect by which the diffusion takes place, fig.4.18.

The calculated activation energy comes from the minimization of the structure with of a fixed ion, Li^+ or H^-, at an equal distance between the corresponding

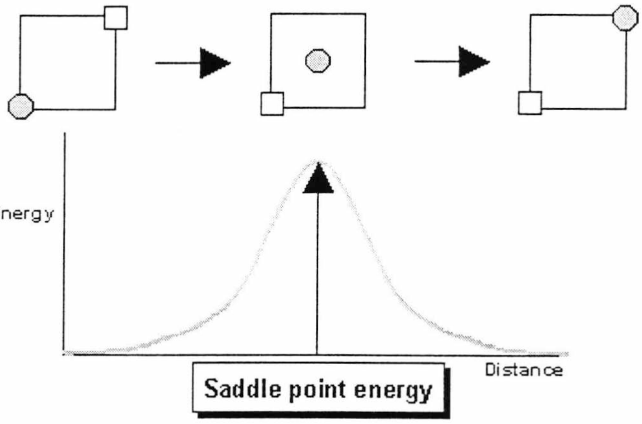

Figure 4.18: Migration profile of a generic vacancy driven mechanism

sub-lattice vacancies. This, according to the symmetry of the system must show the maximum energy, i.e. the saddle point energy, for the diffusion path. The comparison with experimental results, table 4.11, is very good for all our models. The Li^+ diffusion *via* a vacancy mechanism is the charge transport responsible species for LiH at room temperature. Calculations were all performed with the same regions sizes used in the isolated defects calculations, and the regions were centred on the *diffusing* ion.

	Islam	Rigid	Set I	Set II	Exp.
E_a H^-	0.38	0.77	0.72	0.84	≈ 1
E_a Li^+	0.39	0.50	0.46	0.51	0.54 ± 0.02 [56, 57, 59]

Table 4.11: LiH calculated and experimental defect diffusion activation energies The Islam potentials results are re-calculated with our conditions

4.3.2.3 Comparison of defect results as a function of potential set

In table 4.12 we show the configurational energies obtained for single defects with respect to the perfect crystal. For instance the Li^+ vacancy value is the difference of the energy calculated, with all the approximations stated, between the perfect crystal and the crystal without a Li^+. It is important to notice, that physically none of these energies has a meaning by itself, since in ionic solids there cannot be single point defects due to charge neutrality constraints. Their value is, however, very useful in clarifying the obtained differences in the defect formation and activation energies obtained using different potential sets. We have added an extra potential set, called *LiH*, which yielded very similar results to the Islam one, but has been fitted by us starting from potentials in Set II to the elastic, dielectric properties and structure of LiH. In the potential determination the C value was constrained in the potential determination in order to obtain physical values for the potential parameters.

From table 4.12, it can be seen that all the single defects involving H are systematically more stable with the Islam and LiH potentials, which translates to lower Schottky and Frenkel energies. Also a H$^-$ interstitial, which is known to be much bigger than Li$^+$, appears to be more stable with these potentials. Since both ions have the same charge this is not physical, in a mechanical static minimization on an indistinct, respect to the corresponding sublattices, interstitial position. This explicitly shows the inadequacy of Islam potential or any similar potential for non perfect crystal calculations.

Defects	Islam	*LiH*	Rigid	Set I	Set II
$V_H^{\cdot}$	**6.04**	**6.48**	7.06	6.81	7.16
$V_{Li}^{\prime}$	5.89	5.75	6.14	6.64	6.25
$H_i^{\prime}$	**-3.44**	**-4.03**	-1.52	-0.24	-1.35
$Li_i^{\cdot}$	-3.19	-2.94	-3.11	-3.63	-3.02

All energies in eV

Table 4.12: LiH *single* defect energies

4.4 Defect calculations on CaH$_2$

4.4.1 α–CaH$_2$ defects

We have calculated the α–CaH$_2$ Schottky and Frenkel defect formation energies and the diffusion activation energies for hydrogen. Set II potential parameters have been chosen for this study since they give the better representation of the structure. Previous calculations with a preliminary rigid ion potential that reproduced well the structure produced basically the same defect energetics. The sizes and conditions were those used for LiH (~100 ions for region I). α-CaH$_2$ has two different H crystallographic sites, H$_1$ and H$_2$, the obtained results, table 4.13 show a small difference on anion vacancy formation energy with site, 0.05 eV.

The energy difference translates into the possibility of creating three different kinds of Schottky trios, and two kinds of H Frenkel. According to equation D.60, the number of H$_2$–Frenkel defects at room temperature is expected to be around five times the number of H$_1$-Frenkel defects.

	Absolute	Relative*		
Schottky (H$_1$-H$_1$)	6.76	**2.25**	$V_{H_1}^{\cdot}$	5.01
Schottky (H$_1$-H$_2$)	6.81	2.27	$V_{H_2}^{\cdot}$	4.96
Schottky (H$_2$-H$_2$)	6.85	2.28	$V_{Ca}^{''}$	25.35
Frenkel H$_1$	6.28	3.14	$H_i^{'}$	1.27
Frenkel H$_2$	6.23	3.12	$Ca_i^{\cdot\cdot}$	-11.39
Frenkel Ca	13.96	6.98	—	—

(*) Per single defect
All energies in eV

Table 4.13: α-CaH$_2$ structure compound and *single* defect energies

In order to assess what defect will be the most likely one, it is important to compare the energies per number of component single defects. This is a rough normalization that partly accounts for the difference in configurational entropy that arises from compound defects, i.e. Schottky and Frenkel, with a different number of component defects[17].

According to these results the most stable defects would be Schottky trios, then Frenkel H, and then Frenkel Ca. However, the energy difference between both kinds of defect is rather too small, and comes from a fully ionic model. If we use experimental lattice energies instead of calculated ones for calculating the compound defects energies, Frenkel H is 0.3 eV more stable than Schottky trios. A clear conclusion for the intrinsic predominant defect cannot be drawn on these grounds.

Even for relatively pure crystals, the extrinsic conductivity region is dominated by the presence of oxygen impurities, *a priori* in the form of O^{2-}, creating vacancies, that will dominate the diffusion [33]. Doping with Li^+ increases the conductivity, supporting a mechanism of diffusion *via* a H^- vacancy mechanism. This agrees with our results, since either Frenkel H or Schottky trios will create H vacancies. This is also expected from a comparison with previous calculations on the isostructural $PbCl_2$ structure, where interstitials were not found to diffuse [47].

For the activation energy, different H–vacancy diffusion pathways have been explored in order to obtain the most likely paths. The values obtained are for linear pathways, however these energies are not expected to differ much from non-linear diffusion pathways due to the high packing of the α-CaH_2 structure.

The most energetically favorable paths have been linearly explored for all possible paths, yielding a range for activation energies of 0.19–0.79 eV. As expected the paths involving long distances are energetically unfavoured[18]. The more favourable pathways are the site exchange ones, $H_2 \rightarrow V_{H_1}$ and $H_1 \rightarrow V_{H_2}$ (the first one being 0.05 eV more stable than the second one). The Frenkel/Schottky energies are different as a function of site and consequently the number of the

---

[17] A priori, a mathematical normalization, explicitly considering the configurational entropy term, can be worked out, however, considering the uncertainties in the defect formation energies of the model and method, this has not been undertaken.

[18] This normally implies, in highly packed structures, the presence of other species in the diffusion path.

Diff Path	Dist. /Å	Fract. Dist.*	Ea / eV
$H_1 \rightarrow V^{\cdot}_{H_1}$	2.49	**0.50**	0.59
	3.60	0.50	4.67
	3.90	0.50	3.90
$H_2 \rightarrow V^{\cdot}_{H_2}$	2.83	**0.50**	0.79
	3.21	0.50	1.68
	3.60	0.50	3.18
$H_2 \rightarrow V^{\cdot}_{H_1}$ †	2.70	**0.60**	0.31
	2.71	**0.60**	0.19
	2.86	0.50	1.37
	2.94	**0.45**	0.29

* Fractional distance relative to the perfect crystal
† All values from H_1-H_2 +0.05 eV

Table 4.14: Activation energies for linear diffusion pathways in α-CaH_2

more stable vacancies, V_{H_2}, is statistically higher than the number of the less stable vacancies, V_{H_1}. The exchange will be always favoured and almost no conduction should be expected on $H_1 \rightarrow V_{H_1}$ or $H_2 \rightarrow V_{H_2}$ paths. This is important since both favourable non-exchange paths are restricted energetically to nn jumps and this would imply a zig-zag conduction in which displacement can only be in the y direction. The expected range from conduction is predicted to be for single jumps ~ 0.19-0.35 eV. The lowest activation energy for long range diffusion would be however 0.24 eV, 0.05 eV higher. This pathway is very defined since according to the structure the vacancy can only hop to two equivalent sites on the perfect bulk crystal, i.e. forwards or backwards on all cases, this path implies diffusion in all directions.

4.4.2 β–CaH_2

4.4.2.1 Experimental evidence

The high temperature of the fast ionic transition, and the fact that there is not a fluorite structure at room temperature poses a problem in order to obtain experimentally a value for the activation energy for diffusion. However this can be indirectly estimated; it has been observed that the doping with fluorine results in a solid solution at room temperature with a wide range of compositions, $CaF_{2-x}H_x$ ($0< x \leq 1.24$) [62].

Neutron diffraction data shows a fluorite structure where the ions are statistically distributed, i.e. the structure has only one anionic site. This implies that both anions, F^- and H^-, must have a very similar ionic size[19] as opposed for instance to the CaHCl structure [63] where two different anionic crystallographic sites are observed.

The electric conductivity has been studied as a function of dopant concentration [65] and diffusion via a vacancy mechanism of H ions has been deduced (with an activation energy that extrapolates to 0.3 eV at 100 % H doping). This value is confirmed by NMR studies which give a self-diffusion energy for H of 0.45±.0.05 eV at 47% molar H doping.

4.4.2.2 Prediction of the structure at room temperature

The β–CaH_2 phase has the fluorite structure, fig. 4.19. This phase is not stable at room temperature. The α–CaH_2 phase shows a 11% denser structure[20] and it is the only stable polymorph at room temperature. The fact that both structures exist in nature shows that these are two thermodynamic minima with different stabilities as a function of temperature with a not very high kinetic barrier[21] shown by the fact that the β phase re-transforms to α on cooling. Both phases are stable in our static configurational and quasi-harmonic free energy calculations that yielded physical values for all the properties.

There is a very small change in interatomic distances, getting slightly shorter, between CaF_2 and $CaF_{2-x}H_x$, so, extrapolating to the room temperature static (otherwise unstable) β–CaH_2, the distances are expected to be very similar. Both

---

[19] There is only 1% variation of lattice parameter from pure CaF2 to $CaF_{0.76}H_{1.24}$, maximum H doping.

[20] We have taken for the comparison the CaF_2 volume.

[21] In comparison with the isomorph PbF_2 where the β phase is metastable at low temperatures showing a higher kinetic barrier.

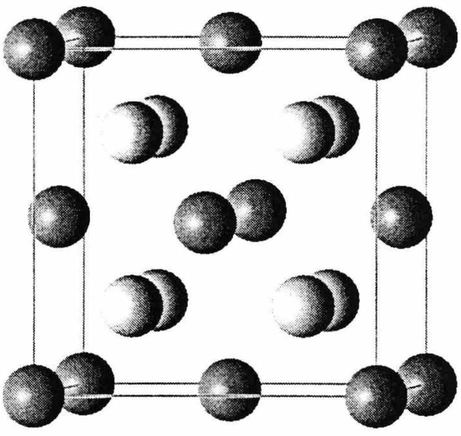

Figure 4.19: β–CaH$_2$ fluorite structure, Ca atoms darker spheres, H atoms: lighter spheres

our potential sets, set II and rigid, yielded physical values for all the properties and predicted the lattice parameter for CaH$_2$ to be $\sim$-1% different than the corresponding value for CaF$_2$. Since the difference from pure CaF$_2$, and the linear extrapolation of experimental data to, *pure* β-CaH$_2$ is -0.4%, (10^{-2} Å), the agreement is extremely good.

4.4.2.3 Defect calculations

The calculation of defects, with set II and the rigid set of parameters predicts, table 4.15, the H Frenkel as the most stable defect (as typical in fluorites). The experimental energy is assumed to be equal to the orthorombic phase as an estimate[22]. Unfortunately, there are no experimental estimates of defect formation energies for the material for comparison. However, in comparison with similar calculations on CaF$_2$ [53, 35], the defect formation energies for all defects are at least 2 eV higher, this comes specifically from the SR potentials, i.e. from the interatomic interactions, since static dielectric constants and structures are very similar in both cases. This suggests that the higher electrical conductivity at high temperatures for β-CaH$_2$ is due to a much higher mobility of the anions coming

---

[22] The difference in calculated cohesive energies between the two phases is < 1eV.

from its much lower mass.

	set II		rigid			set II	rigid
	Abs.†	Rel.‡	Abs.	Rel.			
Schottky (exp.*)	10.37	**3.46**	13.32	**4.44**	V_{Ca}''	25.97	26.61
Schottky (calc.)	6.67	**2.22**	9.66	**3.22**	$V_H^{\cdot}$	4.69	5.85
Frenkel H	4.01	**2.00**	4.35	**2.18**	H_i'	-0.68	-1.49
Frenkel Ca	10.48	5.24	13.46	6.73	$Ca_i^{\cdot\cdot}$	-15.49	-13.15

All values in eV.
(*) Values calculated using the experimental cohesive energy
(†) Absolute energies
(‡) Relative, per single defect, energies

Table 4.15: Calculated defect energetics for β–CaH$_2$ with set II and rigid set parameters

Regarding activation energies, our calculated values, table 4.16, reproduce reasonably well, the extrapolated activation energy to a 100% concentration of F-doping in CaF$_2$ [65] and that obtained from NMR H self–diffusion [33]. These are very similar to the values obtained for CaF$_2$ calculations [53, 35] with the same conditions used in our calculations, 0.27 and 0.24 eV, respectively.

	Rigid	Set II	Exp.
E_a H	0.32	0.15	0.30 [65], <45 [33]

All values in eV

Table 4.16: β–CaH$_2$ calculated and experimental defect diffusion activation energies.

4.4.3 Preliminary MD calculations on high–T β–CaH$_2$

Molecular Dynamics, MD, calculations have been performed with the program DL_POLY 2.1 [66] on High–T β–CaH$_2$. These calculations are, however, still in a preliminary stage and have not yet yielded reasonable results. First, there was a non-negligible structure (wave) in the evolution of properties against time whose cause might be coming from the choosen timestep, 1 fs, 10^{-15}s (since hydrogen is a very light atom smaller timesteps may be needed for a good description of H sublattice vibrations). The fluorite structure was found to be stable dynamically on slab and bulk configurations in the all the temperatures simulated.

Due to the lack of experimental lattice parameters for the β–CaH_2 at high temperatures, cubic supercells of 3x3x3 (324 ions) and 4x4x4 (768 ions) and 5x5x5 (1500 ions) sizes were equilibrated with the Berendsen NPT ensemble at different temperatures near and over the melting point with cutoffs increasing with cell size and runs of typically 20000 timesteps.

Some longer runs with the NVT Hoover thermostat were undertaken at 1200 K on all sizes. However, in all these cases ion diffusion was not observed[23]. A run with the system doped with Na^+ showed ionic diffusion but we doubt the values could be comparable with experiment. The basic problem is that defects did not spontaneously form in our calculations.

The explanation of this comes from the fact that Frenkel defect formation energies, since they involve the motion of atoms to interstitial positions, are very dependent on volume, which our potentials do not reproduce well at high temperatures. The temperature lattice expansion[24] is underestimated while the melting point is overestimated. Gillan [67] has explained this by running various MD simulations on the isomorph $SrCl_2$ system with different fixed volumes obtaining a very steep dependence of number of defects on cell volume.

4.5 Conclusions

We have developed two sets of potentials, rigid ion and shell-model, for ionic hydrides that seem to overcome the limitations of previous models. The use of the multifit approach has been proved crucial in the development of potentials due to the asymmetry of some of the crystallographic structures. The obtained SR potentials for the M–H interactions show qualitively the expected trend as a

---

[23] This was monitored by Mean Square Displacements, MSD.

[24] This was observed to be very small in comparison with experimental values for similar systems.

function of electronic structure.

Our potentials predict the diffusion activation energy for LiH in very good agreement with experiment, showing, in comparison with previous potential sets, the posssible limitations and caveats of using only very symmetric structures and their properties for potential determination.

The activaction energy of the *virtual* β-CaH_2 structure is also in very good agreement with experiment. From the obtained defect formation and activation energies in β-CaH_2, its much higher electric conductivity with respect to CaF_2 seems to come mainly from the higher mobility of the anion.

4.6 Future work

As a result of the present work the following studies should be fruitful:

- Calculations of defects in other crystals, for instance MgH_2, NaH.
- Neutron diffraction experiments for structure determination of β–CaH_2 to obtain the high temperature lattice parameters.
- MD simulations of β–CaH_2 and β–CaD_2 systems (see appendix C).

Chapter 5

Cation Diffusion in Olivines

5.1 Introduction

Atomic diffusion processes are of a extreme importance in the formation and history of minerals or rocks. The experimental techniques used to study this, for instance tracer diffusion and electrical conductivity measurements, do not yield direct atomic information. This results, in complex materials, in problems for data interpretation. Computer modeling can be a powerful tool to understand, explain and predict diffusion data in not highly symmetric structures [68].

Olivine is one of the most widespread silicate minerals; it is prominent in many types of meteorites, one of the most important minerals of the Earth Mantle and even occurs in the moon. Olivines are orthosilicates of the formula M_2SiO_4, where M=Mg, Mn, Fe, Ni, or Co. In nature, olivine appears with very heterogeneous concentrations of metal ions, crystals are often zoned and ionic diffusion of these ions is very important in order to understand the mechanical properties of minerals.

However, mineral samples are far from ideal to contrast with results from calculations, due, mostly, to purity and thermal history concerns. At the same time, experimental measurements have been performed at near melting point temperatures, in order to have the highest diffusion, and is it not clear how representative 0 K simulations may be.

Our study has been restricted to fayalite, Fe_2SiO_4 and forsterite, Mg_2SiO_4, where good experimental data on synthetic, pure, annealed samples are available. This allows us to test the calculations and their possible limitations in order to try to get more insight into the interatomic diffusion processes dominant in these minerals.

5.2 Structure and potentials

Fayalite and forsterite crystallize in the orthorhombic olivine structure, Pnam space group, fig. 5.20. The crystal structure has two symmetry inequivalent sites with equal number of iron/magnesium atoms, M_1 and M_2, three inequivalent oxygen sites and one silicon site.

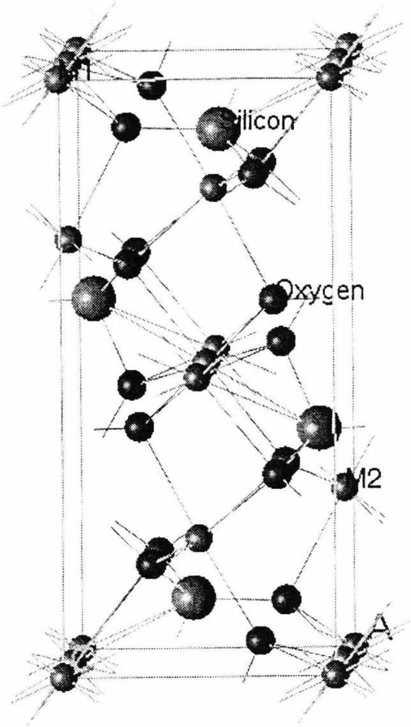

Figure 5.20: Fayalite and forsterite structure

Silicates and zeolites have been widely studied with MM methods, see for instance references [4] and [69]. Many interatomic potential sets have been derived and are available in literature. The potentials used in this study, tables 5.17 and 5.18, have been chosen based on a previous comparative study with quasi-harmonic free energy MM calculations [70].

Ions		A/eV	ρ /Å	C/eV · Å^6	Cutoff/Å
O	O	22764.00	0.149	27.88	12.000
Si	O	1283.91	0.321	10.66	12.000
Fe	O	1207.60	0.308	0.00	12.000
Mg	O	1428.50	0.295	0.00	12.000

Table 5.17: Forsterite and fayalite two body potentials

Ions	k / eV · Å^{-2}	$Y\|e\|$
O	74.92	-2.86902
Si	∞	4.00000
Mg	∞	2.00000
Fe	∞	2.00000
Ions	k / eV $\cdot rad^{-2}$	
O–Si–O	2.09724	

Table 5.18: Spring constants, k, shell charges, $Y|e|$, and three body Si–O–Si potential for fayalite and forsterite

These potentials yielded the best reproduction of structure and properties of different silicates and were derived empirically from α-quartz, [3], FeO and MgO [71]. These potentials reproduce very well the experimental structures of both systems under study, fayalite and forsterite, table 5.19:

5.3 Diffusion in olivines

5.3.1 Experimental evidence

The standard model of the point defects in fayalite involves doubly charged iron vacancies, V_{Fe}'', and electron holes, $h^{\cdot}$. All the charge must be neutral, so in a system in active equilibrium with SiO_2 we can write the following equation:

Fe_2SiO_4	exp.	calc.	diff.	diff. %
Volume/Å^3	307.424	310.181	2.757	0.9
a/ Å	4.819	4.843	0.023	0.49
b/ Å	10.479	10.480	0.001	0.01
c/ Å	6.087	6.112	0.024	0.40
Mg_2SiO_4	exp.	calc.	diff.	diff. %
Volume/Å^3	289.970	293.103	3.133	1.08
a/ Å	4.753	4.777	0.023	0.49
b/ Å	10.199	10.248	0.049	0.48
c/ Å	5.981	5.987	0.006	0.10

Table 5.19: Comparison of experimental and calculated structure of Fe_2SiO_4 and Mg_2SiO_4

$$O_2(g) + SiO_2(s) \rightleftharpoons 2V''_{Fe} + Si^{x}_{Si} + 4O^{x}_{O} + 4h^{\cdot} \tag{5.43}$$

Assuming that virtually all the electric charge perturbation in fayalite is due to iron vacancies and electron holes (for instance all the electrons go into SiO_2):

$$2[V''_{Fe}] = [h^{\cdot}] \tag{5.44}$$

From there, assuming the activity of silicon to be constant, the number of iron vacancies will depend only on the activity of O_2 [72]:

$$[V''_{Fe}] = \left(\frac{K}{16}\right)^{\frac{1}{6}} a_{SiO_2}^{\frac{1}{6}} a_{O_2}^{\frac{1}{6}} \propto a_{O_2}^{\frac{1}{6}} \tag{5.45}$$

The dependence of diffusion coefficients on oxygen pressure in experimental data with different techniques, from tracer diffusion [73, 74] to Mössbauer spectroscopy [72, 75], accords in all cases that in the polycrystalline material[1] the diffusion of iron is via a vacancy mechanism. The migration by interstitial motion is clearly ruled out experimentally. Single crystal tracer diffusion studies [74]

---

[1] Single crystal results show a different behavior, and although in this case the non presence of extra electrons at low pressures of oxygen has been shown not a good simplification [74], the reasons for the different trend at all pressures are at this time poorly understood, [76].

show that both sites must diffuse with participation of exchange of sites in order to obtain diffusion in all directions. Mössbauer experiments [72] do not deny this, showing signal broadening due to diffusion on both sites. The same model applies to forsterite [73].

5.3.2 Defects formation energies

Classical static calculations are, by far, the more feasible method of studying diffusion in these systems. Classical Monte Carlo and Molecular Dynamics techniques are not straightforward to implement due to the electronic nature of the counterpart defect of the iron vacancy.

We have calculated the defect formation energies for all the vacancies in our model, table 5.20. All the calculations were done with sizes for regions I and IIa of 7 ($\sim$ 100 atoms) and 15 Å ($\sim$ 1000 atoms), respectively.

Defects Fe_2SiO_4		Defects Mg_2SiO_4	
$V_{Fe_1}^{''}$	**23.62**	$V_{Mg_1}^{''}$	**24.51**
$V_{Fe_2}^{''}$	**25.56**	$V_{Mg_2}^{''}$	**26.44**
$V_{\ddot{O}_1}$	27.09	$V_{\ddot{O}_1}$	28.14
$V_{\ddot{O}_2}$	24.99	$V_{\ddot{O}_2}$	25.17
$V_{\ddot{O}_3}$	24.18	$V_{\ddot{O}_3}$	24.51
$V_{Si}^{''''}$	102.90	$V_{Si}^{''''}$	101.03

All Energies in eV

Table 5.20: Fayalite and forsterite *single* defects energies

The formation energies for both M sites vacancies are very different; the vacancy on the M_2 site is around 2 eV less stable then the vacancy in M_1. Brodholt [77] performed supercell LDA periodic calculations on O and Mg vacancy creation on forsterite obtaining the same qualitative trend on single vacancies energies as found here. Specifically, the isolated defect energy differences; $(E(V_{\ddot{O}_1}) - E(V_{\ddot{O}_3})) \sim 3$ eV and $(E(V_{\ddot{O}_2}) - E(V_{\ddot{O}_3})) \sim 1$ eV are reasonably reproduced by our model. However, for the M sites, he obtained $(E(V_{Fe_2}^{''}) - E(V_{Fe_1}^{''}))=$ 0.8 eV, in comparison with the 2 eV obtained with our model. Rational function optimizer defect energy calculations, undertaken in order to check the validity of the minimum[2], yielded virtually the same results. A possible explanation of this difference of the M ions vacancies could be sustained by the fact that the Mg ions are rigid ions in our model, in contrast with oxygens, and covalency[3] cannot be accounted for.

According to equation D.60 the energy difference would imply that at the temperatures experiments are performed, around 1100 °C, the number of M_1 vacancies would be of the order 10^7 times larger than the number of M_2 vacancies. In contrast, a 0.8 eV difference (LDA results) gives a more reasonable ratio, 10^3.

The value of vacancy concentration ratios for both sites, considering the experimental data that assures us that diffusion involves M_2 sites indicates that there is, very likely, a non-negligible overestimation of the M_2 vacancy energy with respect to the M_1 vacancy in our calculations of at least 1 eV for forsterite and fayalite.

5.3.3 Diffusion paths exploration methods

Iron and magnesium diffusion is expected to occur via a hopping mechanism where M^{2+} ions jump into nearest neighbour M^{2+} vacancies (giving a charge motion in the opposite direction). The jumps due to the low symmetry of the sites cannot be assumed to be linear with a saddle point in the middle of the pathway. The spatial location of the lowest energy saddle point path and/or, more important, the saddle point itself, is not straightforward. Some of the methods used for this are:

- Grid sampling.
- Coordinate constrained biased sampling.
- Transition state search.

---

[2] Gulp default minimizer, BGFS Newton-Raphson method, does not constrain the Hessian to be positive definite [10].

[3] The difference level of covalency of Mg atoms is suggested from the different oxygen coordination of Mg ions, Z_{Mg1}=6, Z_{Mg2}=8.

5.3.3.1 Grid sampling

The diffusing ion is shifted to different positions on a cube grid where it is fixed while the rest of the system relaxes. In this way an approximation, whose quality depends on how fine is the grid interval, to the ion diffusion energy hypersurface is obtained. The number of calculations by this method scales with the number of sampling points to the power 3, and, therefore, good accuracy can be computationally very expensive.

This method, was used in previous calculations of metal ion diffusion in forsterite [78]. In these calculations all the ions were fixed while the diffusing ions were moved cooperatively from crystallographic to crystallographic site. These approximations are rather crude, there is not relaxation of the structure and diffusing ions from the same cell (due to symmetry constrains) directly interact between themselves. At the same time, this is not, strictly speaking, defect diffusion, since no defect was specifically considered in the calculations.

Although, at least in the M_1–M_1 diffusion, this is relatively equivalent, under the approximations stated, to consider an M^{2+} ion diffusing to a vacancy, and in fact the path resembled the ones obtained in the present study, the obtained activation energies in the cited study were 3–4 times higher than the results of our calculations and estimations based on experimental data.

5.3.3.2 Coordinate Constrained Biased Sampling, CCBS

The biggest problem in calculating diffusion activation energies with any static model arises from the fact that since the saddle point is a maximum of energy with respect to one of the coordinates the rest of the model has to be, in all the other coordinates, to be meaningful, in a minimum. In a standard minimization procedure, unless the atom is constrained to a fixed or pseudo-fixed position it will relax on minimization to the nearest minimum, for instance, in our case, the closest vacancy. In linear diffusion paths the atom can be spatially constrained, but in low symmetry paths some partial constraint has to be undertaken.

One possibility is to constrain, one at a time, the coordinates of the diffusing atom. In this way, the atom is partially constrained and cannot move back to the vacancy. The *point* where the structure relaxes to depends strongly on the initial atomic configuration which is constructed as the bulk perfect structure with the diffusing atom at different positions on the shortest linear path between the two vacancies. This has been found to work very well in the cases where most of the displacement of the diffusing atom is on one of the crystallographic axis. However, when this is not the case, non-continuous paths that are not, at least as a whole, representative of the diffusion path in our model, are obtained.

In order to try avoid this problem we have developed an auxiliary code that calculates the next initial point considering the position of the relaxed ion in the previous point. Since, at least for small steps, consecutive relaxed structures should not differ much, in order to save computational time, the relaxed positions of the atoms of region I are conserved and used on each consecutive calculation.

However, although the final results are better than from linear guess initial points, non-continuous paths are still obtained and the diffusion path has to be constructed as a combination of different coordinates constrained paths. For this, graphical representation of the paths in conjunction with the corresponding energy profiles are used in order to find the lowest saddle point path between the two sites. Once the *joint* path has been constructed, some connecting points are added, with direct linear interpolation of diffusing atom positions in order to probe the possible presence of non-sampled energetic barriers. In the last stage of the process, all the points are put together in order to obtain the whole diffusion path.

This method has been called Coordinate Constrained Biased Sampling, CCBS, and has been developed, coded and tested by us in the present work. To our knowledge, this is a completely novel approach to study diffusion in asymmetric structures.

5.3.3.3 Transition State Search, TSS

The location of the saddle point in diffusion can be computed in a more straightforward way with transition state search, TSS, methods. In any minimization routine, the objective is to search for a stationary point whose gradient (energy in our case) is zero with respect to all the variables and all the second derivatives, forming the Hessian matrix, are all positive. Both maxima and minima show gradients equal to zero. By definition, a first order transition state represent the lowest energy pathway between two minima. Mathematically this corresponds to only one negative eigenvalue for the Hessian, one imaginary frequency, effectively minimizing the energy of the system with respect to all coordinates but one (for which it is maximized).

On its own this method does not yield any other information than the systems geometry for the transition state, whose reliability, at least in this kind of calculation, cannot be directly assessed.

At the same time, all minimization routines general problems can show. For instance the search will find the nearest, *in the search path*, first order transition state point, which might not necessarily be the saddle point. All TSS results of any complex system have to be taken with care and, when possible, thoroughly checked. In our study all the results obtained with this method are compared with CCBS results.

5.3.4 Computational details

All the calculations were performed with the regions radii used for the vacancy calculations (7 and 15 Å). Under the Mott-Littleton approach, sect. 3.2, two spherical regions are considered around a user defined centre. For single defects, the selection of the most suitable centre is, clearly, on the defect. However, for diffusion calculations on non-linear paths the location of the centre may be a matter of debate.

Ideally, the radius of region I should be such as that the differences in the energy profile with respect to the positioning of the centre are completely negligible. This is not possible with the current resources, sect. 3.2.1, but it is not required, since, as we will show, at least for this study, the differences are very small.

Since regions sizes are limited they should be located so as to include the largest mechanically distorted region in the explicitly treated volume (region I).

In the present study, for the CCBS preliminary calculations, we initially opted by centring the regions on the diffusing atom of each initial, unrelaxed, configuration. However this approach shows some intrinsic problems, for instance in vacancy diffusion, when the diffusing atom is close to a vacancy (initial or final stages of diffusion) the energies should be quite different from the ideal case since most of the mechanical relaxation will be located on the other vacancy and not very near the centre. In our case, since our region I diameter is only 14 Å, around 4 times the nn diffusion shorter distance, in the worst case changes of around 25% in the activation energy are observed. This has an obvious effect on the diffusion profiles, for instance fig 5.22 where the diffusing atom is *apparently* more stable near to the vacancy than in the vacancy itself. In practice, since the saddle point energy is mostly at a midway between sites, where the distortion is most evenly distributed, the activation energies have not been observed to change more than 0.1 eV.

In view of this, we have opted, for a fixed centre on the spatial centre of the linear diffusion. This allows direct comparison of energies and geometries with different methods.

For the cases where an impurity atom jumps into a vacancy, specifically Fe^{2+} diffusion in forsterite, the reference calculation, vacancy + impurity, is centred on the vacancy since it has been found that the substitutional Fe^{2+} produces only a very weak mechanical deformation in forsterite for both sites.

5.3.5 Iron diffusion in fayalite

There are two crystallographically and energetically different sites for iron in olivine structures, fig. 5.21.

Tracer diffusion data, [74, 73], show that, in olivines, atomic diffusion in the c direction is much more favored. According to previous calculations [77] and our results, M_1 vacancies are more stable than M_2 vacancies. Based on the energetic difference, assuming a similar entropy for both vacancies, the ratio $V_{Fe_1}^{''}/V_{Fe_2}^{''}$ is expected to be much greater than 1. Consequently, it seems very likely that this faster diffusion in the c direction should come from a $M_1 \rightarrow M_1$ sites jump, since there are more vacancies available. In table 5.21 we can see that, by far the nearest neighbour, nn, jump, is the most favored, with an activation energy of 0.67 eV (in the range of the rough estimation of 0.9 proposed by Becker [72]) but very different from the cited experimental value of iron diffusion in forsterite, 2.74 eV, of Miyamoto et al. [78]. Actually, that value was taken from high temperature[4] tracer diffusion experiments where the *apparent activation energy* is the sum of the real activation energy and the energy due to the defect formation.

Initial pos.	Final pos.	Sampled pos.	E_a/eV	Dist. /Å
		Fixed diffusing atoms, linear path		
0 0 0	0.0 0.0 0.5	0.0 0.25 0.0	1.77	3.04
0 0 0	1.0 0.0 0.0	0.5 0.0 0.0	5.60	4.84
0 0 0	1.0 0.0 0.5	0.5 0.0 0.25	9.34	5.72
		Saddle point		
0 0 0	0.0 0.0 0.5	z const.*	0.67	3.38 †
0 0 0	0.0 0.0 0.5	TSS	0.67	—

(*) Constrained to z fixed

(†) Distance calculated on the free path

Table 5.21: M_1–M_1 diffusion in fayalite, fractional coordinates paths

The activation energy in the non-linear path is reduced by more than 1 eV with respect to the linear path and, therefore, non-linear searches are crucial in

---

[4] Intrinsic zone of diffusion.

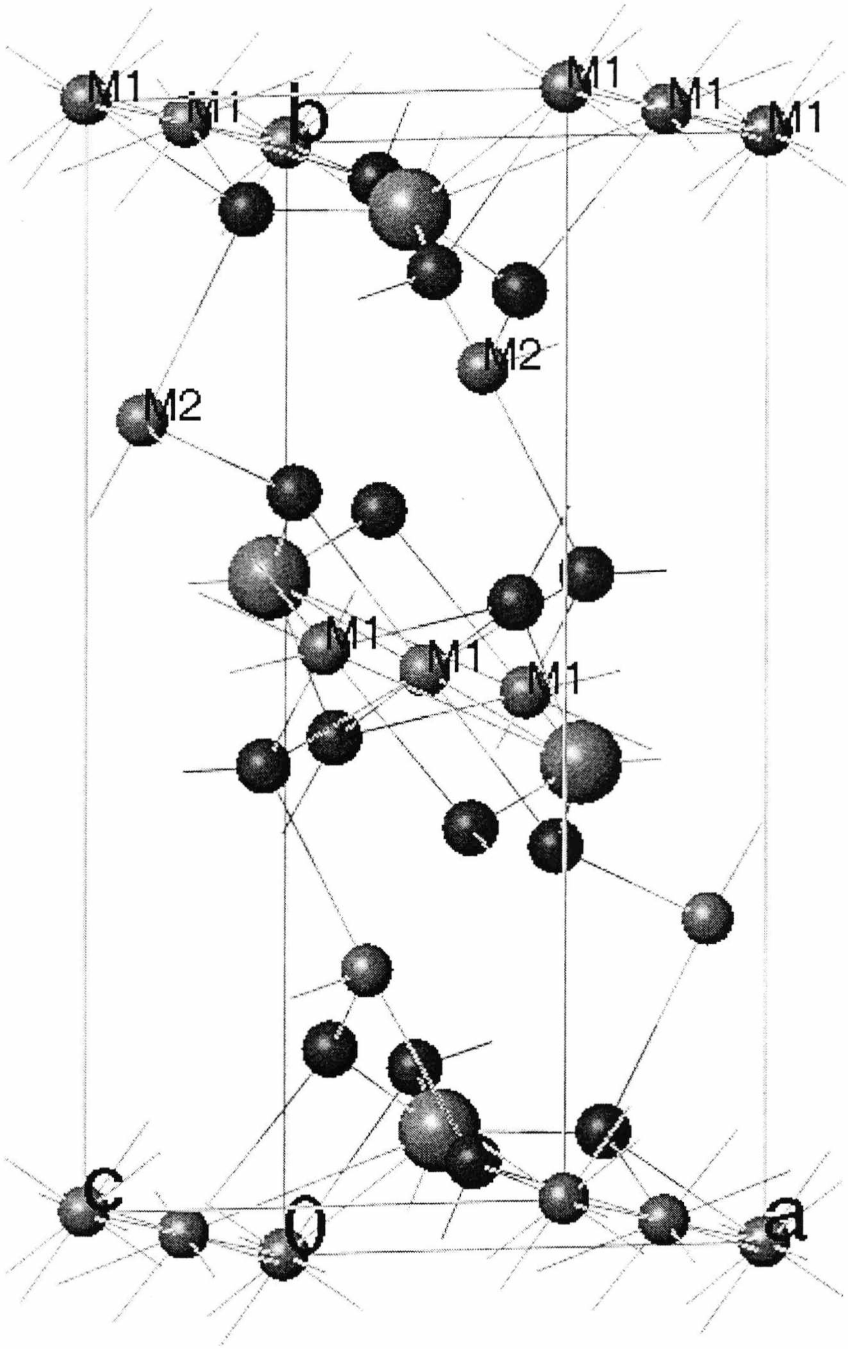

Figure 5.21: Fayalite and forsterite M_{1-2} sites

order to correctly estimate activation energies with our model. Both sampling techniques, TSS and CCBS, give virtually the same answers. Specifically, the difference in energy and saddle point Cartesian coordinates is of the order 10^{-6} eV and 10^{-5} Å, respectively, with a sampling step of 0.01 fractional. The CCBS sampling has been computed with 60 points, from 0.20 to 0.80 fractional.

With the same number of calculations and accuracy, using the grid sampling method we would construct a cubic array of 4x4x4 sampling points (i.e. only 0.12x0.12x0.12 Å^3). The coordinate constrained biased sampling is consequently much better suited for this problem.

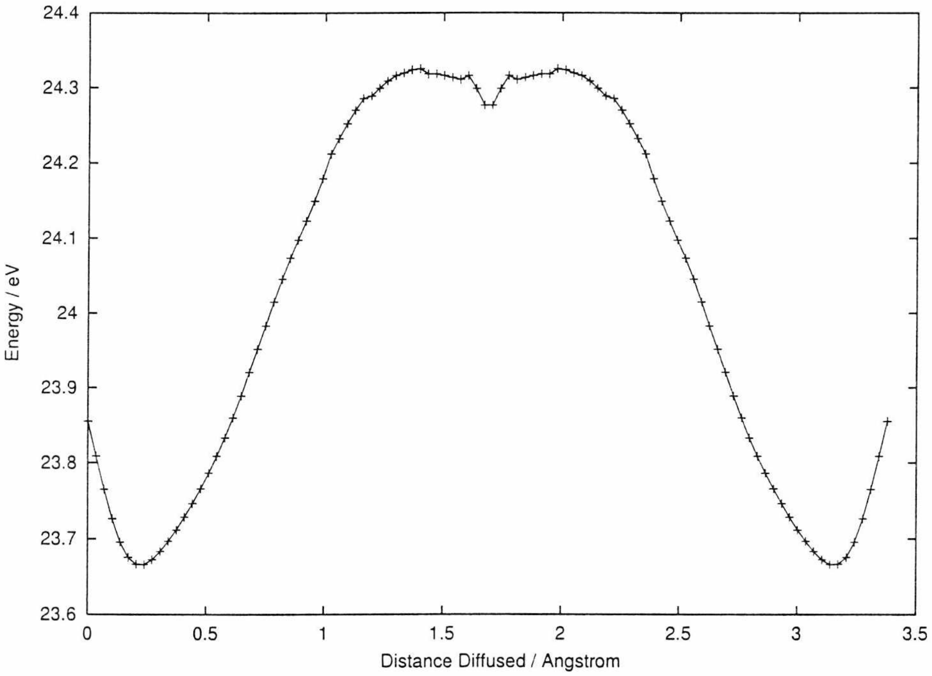

Figure 5.22: M_1–$M1_1$ diffusion energy profile in fayalite

The energy diffusion profile[5] in fig. 5.22 shows qualitative interesting features:

- Although the diffusion is symmetric, with respect to the middle point this is not a maximum suggesting a possible interstitial site[6].

---

[5] Diffusing atom centred profile, in the saddle point the difference is not significant <0.05 eV.

[6] This position is crystallographically described as a vacant cation site [78].

- The low and high distances minima are artifacts of the Mott-Littleton regions centring, see sect. 5.3.4, and only the central parts are really representative.

Migration between the M_2-M_2 sites can only be associated with two dimensional diffusion in the *a* and *c* direction[7]. Single crystal[8] tracer diffusion studies in fayalite [74] and forsterite [73] show that although diffusion is not isotropic it occurs in all three directions, *a*, *b*, and *c*, and consequently exchange of sites by iron atoms has to be possible. Three possibilities of exchange jumps have been considered at very similar distances, table 5.22, and are arbitrarily referred to as path 1, 2 and 3. The calculations result in similar features to the M_1–M_1 jumps with the non-linear path being also necessary for a good estimate of the activation energy of diffusion. The transition state search results yielded very similar results with respect to the CCBS, with a maximum difference in coordinates of 0.02 Å and in energy of 0.02 eV. This is much higher than the divergences obtained with the same sampling step on M_1–M_1, which is not surprising due to the higher complexity of these defect diffusion paths as shown by the need of joint, differently constrained, paths and the presence of more than one saddle point on the path.

TSS yielded the same number of saddle points. In order to obtain this result eight different starting points on the linear diffusion path from 0.2 to 0.8, fractional linear distances, were sampled. The fact that both, different, techniques yield virtually the same result assures us that the saddle point in our model has been correctly located.

As expected, the most likely path is between the closer sites, i.e. path 3 in table 5.22. The activation energies are very different depending on the direction of the jump, the difference being equal to the difference in vacancy formation energy of both sites. In the most favorable case the activation energy may be so low as 0.14 eV for a M_1 atom jumping to a M_2 vacancy. This activation energy is much

---

[7] The minimum distance for direct vacancy diffusion in the *b* direction is $\sim$ 6 Å, fig. 5.21.

[8] Lattice diffusion studies can only be studied in single crystals.

Fixed diffusing atoms

path	Init. pos.(Fe_1)	Final pos. (Fe_2)	E_a ($Fe_1 \rightarrow$)	E_a ($Fe_2 \rightarrow$)	Dist /Å.
1	0.0 0.0 1.0	0.50 0.22 0.75	3.00	1.06	3.645
2	1.0 0.0 1.0	0.50 0.22 0.75	3.15	1.21	3.650
3	0.5 0.5 1.0	0.50 0.22 0.75	3.18	1.24	3.348
		Saddle point			
1	0.0 0.0 1.0	const. x, z*	2.66	0.72	4.00 †
2(a)	1.0 0.0 1.0	const. y, x*	2.25	0.31	4.08 †
2(b)	1.0 0.0 1.0	const. y, x*	2.05	0.11	4.08 †
3(a)	0.5 0.5 1.0	const. y	2.09	0.15	3.75 †
3(b)	0.5 0.5 1.0	const. y	1.94	-0.00	3.75 †
1	0.0 0.0 1.0	TSS	2.66	0.72	4.00 †
2(a)	1.0 0.0 1.0	TSS	2.25	0.31	4.08 †
2(b)	1.0 0.0 1.0	TSS	2.06	0.12	4.08 †
3(a)	0.5 0.5 1.0	TSS	2.08	0.14	3.75 †
3(b)	0.5 0.5 1.0	TSS	1.92	-0.02	3.75 †

(*) Joint paths, with different coordinates fixed

(†) Distance calculated on the free path

(a) *Global* saddle point

(b) Local saddle point

Table 5.22: M_1–M_2 diffusion in fayalite, fractional coordinates paths

lower than the activation energy for the more likely M_1-M_1 jump. However, the ratio of vacancy concentration implies that the next, most likely, non-returning jump undertaken via the lowest saddle point will be M_1-M_1 and this will dominate most long range diffusion (as observed experimentally).

If we restrict diffusion to only one M_1–M_2 jump path only *c* direction diffusion is possible, so, assuming there is not any M_2-M_2 diffusion, at least two different M_1–M_2 paths jumps have to happen to explain the 3D diffusion. This is clearly shown in figures 5.23–5.25, where a projection on the plane normal to the *c* direction for each path expanded by symmetry on a 2x2x2 olivine supercell is represented.

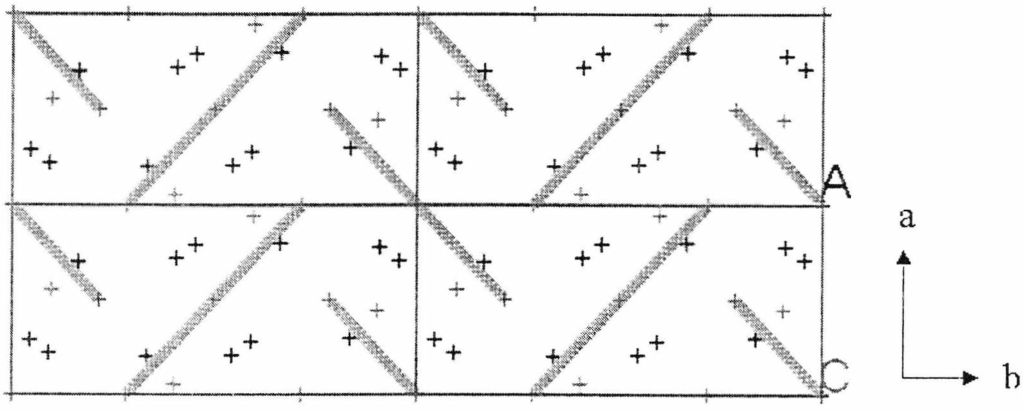

Figure 5.23: 2x2x2 cell path 1 (*initial* points)

The *a* and *b* direction diffusion site has to happen, always from jumps M_2–M_1 (very unfavored) and M_1–M_2 jumps (very favored). The simple fact that diffusion in these directions occurs in real systems strongly suggests that the values for the vacancy formation energy difference, that weight strongly the M_2–M_1 activation, difference are very probably overestimated.

A combination of paths 1-2 can account only for diffusion in the *a* direction (as can be seen from a superposition of figures 5.23 and 5.24). While paths 2-3 (fig. 5.27), or 1-3 (fig. 5.26) can account for the *b* and *a* directions. According to our results, table 5.22, 2-3 is more likely (lower saddle point, 0.3 eV) than 1-3 (0.7

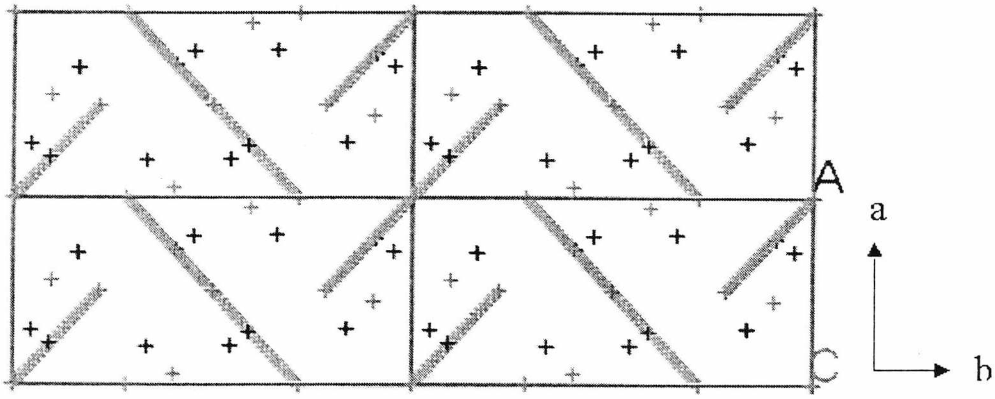

Figure 5.24: 2x2x2 cell path 2 (*initial* points)

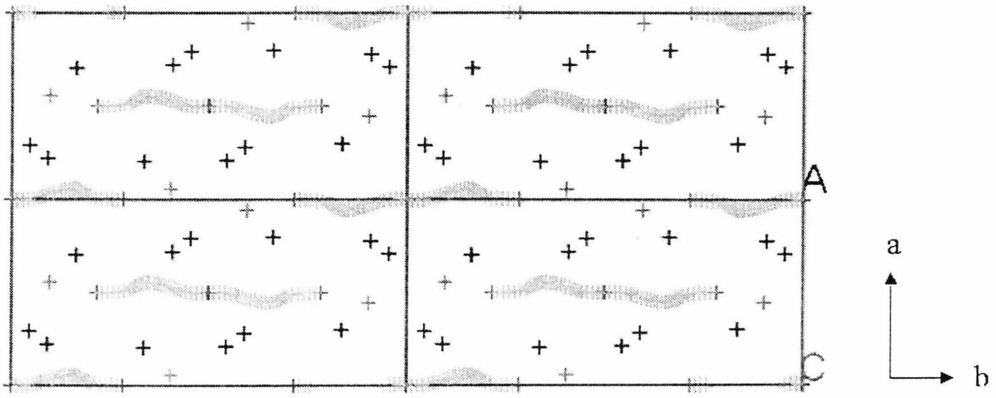

Figure 5.25: 2x2x2 cell path 3 (CCBS points)

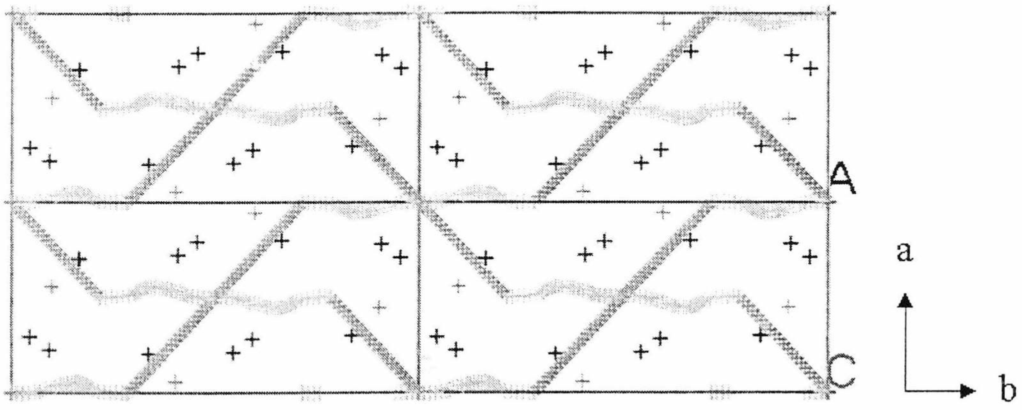

Figure 5.26: 2x2x2 cell path 1-3 (1: *initial* points, 3: CCBS points)

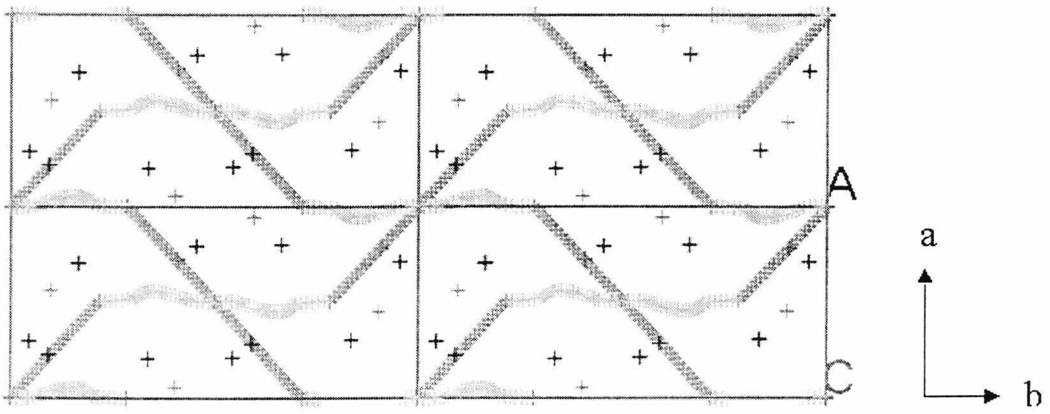

Figure 5.27: 2x2x2 cell path 2-3 (2: *initial* points, 3: CCBS points)

eV). Regardless of the energetics, geometrically, both composed paths, 2-3 and 1-3 are very similar. If no account is taken of the *c* direction motion, the cation displacement on the 3 path jump is basically in the *b* direction, while the 2 or the 1 path displaces the cations in both, *b* and *a*, directions. From this consideration alone, long range diffusion for both paths will be expected to be faster on the *b* direction than on the *c* direction. This fits with the diffusion coefficients trends experimentally observed in fayalite [74], $c > b > a$.

The diffusion profiles show the accuracy of the searches in our model, for instance for path 3, fig. 5.28, and how strongly the saddle point energy is weighted by the vacancy energy difference.

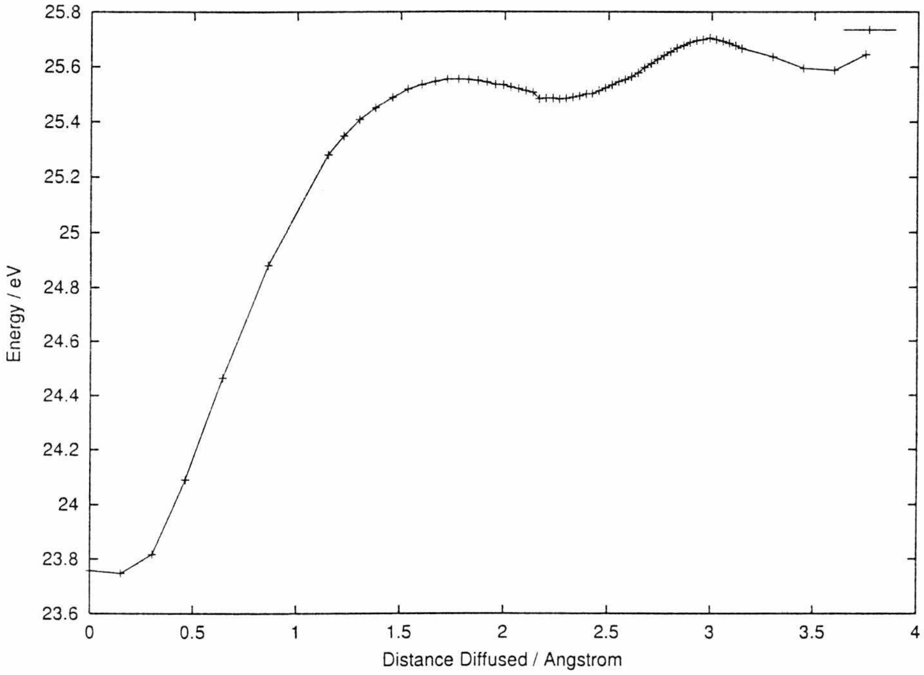

Figure 5.28: M_1–M_1 diffusion in fayalite(fractional coordinates)

The M_2-M_2 diffusion has been considered, but the lowest energy with a relaxed middle point (which does not have to be the saddle point) implies at least, an activation energy of 2.24 eV. Besides, when a M_2 vacancy is available it is more likely for an M_1 atom to jump in, since the activation energy for this process is much lower, than for an M_2 atom.

5.3.6 Magnesium and iron diffusion in forsterite

5.3.6.1 Magnesium diffusion

The same diffusion mechanism for Fe^{2+} in fayalite has been experimentally observed to operate for Mg^{2+} in forsterite [73]. In the calculations presented only the M_1–M_1 path has been fully explored, table 5.23. The activation energy for diffusion in the M_1–M_1 sublattice is 0.70 eV, very similar to the obtained value for fayalite, 0.67 eV, but slightly higher due to the lower volume (better packing) structure of forsterite[9].

Fixed diffusing atoms				
Initial pos.	Final pos.	Sampled pos.	E_a/eV	Dist. /Å
0 0 0	0.0 0.0 0.5	0.0 0.25 0.0	1.892	2.99
0 0 0	1.0 0.0 0.0	0.5 0.0 0.0	5.89	4.78
0 0 0	1.0 0.0 0.5	0.5 0.0 0.25	9.66	5.64
Saddle point				
0 0 0	0.0 0.0 0.5	TSS	0.70	—

Table 5.23: M_1–M_1 diffusion in forsterite, fractional coordinates paths

The estimated activation energies for site exchange diffusion paths are very similar to those obtained for fayalite, regardless of the different vacancy formation energy for cation sites between both crystals, table 5.20.

Linear path middle point values have been calculated for all the other paths and the results are extremely similar to the corresponding calculations in fayalite.

---

[9] This is not due to the potentials, since Volume(MgO)<Volume(FeO) which in the parameter sets used (equal formal charges) implies a more repulsive SR potential for Mg-O than for Fe-O.

Although TSS or CCBS calculations are needed to fully establish this, from these results alone it seems likely that diffusion energetics in both systems, forsterite and fayalite will be very similar.

The fact that that activation energies for both crystals are very similar, while vacancy energies diverge, shows the generally better quality of diffusion activation energies than defect formation energies (as shown by most modeling diffusion studies when compared with experiment, see for instance [11, 52, 53]).

5.3.6.2 Iron diffusion

Buening et al. [73] have observed with tracer diffusion experiments that the Arrhenius energies as a function of Fe^{2+} % doping in forsterite decreases monotonically (although not linearly) in the range of concentrations studied for all directions diffusion. From the same work the dependence on oxygen pressure of diffusion supports a substitutional impurity model regardless of doping concentration.

The substitutional solution energies for Fe^{2+} in forsterite are different on different sites, Fe_{Mg_1}=1.04 eV and Fe_{Mg_2}=0.94 eV. The difference in energy between an impurity in the perfect bulk geometry, and the impurity in a relaxed geometry amounts only to 0.03 eV for both sites showing the very small mechanical deformation due to the presence of the impurity[10].

A simulation in the dilution limit for Fe^{2+} in forsterite for the M_1–M_1 path yields a lower activation energy than any of the pure systems, 0.52 eV. This is expected with respect to the Mg^{2+} diffusion since the Fe–O potential is less repulsive than the Mg–O one. It is important to notice that activation energies for pure and doped crystals are directly comparable due to the small strain introduced by the impurity[11].

The decrease in Arrhenius energy from 10 % to 40 % mole fraction Fe^{2+} doping,

---

[10] Typical values of relaxation energy difference for interstitials and vacancies are three orders of magnitude larger.

[11] With the appropriate centre, the errors coming from the Mott-Littleton approximation are very similar in both cases.

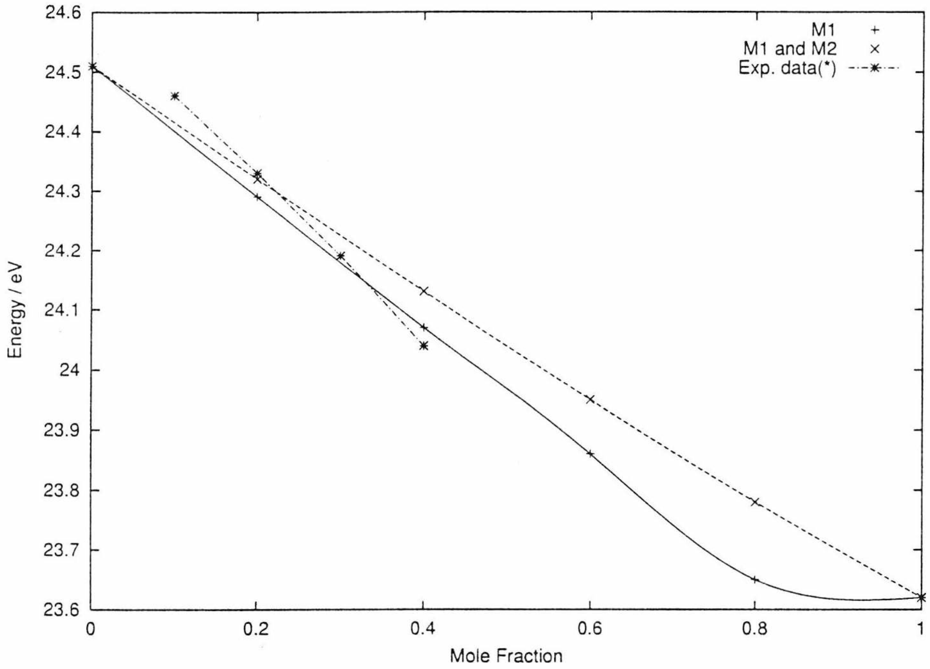

Figure 5.29: M_1 isolated vacancy energy $Mg_{2(x-1)}Fe_{2x}SiO_4$ versus x
(*) Energy arbitrary shifted by 23.05 eV

at the lowest oxygen pressure studied, for the c axis[12] diffusion is $\sim$ 0.4 eV. It is likely that the number of vacancies in the system changes with concentration of Fe^{2+} since the quantitative presence of the dopant should alter the formation energies of vacancies (fayalite cation vacancies are 1 eV more stable than forsterite ones and the volume of the unit cell[13] also changes).

We have calculated with mean field theory [10] an approximation to the M_1 vacancy formation energies as a function of Fe^{2+} concentration , fig. 5.29. Two different approaches have been undertaken in order to account for the fact that substitutional impurities are not supposed to be equally distributed in both sites[14]. In the first one, M_1 in the figure, Fe impurities are distributed only in the M_1 sites. In the second, $M_1 - M_2$ in the figure, they are equally distributed in both sites. In

---

[12] Where most diffusion will happen due to M_1 vacancies.

[13] The fractional coordinates differ only by as much as 0.01 fractional, so both crystals are *really* isostructural.

[14] Actually the calculated difference of energy could be used to differently weight the mole % in both sites, if needed, however this would not improve the picture.

accordance with the energetics of our model, at the forsterite end, 0% Fe^{2+} doping, the M_1 is more representative while at the fayalite end, 100% Fe^{2+} doping, the $M_1 - M_2$ is more representative.

Both models yield very similar results in the range of interest and the difference in vacancy energy, ~ 0.4 eV, is very similar to that observed experimentally confirming the model of an increased number of vacancies with the addition of iron to forsterite.

5.4 Conclusions

We have calculated the activation energy for different diffusion paths of iron in fayalite via a vacancy mechanism. Two different sampling methods, TSS and, the novel, CCBS, have been tested in order to locate the saddle points for Fe^{2+} diffusion paths yielding virtually the same results.

The model used, although very likely overestimating the vacancy formation energy difference[15] between the M_2 and the M_1 sites, and hence part of the activation energies, agrees well with all the available experimental data. Our calculations, agreeing with previous LDA calculations, predict a larger number of M_1 vacancies than M_2 vacancies for forsterite and fayalite, and therefore affirm that most of the atomic jumps in both crystals will involve M_1 vacancies.

Also, for single crystals of fayalite with only point defects, at least two different site exchange jumps, M_1-M_2, have to occur in order to observe diffusion in all directions, the geometry of these jumps explains qualitatively the trend in the diffusion coefficients for each crystallographic axis. M_2–M_2 jumps are found energetically not to be likely. Forsterite site-exchange diffusion has been partially studied and similar diffusion processes are expected. The trend of experimental Arrhenius energies of the $Mg_{2(x-1)}Fe_{2x}SiO_4$ system as a function of x is explained by the decrease in vacancy formation energy due the presence of Fe^{2+}.

---

[15] The relative defect formation energy.

Chapter 6

Cu clustering on CeO_2

6.1 Introduction

CeO_2 is a widely used catalyst, see [79] and references therein. In its most important application, it is added to exhausts, with Pd, Pt or Rh metals, to convert toxic unwanted products from internal combustion engines to harmless molecules.

The catalytic yield of CeO_2 increases when doped with copper [80, 81, 82]. At the same time, very recent studies show that the copper doping in ceria allows direct oxidation of different hydrocarbons in a solid-oxide fuel cell[1] [84] without carbon formation problems or poor power densities, forming the nucleus for a possible new generation of fuel cells.

Copper enters ceria as Cu^{2+}, a paramagnetic species. The local environment of Cu^{2+} in ceria has has been thoroughly studied with EPR techniques [85, 86]. In spite of the extension of the cited experimental work, the results have been interpreted with very qualitative models. The objectives of this work are two-fold: first to model different structures of Cu^{2+} defects in CeO_2 in order to interpret the EPR results and second to test the adequacy of the technique and potentials for the Cu/CeO_2 system for further use in surface calculations, more relevant in catalysis studies.

---

[1] Most fuel cells to date work specifically with hydrogen, a reformer being needed to transform hydrocarbons to hydrogen [83].

6.2 Pure ceria

CeO_2 appears in nature with the fluorite structure. This suggests a quite strong ionic character as also found by quantum mechanical calculations [87]. The fluorite structure can be described by a face centred cubic, FCC, cell formed by Ce^{4+} ions with a cubic primitive cell inside of side $a/2$ formed by 8 O^{2-} ions, fig 6.30. In this structure the cations are coordinated by 8 O^{2-} forming a cube while the anions are coordinated by 4 Ce^{4+} forming a tetrahedron.

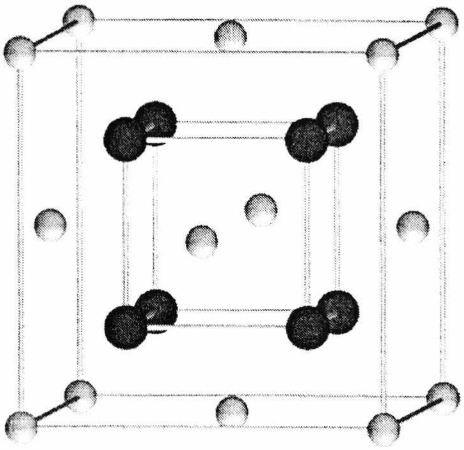

Figure 6.30: CeO_2 structure

Due to the technological importance of ceria quite a few simulation works have been reported to date [87]–[102] of which, justified by the complexity of the electronic structure of cerium, atomic cerium has f orbitals that are difficult to treat, only a small proportion are devoted to quantum mechanical simulations, [87, 88].

We have used the potential set due to Sayle et al. [89], which includes also a Ce^{3+}–O potential derived from electron gas calculations. The originally published potential set has been slightly modified, as in [90, 93, 94] where the van der Waals' C_{O-O} parameter has been set so that that the O–O potential is equal to the Lewis O–O potential [71]. This allows us to use other M–O potentials from the

Lewis set and specifically the Cu-O potential due to Baetzold [103]. The modified potential set, tables 6.24 and 6.25, has been shown to reproduce very well ceria bulk properties and structure [94].

Ions		A/eV	ρ /Å	C/eV · Å^6	Cutoff/Å
O^{2-}	O^{2-}	1986.83	0.3511	20.40	12.000
Ce^{4+}	O^{2-}	22764.3	0.1490	27.89	12.000
Ce^{3+}	O^{2-}	1731.62	0.36372	14.43	12.000
Cu^{2+}	O^{2-}	3799.3	0.24273	0.00	12.000

Table 6.24: CeO_2 potential set

Ions	k / eV · Å^{-2}	$Y|e|$
O^{2-}	419.874	-6.1
Ce^{4+}	291.75	7.7
Ce^{3+}	291.75	7.7

Table 6.25: Spring constants, k, and shell charges, $Y|e|$, for CeO_2

6.2.1 Defects in ceria

Ceria is used as an "oxygen storage" material since it can change its oxidation state with the redox properties of the surrounding atmosphere; Ce^{4+}, which exists under oxidizing conditions, can be transformed to Ce^{3+} under net reducing conditions and vice versa. In mild oxidizing conditions the defects formed involve the Ce^{3+} species, a polaron[2].

The polaron trio ($2Ce'_{Ce} + V_O^{\cdot\cdot}$) forms according to the chemical reaction:

$$O_O^X + 2Ce_{Ce}^X \rightleftharpoons \frac{1}{2}O_2(g) + V_O^{\cdot\cdot} + 2Ce'_{Ce} \qquad (6.46)$$

The calculation of the polaron trio formation energy is done according to the following thermodynamic path [99]:

---

[2] An electron hole trapped on a cation.

1. 2 x isolated defect energy for a polaron, mechanical relaxation (74.40 eV):

$$2Ce_L^{4+} \rightarrow 2Ce_L^{3+} \tag{6.47}$$

2. 2 x the 4th Ionization Potential of Ce (-73.44 eV):

$$2Ce_{\infty}^{4+} + 2e_{\infty}^{-} \rightarrow Ce_{\infty}^{3+} \tag{6.48}$$

3. Isolated O vacancy energy formation, mechanical relaxation (16.59 eV):

$$O_L^{2-} \rightarrow O_{\infty}^{2-} + V_{\ddot{O}} \tag{6.49}$$

4. First + second electron affinities of O (7.29 eV):

$$O_{\infty}^{2-} \rightarrow O_{\infty} + 2e_{\infty} \tag{6.50}$$

5. 1/2 O_2 dissociation energy (-2.58 eV):

$$O_{\infty} \rightarrow \frac{1}{2}O_2(g) \tag{6.51}$$

Where L is on a lattice site and ∞ at infinite separation.

The calculated defect energies were obtained with with regions I and IIa radii of 11 ($\sim$ 900 ions) and 24 Å ($\sim$ 8000 ions), respectively. The most stable defect is the polaron trio (2.56 eV per forming defect). However this depends on the surrounding atmosphere of the sample, and in non-reducing atmospheres the oxygen Frenkel defects are predicted to dominate, (3.77 eV per forming defect).

6.2.1.1 Comparison with previous studies

Our results for the polaron vacancy trio formation energy (7.67 eV) do not compare too well with the value published by Sayle et al. [99] with mostly the same

	Absolute	Per defect
Schottky trio	19.87	6.81
Frenkel Ce	26.80	13.40
Frenkel O	**7.53**	**3.77**
Anti Schottky	22.00	7.33
$2Ce'_{Ce} + V_{O}^{\cdot\cdot}$	**7.67**	**2.56**

Table 6.26: CeO_2 defect formation energies

potentials and thermodynamic data (6.58 eV). Test calculations with GULP with the very same potentials and cutoffs and region I radius as reported yielded for the oxygen vacancy a similar energy discrepancy. This might come from software implementation[3] or a more inexact treatment of region IIa and/or IIb.

6.3 Cu^{2+} clustering in ceria

6.3.1 Experimental evidence

A few papers have been devoted to study the local structure of Cu^{2+} in ceria with EPR [85, 86] from which the following observations were obtained:

- Cu^{2+} ions are not very soluble in ceria, at a relatively low dopant content the copper ions segregate to form a CuO phase.
- In all investigated Cu/Ce doping ratios, 0.01–1, different signals EPR are observed due to Cu^{2+} monomers, dimers and clusters.
- Under reducing (hydrogen) conditions the signal due to Cu^{2+} dimers and monomers disappears to reappear on reoxidation.
- The EPR signal due to Ce^{3+} disappears on doping with Cu^{2+}.
- In the dimer the Cu^{2+} atoms are at an average distance of 3.6±0.3 Å for all Cu/Ce ratios studied and seem to be bridged by oxygens.

---

[3] CASCADE [104].

- The dimer is not observed in samples prepared under no-oxygen atmosphere.

In the cited papers, the dimer configuration was explained based on a Cu^{2+} substitutional model, since the distance between the closer Ce atoms in the perfect bulk is very similar to the obtained distance, 3.6 Å. However, when no structural relaxation due to presence of the defects is considered, the two closer interstitial atoms will appear at exactly the same distance, fig. 6.31. Calculations of clustering of defects must be performed in order to clarify which will be the most stable dimers.

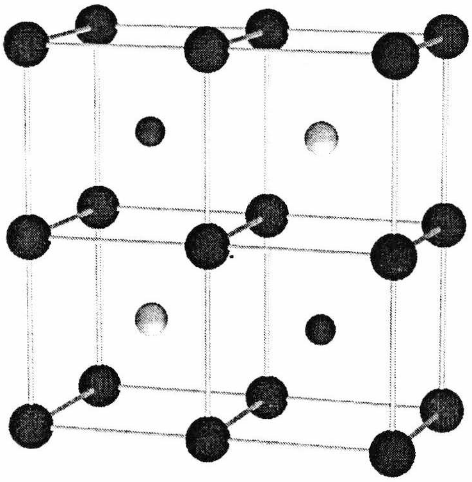

Figure 6.31: CeO_2 + 2 interstitial atoms

6.3.2 The Cu-O potential

Interactions regarding Cu^{2+} are difficult to treat with a simple spherical Buckingham potential. The first coordination shell of the Cu^{2+} ion is distorted due to the Jahn-Teller effect; in the monoclinic phase of CuO, for instance, the distortion amounts to a difference of Cu-O distances of 0.8 Å. Actually, the multifit method, sect. 1.4.4, was developed in order to try to reproduce the structure of CuO with Buckingham Cu-O and O-O potentials without success. So far, no constant pressure MM simulation with Buckingham or three body potentials has been able to correctly reproduce the CuO structure. We have used the Cu-O Buckingham potential due to Baetzold [103]. This potential, table 6.24, was empirically fitted to $YBa_2Cu_3O_7$, where the Cu–O distances show the Jahn-Teller effect distortion[4].

Although preliminary calculations for bulk CeO_2 were performed with other potentials sets; Minervini et al. [92] and Bush et al. [30], with success, the need of Cu-O and Ce^{3+}–O potentials constrained the simulations to the potential set used.

6.3.3 Cu^{2+} solution Energies

The Cu^{2+} impurity may enter the CeO_2 on two different sites, substitutionally, i.e. on a Ce^{4+} site, eq. 6.52, or interstitially, the latter with charge compensation either by polarons, eq. 6.53, or by O interstitials, eq. 6.54.

$$CuO + Ce_{Ce}^{X} + O_{O}^{X} \rightleftharpoons V_{O}^{\cdot\cdot} + Cu_{Ce}^{''} + CeO_2 \qquad (6.52)$$

$$CuO + 2Ce_{Ce}^{X} \rightleftharpoons \frac{1}{2}O_2(g) + Cu_{i}^{\cdot\cdot} + 2Ce_{Ce}^{'} \qquad (6.53)$$

$$CuO \rightleftharpoons O_{i}^{''} + Cu_{i}^{\cdot\cdot} \qquad (6.54)$$

The results, table 6.27, show that Cu^{2+} will enter the system interstitially compensated by 2 polarons (2.91 eV per defect). In oxidizing conditions, however, the equilibrium is displaced and interstitial O compensation will dominate (4.10 eV per defect). The substitutional copper is the least likely one (5.45 eV per defect).

In order to test this calculations with a known system, we have performed Ca^{2+} doping calculations, where the energies obtained show, that as observed experimentally, in an oxidizing atmosphere, the Ca^{2+} ion will enter the ceria on

---

[4] Although, due to the higher number of potentials in this system, part of the distortions must be subsumed in the other potentials. This potential could not reproduce the CuO structure.

	Absolute	Per defect
$Cu_i^{\cdot\cdot}$ (comp. 2 Ce'_{Ce})*	8.74	**2.91**
$Cu_i^{\cdot\cdot}$ (comp. O_i'')†	8.21	4.10
Cu_{Ce}'' (comp. $V_O^{\cdot\cdot}$)‡	10.91	5.45
$Ca_i^{\cdot\cdot}$ (comp. O_i'')†	10.40	5.20
Ca_{Ce}'' (comp. $V_O^{\cdot\cdot}$)‡	8.42	**4.21**

(*) Cu^{2+} interstitial compensated by two polarons
(†) Cu^{2+} or Ca^{2+} interstitial compensated by an oxygen interstitial
(‡) Cu^{2+} or Ca^{2+} substitutional compensated by an oxygen vacancy
All energies in eV

Table 6.27: Solution energies of Cu^{2+} and Ca^{2+} in CeO_2

the cation site.

6.3.4 Cu^{2+} clustering

6.3.4.1 Clusters geometry

The defect clusters presented have been constructed considering that, for the unrelaxed cluster, the distance between clustering defects has to show the minimum Cu^{2+}–Cu^{2+} distance and minimum (charge-compensating-defect)–Cu^{2+} distance. With this constraint in some cases there are more than one possible arrangement of defects on the cluster. These are referred as (i) for the more compact clusters, i.e. the cluster where defects have overall minimum distances, and (ii) and (iii) for the less compact ones. It is important to notice that due to the high symmetry of the system the number of possible configurations for dimers and trimers is restricted and can be considered statically (and minimized with symmetry constraints). Below we show figures of the different starting points. This is relevant since we are interested in a sampling of the most representative starting points, the final geometries, apart of the Cu^{2+}–Cu^{2+} distance, lack specific interest.

For interstitial Cu^{2+} compensated with O^{2-} interstitials we have considered 1 monomer (1 Cu^{2+} + 1 O^{2-} interstitial), 4 dimers and 1 trimer Cu^{2+} configurations, figures 6.32–6.36 (the Cu^{2+} atoms are the dark small spheres).

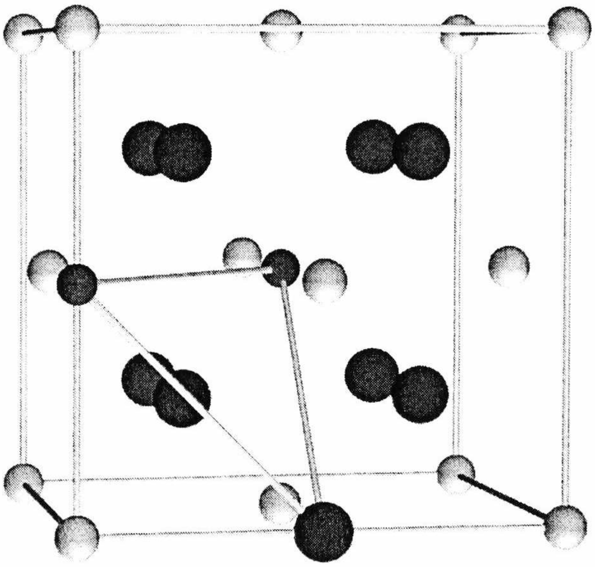

Figure 6.32: 2 $\text{Cu}_i^{\cdot\cdot}$ + 1 O_i'' cluster

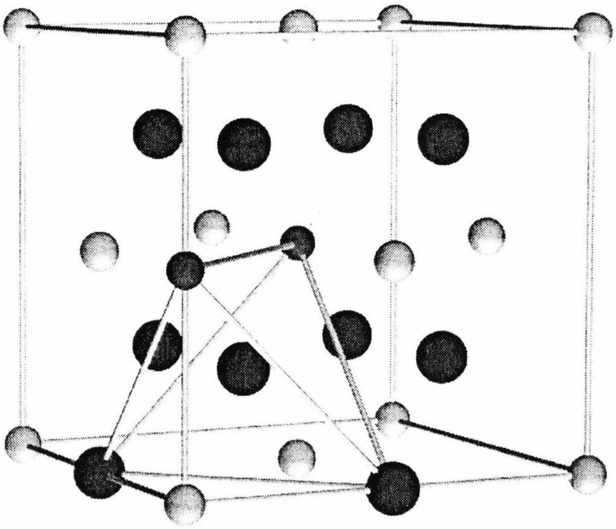

Figure 6.33: 2 $Cu_i^{\cdot\cdot}$ + 2 O_i'' (I) cluster

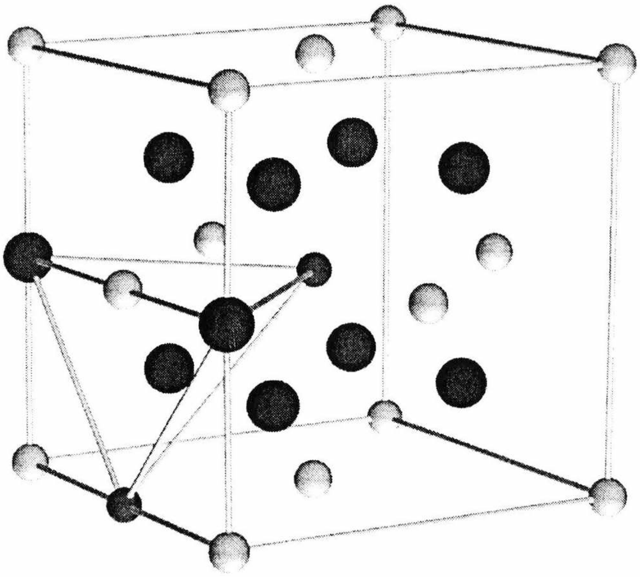

Figure 6.34: 2 $Cu_i^{\cdot\cdot}$ + 2 O_i'' (II) cluster

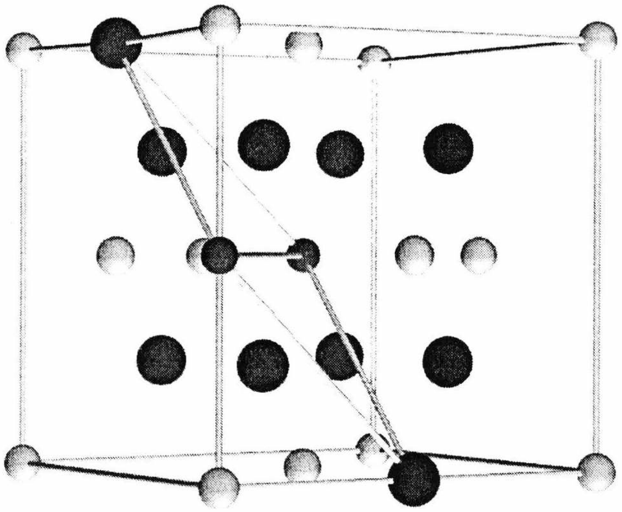

Figure 6.35: 2 Cu$_i^{\cdot\cdot}$ + 2 O$_i''$ (III) cluster

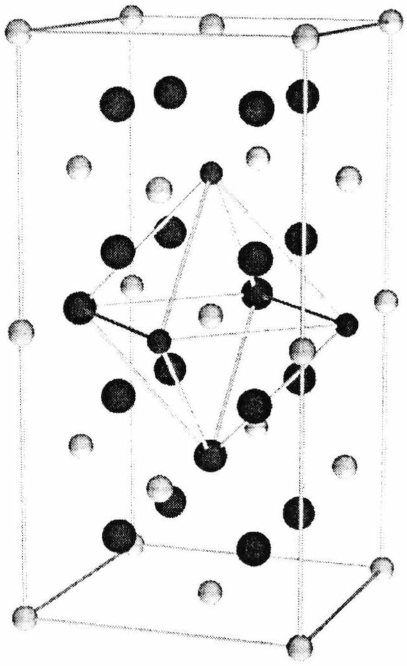

Figure 6.36: 3 Cu$_i^{\cdot\cdot}$ + 3 O$_i''$ cluster

For interstitial Cu^{2+} compensated with polarons we have considered 1 monomer and 3 dimers, figures 6.37–6.40 (the Cu^{2+} atoms are the dark small spheres and polarons, Ce^{3+}, are the small light spheres):

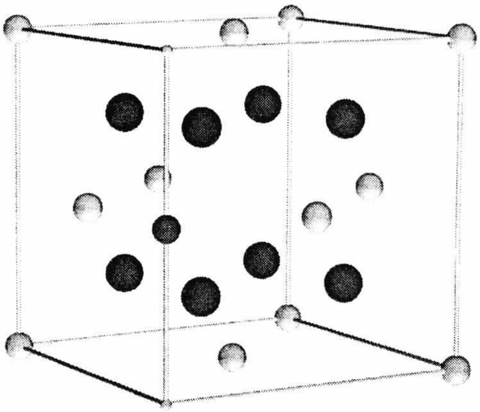

Figure 6.37: 1 $\mathrm{Cu}_i^{\cdot\cdot}$ + 2 Ce'_{Ce} cluster

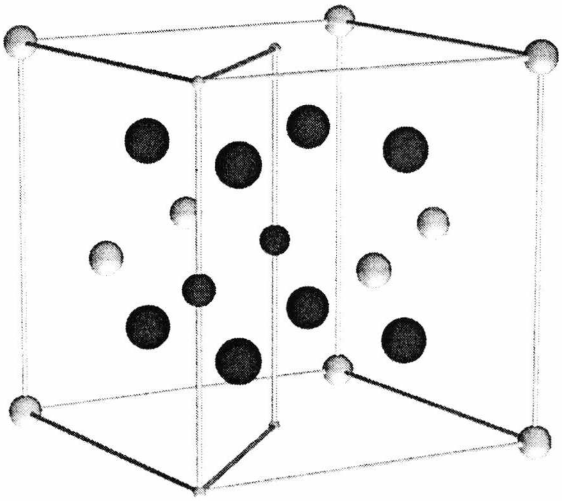

Figure 6.38: 2 $\mathrm{Cu}_i^{\cdot\cdot}$ + 2 Ce'_{Ce} (I) cluster

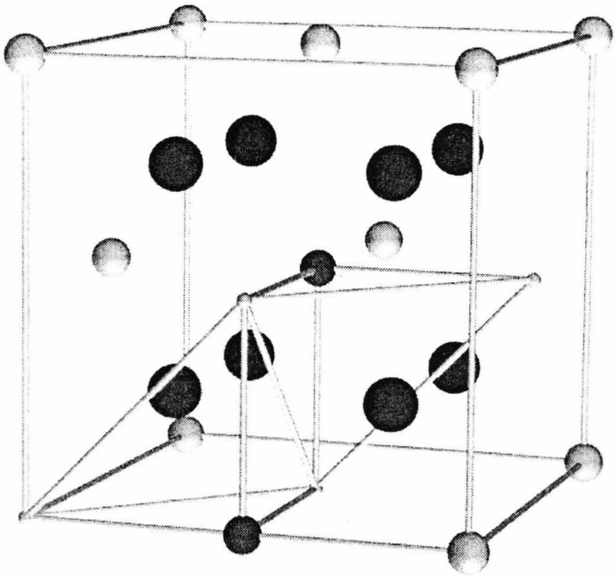

Figure 6.39: 2 $Cu_i^{\cdot\cdot}$ + 2 Ce'_{Ce} (II) cluster

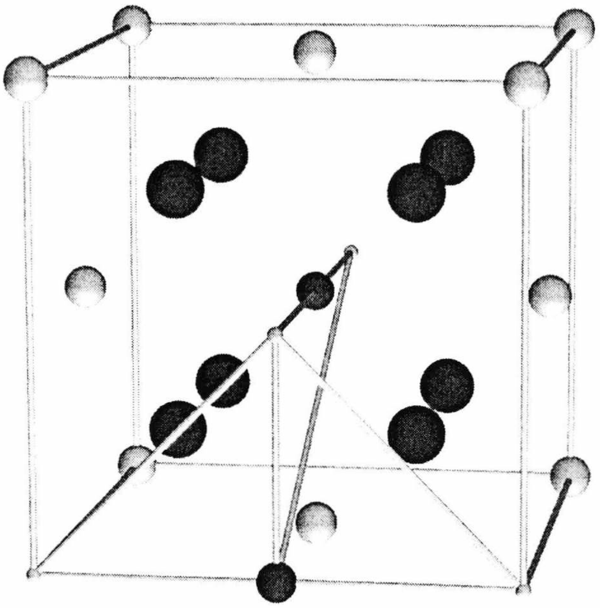

Figure 6.40: 2 $Cu_i^{\cdot\cdot}$ + 2 Ce'_{Ce} (III) cluster

For substitutional Cu^{2+} compensated with vacancies we have considered 1 monomer and 2 dimers, figures 6.41 and 6.42 (the Cu^{2+} atoms are the dark small spheres):

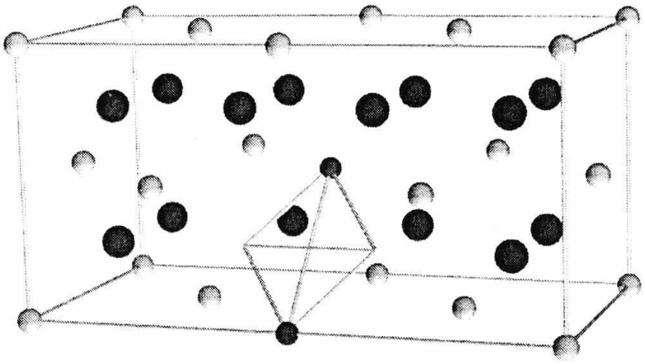

Figure 6.41: 2 Cu_{Ce}'' + 2 $\mathrm{V}_{\ddot{O}}$ (I) cluster

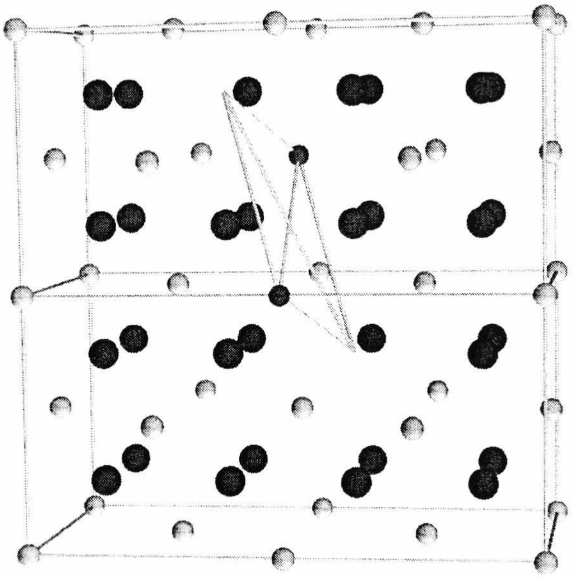

Figure 6.42: 2 Cu_{Ce}'' + 2 $\mathrm{V}_{\ddot{O}}$ (II) cluster

6.3.4.2 Clustering energetics

The Cu^{2+} clusters have been calculated with the same regions sizes used for the isolated defects. The centring of the Mott-Littleton regions has been chosen in all cases so as to maximize the symmetry of system to decrease the number of variables to optimize. Due to the size of the larger clusters an uncertainty is expected in the comparison of energies between clusters. Specific calculations with much smaller regions radii have been performed and will be commented upon in sect. 6.3.6. The clustering energy is calculated as the difference in energy between the defect cluster and the isolated defects. A negative value indicates that the cluster is more stable than the isolated defects while a positive energy indicates the opposite.

Clustering of defects reduces the configurational entropy of any given system, and, consequently, it is normally found only at low temperatures. Our calculations produce only configurational energies (very similar to enthalpies) and no account has been taken of different configurational entropies of different clusters. According to this, clustering energies are only directly comparable when formed by the same number of defects, since in this case the configurational entropy is equal.

From table 6.28 some conclusions can be drawn. For dimers, the neutral, more compact, (i) clusters dominate in all cases except for 2 $Cu_i^{\cdot\cdot}$ + 2 $O_i^{\prime\prime}$ (iii). However in this case both, initially different clusters, (i) and (iii), on relaxation converged to a common geometry. The higher cluster binding energy for dimers is in the vacancy case. From this it would seem that these are more favored, however, when the cluster formation energy, i.e. the energy needed to form the isolated defects + the binding energy, is considered, the energies are very similar, the interstitial dimer energy being slightly lower, table 6.29. It is important to note, that the cluster formation energy per defect for the polaron compensated case is not directly comparable, due to the number of different defects clustering and consequently the different configurational entropy, to the other clusters values.

Cluster	Clustering energy	per defect	Cu^{2+}–Cu^{2+} dist./ Å
1 $Cu_i^{\cdot\cdot}$ + 1 $Cu_i^{\cdot\cdot}$	1.17	0.58	3.77
1 $Cu_i^{\cdot\cdot}$ + 1 O_i''	-1.66	-0.83	—
2 $Cu_i^{\cdot\cdot}$ + 1 O_i''	-1.52	-0.50	3.54
2 $Cu_i^{\cdot\cdot}$ + 2 O_i'' (I)	-3.88	**-0.97**	**3.64**
2 $Cu_i^{\cdot\cdot}$ + 2 O_i'' (II)	-3.50	-0.88	4.37
2 $Cu_i^{\cdot\cdot}$ + 2 O_i'' (III)	-3.86	-0.97	3.64
3 $Cu_i^{\cdot\cdot}$ + 3 O_i''	-8.52	-1.42	—
1 Cu_{Ce}'' + 1 Cu_{Ce}''	0.39	0.19	2.94
1 Cu_{Ce}'' + 1 $V_O^{\cdot\cdot}$	-2.90	-1.45	—
2 Cu_{Ce}'' + 1 $V_O^{\cdot\cdot}$	-4.66	-1.55	—
2 Cu_{Ce}'' + 2 $V_O^{\cdot\cdot}$ (I)	-8.00	**-2.00**	**4.88**
2 Cu_{Ce}'' + 2 $V_O^{\cdot\cdot}$ (II)	-5.79	-1.45	2.85
1 $Cu_i^{\cdot\cdot}$ + 2 Ce_{Ce}'	0.04	0.01	—
2 $Cu_i^{\cdot\cdot}$ + 4 Ce_{Ce}' (I)	-0.88	**-0.15**	**3.52**
2 $Cu_i^{\cdot\cdot}$ + 4 Ce_{Ce}' (II)	-0.53	-0.09	3.19
2 $Cu_i^{\cdot\cdot}$ + 4 Ce_{Ce}' (III)	-0.41	-0.20	3.31

All energies in eV

Table 6.28: Cu^{2+} clusters binding energies in CeO_2

The value to compare with, for the polaron compensated case, is the formation energy with respect to the number of forming Cu^{2+} ions. This shows that dimers are less favored in that case than in any of the other ones.

Cluster	Clustering energy	per Cu	per defect
2 $Cu_i^{\cdot\cdot}$ + 2 O_i'' (I)	12.53	**6.27**	3.13
2 Cu_{Ce}'' + 2 $V_O^{\cdot\cdot}$ (I)	13.81	6.90	3.45
2 $Cu_i^{\cdot\cdot}$ + 4 Ce_{Ce}' (I)	16.11	8.30	2.77

All energies in eV

Table 6.29: Cu^{2+} dimers formation energies in CeO_2

The difference in cluster formation energy between vacancies and interstitials is not substantial, in comparison with the uncertainties of the method, to allow us to affirm that the interstitials would be the most likely way for Cu^{2+} ions to enter CeO_2. However, the distance found for the interstitials dimer compensated with interstitial oxygens 3.64 Å, table 6.28, is very similar to the experimentally obtained value of 3.6±0.3 Å [86], in contrast, the values for vacancy dimers are either too high, 4.88 Å (i) or too low 2.85 Å (ii).

The Cu^{2+} dimer clusters are far more stable for Cu^{2+} substitutional and O interstitial compensated Cu^{2+} interstitials defects than for the polaron compensated case. At the same time, for polaron compensation, forming neutral clusters involves a larger number of defects, further decreasing the total configurational entropy and making them even more unstable relative to the other clusters. Both factors explain the fact that dimers and larger Cu^{2+} clusters signals are not observed in absence of oxygen. In a non-oxidizing atmosphere Cu^{2+} impurities might enter the system compensated by polarons, however since the clustering energy is small and so will be the configurational entropy (relative to the other clusters) the Cu^{2+} will not cluster.

The substantially higher clustering energy for the interstitial trimer qualitatively sustains the experimentally observed formation of Cu_n^{2+}, $n > 2$, clusters.

6.3.5 Cu doping on a reducing atmosphere

The structural model proposed from EPR was partially based on the fact that the copper dopant stays in the system on reduction, i.e passes to neutral Cu, to reappear on oxidation. This, according to the authors implied that the Cu^{2+} must sit on a regular site, i.e. substitutionally [105].

Assuming the same SR interaction for Cu-O as for Cu^{2+}-O, we have calculated the energy of formation of the isolated defects for neutral Cu substitutional (86.77 eV, practically identical to the Ce^{4+} vacancy) and interstitial (1.71 eV).

The Cu interstitial does not have to be charge compensated since it is not charged, eq. 6.56. On the contrary, on the substitutional site two vacancies are needed to compensate the -4 charge, eq. 6.56. From these equations the difference in energy, per defect, comes to be 5 eV (i.e. creating the $Cu_{Ce}'''' + 2V_O^{\cdot\cdot}$ is 18 eV more expensive than creating a neutral copper interstitial). In accordance with this, neutral Cu interstitials will also be present in reducing conditions.

$$CuO + Ce_{Ce}^{X} + O_{O}^{X} \rightarrow Cu_{Ce}^{''''} + 2V_{O}^{\cdot\cdot} + \frac{1}{2}O_2(g) + CeO_2 \tag{6.55}$$

$$CuO \rightarrow Cu_i + \frac{1}{2}O_2(g) \tag{6.56}$$

6.3.6 Size effects on cluster defects calculations

All isolated defects and clusters of defects have been calculated with two different regions sizes sets, a *small* set with regions I and II radii of 7 and 15 Å, respectively, and a *large* set with regions I and IIa radii of 11 and 24 Å, respectively. Initial calculations were done with the small set, to be later repeated in the large one due to a specific concern for the very different size of defect clusters. For intrinsic defects in CeO_2 the results were fairly consistent for the calculations of both sizes, the vacancy energies showing the largest differences[5].

When comparing cluster energetics, the results show a relatively high divergence in energies (as much as 4 eV for the trimer). However both sets show in the most stable clusters, i.e. the most compact ones, a very similar trend in energies and, in all clusters, very similar dimer distances. This emphasizes the fact that not very extended clusters are quite self-compensating with respect to their own generated mechanical stress, and can be described by relatively small regions.

6.4 Conclusions

Although, in principle, the reliability of static simulations with empirical spherical interatomic potentials for a complex system like Cu/CeO_2 is not clear, the method, within the limitations of the model explains most features of the experimental results. Our calculations show that, in contrast with the models previously proposed, the most stable site for Cu^{2+} in ceria is an interstitial one compensated

---

[5] This shows that for this system the mechanical strain created by a vacancy affects a larger region.

with oxygen interstitials. The obtained distance for the corresponding dimer, 3.64 Å, is very similar to the one obtained experimentally 3.6±0.3 Å.

In non oxidizing conditions, however, polaron compensated Cu^{2+} interstitials are expected to dominate, but in this case, the clustering energy and the higher number of forming defects per dimer/cluster hinders the clustering (as observed experimentally). The interstitial site has been shown also to be the more energetically stable for Cu in strongly reducing conditions.

6.5 Future work

- Derivation of a new Cu^{2+}–O potential with a new functional form [107] that accounts for Jahn-Teller effects.
- Exploration of the reasons of the higher catalytic activity of Cu/CeO_2, with surface MM and QM calculations.

Part III

Quantum Mechanical Calculations of Small Molecules Adsorption on the SnO_2 (110) Surface

Chapter 7

Calculations on the SnO_2 (110) Surface

7.1 Bulk SnO_2

SnO_2 adopts the tetragonal rutile structure shown in fig. 7.43. The structure belongs to the space group $P4_2/mmm$ and there are two formula units per cell. The Sn cation is hexacoordinated with two O ions at 2.047 Å and four O ions at a slightly longer distance, 2.058 Å [108]

The intrinsic material is a semiconductor with a direct but forbidden band gap of about 3.6 eV [109]. Practical interest in the surface properties of SnO_2 derives from two main areas of application, as a catalyst for oxidation of hydrocarbons, and a sensor for the detection of reducing gases.

In general QM bulk optimization[1] give rutile structures that in most cases are far from ideal (although the deformations are mostly isotropic) as shown by Goniakowski et al. [110], where different gradient corrected Plane Wave Pseudo-Potential, PWPP, calculations on SnO_2 and TiO_2 gave results ranging from +4% to -4% displacements on the lattice parameters. In the same paper, this divergence has been postulated to come from the inclusion of the $4d^{10}$ in the core part of the

---

[1] Optimization of all or some of the geometrical parameters defining the unit cell.

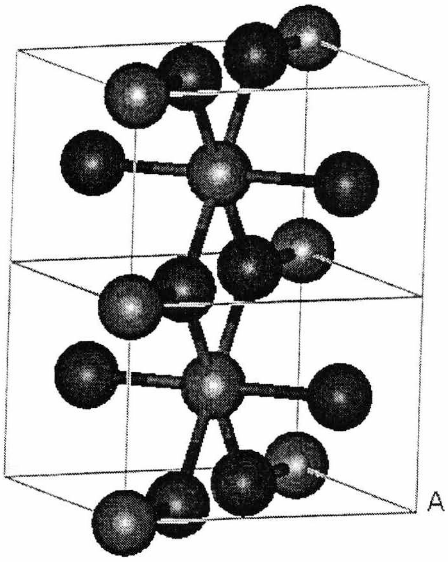

Figure 7.43: SnO_2 1x1x2 supercell

pseudopotentials, however this has been explicitly considered in other calculations [111] without any specific improvement and seems to be part of a more complex problem.

In our study the coordinates for our system are fixed, i.e. they have not been optimized, and equal to the experimental geometry obtained from neutron diffraction data analysis [108].

One of the most obvious experimental data available to corroborate our calculations, after the structure, is the band gap, i.e. the difference energy between the highest occupied band and lowest unoccupied one. Traditionally band gaps are strongly overestimated with HF methods [142] and systematically underestimated by PW-LDA calculations, ~30 % [112]; the PW-GGA approximation yields only a small improvement [113].

As a first step, we have performed calculations on unrelaxed periodic bulk under the LCAO approach with the program CRYSTAL98 [20]. The HF results overestimated by more than 200% the band gap, while non hybrid DFT methods

	Hamiltonian			
Band gap	HF	LDA	BLYP	B3LYP
Hartree	0.427	0.050	0.050	0.126
eV	11.62	1.37	1.37	3.42
Diff. Exp.	+223%	-62%	-62%	-5%

Table 7.30: Bulk SnO_2 band gaps, DFT, HF, and % difference with experiment

(LDA, BLYP) show a -62% discrepancy. In contrast the value for the B3LYP functional deviates by only -5%. This shows the good quality of this functional and its adequacy for our system.

7.1.1 Basis sets for SnO_2

Sn is a heavy metal, Z=50, and an all electron calculations would be extremely heavy on computing time. In our calculations we have adopted the pseudopotential approximation, where only valence electrons are explicitly represented and the valence-core interaction is represented by non-local pseudopotentials generated by first principles calculations on isolated atoms. In our case, the large core relativistic ECP (effective core pseudopotential) due to Hay and Wadt [114] is used. In this ECP the $1s^2$ to $4p^6$ electrons are treated as core electrons, and only the $5s^25p^2$ electrons are explicitly considered in the calculations. The basis set for Sn is [4s4p/2s2p] [114]. For the periodic calculations this had to be modified due to known convergence and quasi-linear dependence problems in CRYSTAL98, [20] due to the presence of very diffuse functions in the atomic orbitals[2]. The most external p exponent, which in the molecular case is α=0.063 in the periodic calculations has been set to α=0.1.

A d polarization function, α=0.183 [115], has been added on the adsorbing cationic site in cluster calculations and, on all Sn atoms, in the slab calculations in order to reduce BSSE effects[3], sect. 2.4.2.

---

[2] Very diffuse functions when applied to crystalline materials give a strong overlap and result in numerical instability, the *real* functions for crystalline orbitals are Bloch functions [20].

[3] The bigger the base the smaller the BSSE.

The basis set on the central Sn_{5c} atoms for the clusters and on all Sn atoms for the slabs are [4s4p1d/2s2p1d]. For the O atoms of the SnO_2 substrate we used the all electron 6-31G [116] basis set in both cluster and periodic calculations.

The effect of the d polarization function has been tested on cluster calculations of CO adsorption, with and without the function, yielding very similar results.

7.1.2 Comparing CRYSTAL98-Gaussian98 DFT results

In CRYSTAL98 [20] for DFT calculations, an auxiliary basis for the fitting of the exchange correlation potential needs to be selected. This implies that absolute energies for exactly the same systems cannot be directly compared with results obtained with Gaussian98 [26] unless the same integration functions and grids are used. This might introduce some uncertainties in the comparison of results. Consequently, in order to assess the reproducibility of data, we have thoroughly tested the CO molecule with all different DFT functionals used on periodic and cluster packages, obtaining vibrational frequencies and equilibrium geometries which were virtually the same regardless of sampling mode (largest difference $\sim$ 0.1 %).

7.2 Calculations on the SnO_2(110) surface

7.2.1 Metal oxide surfaces, general considerations

The goal of any surface structural analysis is to determine, as accurately as possible, the positions of all of the atoms in the surface and near-surface regions of the crystal. While metals and semiconductors surfaces have been widely studied, in comparison the study of metal oxide surfaces seems to lag behind. In general, geometrical structural information on oxides surfaces are particularly difficult to obtain and analyze [117] for the following reasons:

1. Only a few oxides cleave well along any crystal plane; most oxides either exhibit conchoidal fracture or have large step and defect densities on cleaved faces.

2. Attempts to prepare oxide surfaces by ion bombardment and annealing of cut-and-polished surfaces generally lead to either reconstructed surfaces or surfaces whose stoichiometry is different from that of the bulk crystal.

3. Unit cells are relatively large, resulting in much greater computational complexity for the analysis of data when compared with more simple materials.

The intrinsic difficulty of obtaining good experimental data makes simulation techniques of prime importance for oxide surfaces and their interaction with molecules.

The ideal model of a surface, the truncated bulk model, is generated by means of cleaving along a given crystal plane, leaving the atoms in exactly the same position they had in the bulk. A more realistic model would allow for rearrangement or relaxation of the surface and near surface atoms. It is possible to cleave an infinite number of different surfaces from bulk crystal by separating the crystal along any plane, no matter how large the Miller indices for that plane might be. However, it is found that most surfaces generated in this way are composed of terraced low-Miller-index planes separated by steps of single atomic height in various directions. Consequently it is better, and more feasible, to consider, when close in orientation, just the corresponding low-index faces combined with steps [117].

7.2.2 SnO_2 (100) surface

Two of the metal oxides whose surface properties have been most thoroughly studied, SnO_2 and TiO_2 have the rutile tetragonal structure, showing three different surfaces (110), (100) and (001), see [117] and references therein. The most thermodynamically stable face of the rutile structure is the (110) stoichiometric surface [118] which is constructed by the imaginary cleave that reduces the surface atoms coordination by the smallest amount. This results in a surface that is not atomically flat: rows of O dicoordinated "bridging" ions lie above the main surface plane, which contains an equal number of five and six fold coordinated cations and double number of "in-plane oxygens". Symmetric rows of O ions lie at an equal distance below the surface plane, resulting in a non-polar surface, of type II according to the categories defined by Tasker [119].

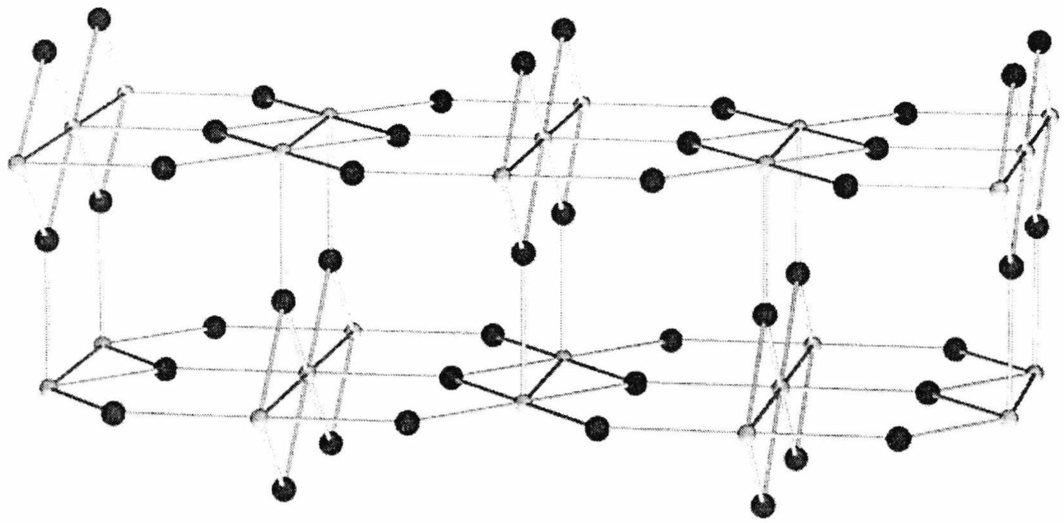

Figure 7.44: 2L SnO_2(110) slab, bigger atoms are O, smaller atoms Sn

Another kind of cleaving along this plane is also possible resulting in the (110) *reduced* surface, a polar surface of type III, so not truly stable [119], where, in comparison with the stoichiometric surface, the surface bridging oxygen have been suppressed. Our study so far has been completely devoted to the stoichiometric surface.

As a whole, the metal oxides surface most studied structures cannot be described by a simple rule, and relaxation seem to be material dependent (see [120] and references therein): on one side, there is the almost complete lack of relaxation of the MgO(100) surface as revealed by experiments and *ab initio* calculations; at the other, there are the very large atomic relaxations leading to a major reduction in surface energy found on the α–alumina basal plane surface. In this context, as we will see, SnO_2 (110) seems to be an intermediate case, showing only discrete deviations from bulk terminations[4].

As a first step, we calculated the ground state energy of truncated bulk 2D periodic slabs of different thicknesses with different Hamiltonians, HF and B3LYP, from the six atomic layers slab, to the twelve atomic layers one.

In CRYSTAL98 a slab is a semi-infinite crystal, showing periodicity only on two directions[5], x and y while in the z direction, normal to the surfaces is not replicated.

One very clear way to see a rutile crystal relative to the (110) surface, is like a stack of atomic layers perpendicular to the surface containing an O atom layer (bridging O), an Sn and O, (Sn–O) atom layer and other O atom layer, this sequence is repeated to infinity. Under this perspective, a 6 atomic layers thick slab can schematically be represented as, *O..Sn–O..O..O..Sn–O..O*, fig. 7.44. This is the thinnest slab for which meaningful results representing the (110) surface may be expected[6]. Under our periodic approach, the minimum periodic representation of this slab has 12 atoms and can be seen as a slab with two layers of Sn-O atoms, 2L. Also 3L (18 atoms) and 4L (24 atoms) slabs, have been considered.

The surface energy is defined as:

$$E_{surf} = \frac{E(n \cdot SnO_2)_{slab} - E(n \cdot SnO_2)_{bulk}}{A_{slab}} \tag{7.57}$$

where A is the slab area[7] and $E(n \cdot SnO_2)$ is the energy of n molecules of SnO_2 in the bulk or slab configuration.

As we can see in table[8] 7.31, at the HF level the difference between 2L and 3L slab is 0.03 eV, much smaller than a BSSE correction for this system, and between

---

[4] Even the gross disturbance associated with loss of surface oxygen has been shown to lead to only rather minor displacements [120].

[5] Slabs can be calculated as well with 3D periodicity, separated by a vacuum layers, this approach is used on packages that work only on 3D periodic space, for instance in the CASTEP package [121].

[6] The pentacoordinated Sn atoms in the 1L slab have a coordination of less than 5.

[7] Since the slabs are double sided, twice one of the surfaces.

[8] We consider the absolute energies in Hartree to compare with the SCF convergence in energy, $\sim 10^{-5}$, and eV to compare with binding energies. Note that all our calculations are related to the same surface area.

3L and 4L is < 0.005 eV. At the DFT B3LYP level the convergence is higher 2L and 3L slab being 0.01 eV.

Consequently at both levels of theory and for our purpose, as we will further show on the CO and CO_2 adsorption cases, the SnO_2 (110) truncated bulk surface can be represented as a 2L slab.

Hamiltonian	B3LYP	B3LYP	HF	HF	HF
Layers	2	3	2	3	4
$E_{surface}/(J/m^2)$	2.149	2.155	2.673	2.685	2.683
$E_{surface} \cdot A_{slab}/\mathrm{Hartree}$	0.210	0.211	0.262	0.263	0.263
$E_{surface} \cdot A_{slab}/\mathrm{eV}$	5.73	5.74	7.12	7.15	7.15

Table 7.31: Unrelaxed SnO_2(110) surface energies versus slab thickness

7.2.3 Comparison between clusters and periodic calculations

System	Sn_7O_{14}	Unr. 2L slab	diff.	Sn_7O_{14}	Unr. 2L slab	diff.
Hamiltonian	HF	HF	HF	B3LYP	B3LYP	B3LYP
O_{2c}	-1.035	-1.052	0.017	-0.834	-0.827	-0.007
Sn_{5c}	2.368	2.414	-0.046	1.931	1.888	0.043
Sn_{6c}	2.298	2.414	**-0.116**	2.039	1.897	**0.142**
O_{3c}	-1.224	-1.232	0.008	-1.001	-0.963	-0.038

Table 7.32: HF and B3LYP Mulliken charges, cluster versus slab

Although typical surface properties, for instance surface energy, cannot be calculated with cluster methods some easy qualitative comparisons are possible. For instance, very similar Mulliken charges have been obtained with cluster and periodic methods. This reaffirms the validity of the cluster approach for the modeling of the (110) SnO_2 surface, table 7.32. Systematic differences between clusters and slabs are observed for both Hamiltonians, specifically the differences are higher for Sn than for O, and of these the biggest appears on the Sn_{6c}, since this is a border cluster atom coordinated mostly by point charges, sect. 8.2.

7.2.4 Relaxation of the surface

The surface topology of SnO$_2$ has been investigated by various techniques [122], and depending on experimental conditions at least (1x1), (1x2) and (4x1) reconstructions were observed. It seems obvious, however, that the ideal stoichiometric surfaces appears in the (1x1) reconstruction.

Unfortunately, there are no direct experimental data for the surface relaxation of the (110) face. However, from all previous theoretical works, for instance [110] and [111], the relaxation of the SnO$_2$(110) is expected to be described by small displacements from the bulk positions.

Symmetry constraints imply that the non-reconstructive relaxation of the SnO$_2$ (110) surface can only be described by the z, (110), direction relaxation on all the atoms and the y, $(1\bar{1}0)$, directions relaxation of all the basal oxygens, see fig. 7.45.

Rantala et al. [111] have studied the relaxation of the surface on not optimized bulk with two different LDA methods, PW and LCAO, and inferred that although the z relaxation was at least qualitatively comparable the basal oxygens in-plane relaxations were very dependent on the method, a fact connected to the very different bulk relaxation, i.e. the in-cell strain. For this study, we have chosen a non bulk optimized structure where we have just relaxed the z direction on the first two atomic layers on both sides of the slab. This constraint on the number of optimized parameters comes from the fact that with the chosen package the optimizations can only be performed with numerical gradients [9].

The slab relaxation was calculated on different slab thicknesses with fixed constraints. In this process, in order to, *a priori*, save computational time and check the relative stability of different obtained minima, when possible, our initial geometry was equal to the geometry of the previous, in thickness, relaxed surface.

---

[9] CRYSTAL98 does not calculate analytical gradients, and minimizing by numerical gradients under the scheme used, conjugate gradients Polak-Ribiere method, implies a number of single points calculations at least three-fold the number of variables per optimization step.

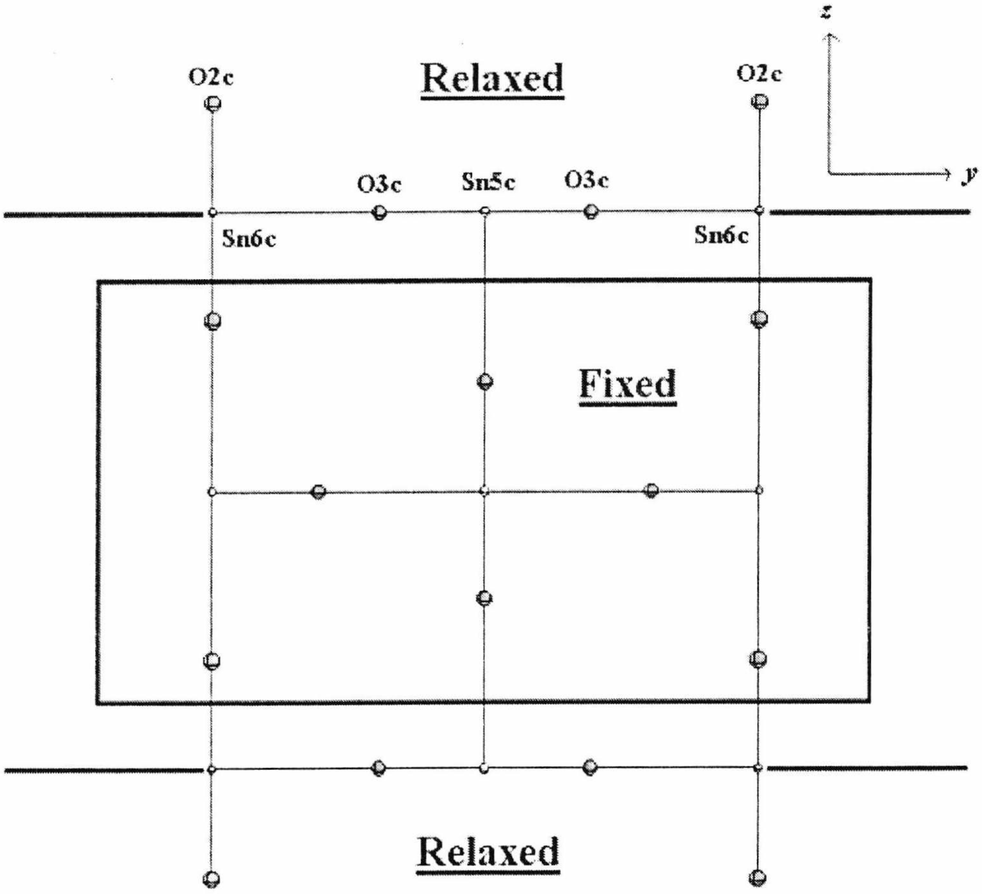

Figure 7.45: Fixed and relaxed atoms for a 2L SnO$_2$ slab representation

Convergence was, *a priori*, obtained based on two criteria, weighted gradient norm and energy difference. Convergence cannot be considered to be achieved *only* by energy difference; this was only considered when the gradients of all the variables were already converged, and the difference on geometrical parameters from previous and present step was < 0.01 Å. The gradient convergence criterion for all variables was $\leq \pm 0.15$ eV Å^{-1}. Further optimization would only change the optimized coordinates by less than 0.01 Å. This change corresponds to a change in energy <0.001 eV, one order of magnitude higher than the typical energy change in the SCF convergence step. Convergence criterion for convergence by energy difference was in most cases $< 10^{-2}$ eV.

7.2.4.1 Hartree-Fock relaxation

The HF displacements are shown in table 7.34, where the positive sign means an outward displacement, in the vacuum, while the negative one means an inward displacements, towards the interior of the crystal.

Displacements and surface energy converge with thickness with the 3L slab, tables 7.33 and 7.34. However, there is an increase of the latter from the 2L to the 3-4L. In the 2L, 4 atomic layers of 6 are allowed to relax, so the slab is quantitatively more relaxed, however there is not an internal Sn-O layer and the distance between relaxing surfaces, top and bottom, is too small so that displacements of the surfaces are quite likely correlated, and not representative of the surface[10]. In 3L-4L slabs there is at least one fixed Sn–O layer, this constraint increases apparently the surface energy, but the correlation between top and bottom layers is negligible, as shown by the similarity of both results.

At the HF level, surprisingly enough, the results of the 2L, being quantitatively different, are qualitatively similar to the 3L and 4L, suggesting that although a relaxed 2L slab is not the best representation of the oxide surface it is not very

---

[10] PW-DFT calculations of Manassidis et al. [120] on fully relaxed slabs have shown that displacements of a 2L slabs are not representative (i.e. converged with thickness) of the surface, and at least 3L slabs are needed.

different from the obtained relaxation from a thicker slab, as adsorption results on CO and CO$_2$ will show.

On the 2–3L, the effect of surface relaxation is remarkable for the five-coordinated Sn atoms which move inside by about 0.1 Å, the six-coordinated Sn atoms move outside by about the same amount while the three-coordinated O of the basal planes are displaced by 0.07 Å. All these predictions are in agreement with previous studies, from tight binding to PW techniques, see Rantala et al.[111] and [110, 120, 123]. On the contrary, at the HF level the bridging oxygens relax inside with respect to the ideal face (110) face by 0.09 Å. This is similar to the findings for the corresponding atom on the TiO$_2$(110) surface [124] but at variance with that reported in other theoretical studies on SnO$_2$ where little or no displacement of the bridging O was observed [110, 111, 111, 123].

Hamiltonian	B3LYP	B3LYP	HF	HF	HF
Layers	2	3	2	3	4
$E_{surface}$ /J · m^{-2}	1.632	1.805	1.906	2.128	2.120
$E_{surface} \cdot A_{slab}$ /Hartree	0.160	0.177	0.187	0.208	0.208
$E_{surface} \cdot A_{slab}$ /eV	4.35	4.81	5.08	5.67	5.65

Table 7.33: Relaxed SnO$_2$(110) surface energies versus slab thickness

		Δz / Å			
		Bridging	Adsorbing	Bridging	Basal
Hamiltonian	Sn-O Layers	O_{2c}	Sn_{5c}	Sn_{6c}	O_{3c}
HF	2L	-0.056	-0.164	0.207	0.093
HF	3L	-0.094	-0.121	0.131	0.072
HF	4L	-0.092	-0.123	0.133	0.072
B3LYP	2L	0.022	-0.129	0.223	0.140
B3LYP	3L	-0.019	-0.085	0.151	0.115

Table 7.34: HF and B3LYP relaxation displacements versus slab thickness

7.2.4.2 B3LYP relaxation

A preliminary B3LYP 2L optimization, where only the bridging O was free to relax, has been performed resulting in an inward displacement of 0.12 Å. On the contrary, when all the surface atoms were relaxed an outward 0.02 Å displacement was obtained, in agreement with previous studies [110, 111, 120, 123].

This basically shows that relaxation of the bridging O is strongly correlated with the relaxation of the rest of the atoms, hinting at the presence of a possible soft mode in the bridging oxygen as shown by Harrison et al. on TiO_2, [125] (for further details see appendix A).

At the DFT level, we have only considered 2L and 3L slabs, based on the HF results that show clearly that relaxation, with the imposed constraints, of the 4L slab is virtually equal to 3L slab.

The same general features obtained with HF are observed here. The relaxed surface energy, table 7.33 increases from 2-3L and the trend of variation of displacements between the two slabs is similar for both cases.

In comparison with HF, at the DFT level the displacements for the 3L slab are smaller on the inward displacements and bigger on the outward ones. Specifically, the bridging O relaxes very little inwards by 0.02 Å and so does the pentacoordinated Sn but for much a smaller amount than in the HF case, 0.08 Å, while the hexacoordinated Sn and basal O are relaxed outwards by 0.15 and 0.12 Å, respectively.

7.3 Conclusions

DFT-B3LYP bulk periodic calculations with the chosen basis sets under the LCAO approximation have reproduced very well the experimental bandgap of SnO_2. Relaxation of the surface has been studied at the HF and B3LYP levels on different thickness slabs models and has been found to be qualitatively different with both Hamiltonians. The smaller representation of the surface with a truncated bulk slab corresponds to a slab of 6 atomic layers. The smaller representation of a relaxed slab corresponds to a slab 9 atomic layers.

Chapter 8

Adsorption of CO on Acidic Sites

8.1 Introduction

CO is a prototype molecule for chemisorption studies, it is small, linear, it has only a small dipole moment, and in spite of its lone-pair electron it is a relatively weak donor. CO is widely used in surface chemistry as a probe molecule to titrate the number and the strength of acid sites of a surface [126], which is usually done by measuring the shift of the vibrational frequency of adsorbed CO compared to the gas-phase molecule. Regardless of the fact that dipole moment is wrongly estimated by single determinant HF and DFT techniques[1] [12], the interaction of CO with the surface of ionic oxides like MgO and NiO and TiO_2 has been theoretically studied with great accuracy, see [24] and therein, providing a solid basis for the understanding of the nature of the bonding and the origin of the frequency shift.

The interest of this study is two-fold; it not only provides a wealth of information about the nature of the acid sites of the SnO_2 surface, but a direct comparison with results on the same site on the isostructural TiO_2 surface [127] is possible. The comparison is of special interest due to the different electronic configuration of the two atoms, Ti: $3d^2 4s^2$ (open d shell), Sn: $4d^{10} 5s^2 5p^2$ (closed d shell) which

---

[1] Wrong modulus and direction.

results in different characteristics of the material. For instance, a weaker bonding of O ions to the surface[2] which becomes manifest on the easy removal and replacement of the bridging O in SnO_2 upon surface treatment.

8.2 Cluster embedding

The choice of cluster embedding due to the mixed character, ionic-covalent, of the SnO_2 bonding is critical. We have adopted the following strategy:

1. When possible the SnO_2 cluster contains a number of atoms in the correct ratio Sn:O, 1:2; the use of stoichiometric clusters avoids the ambiguities connected with the assignment of extra electrons to compensate the formal ionic charges of the cluster.
2. The clusters are mainly on the 2-3 first atomic layers of the surface embedded in a 4L deep array of Point Charges (PCs) that conserves the stoichiometry of the system and the symmetry of the QM cluster. The system size is the same in all cases 270 SnO_2 species, the size of the QM and PC arrays changes with clusters. The values of the PCs have been assigned to the closer integer value from calculated Mulliken charges, see table 7.32. Also, for one of the cases, the values of these charges have been consistently varied to see the dependence of the results on the PCs electrostatic field.
3. To avoid polarization of the O anion at the cluster border induced by the PCs, effective core potentials (ECP) with no associated basis functions have been placed at the position of the positive charges around the cluster in order to represent the finite size of the Sn core [23]. We have used an ECP that represents the [Kr] core ion size [114]; and in particular we used the Rb^+, Sr^{2+}, and Sn^{4+}, in connection with +1, +2 and +4 positive charges in the external region.

---

[2] Weaker bonding in general, the volume for for TiO_2 unit cell is 15% higher than the isostructural SnO_2 while the O anions are quite similar in both compounds according to [127] and the present calculations.

4. The results have been checked versus cluster size and also by a direct comparison with those of periodic calculations.

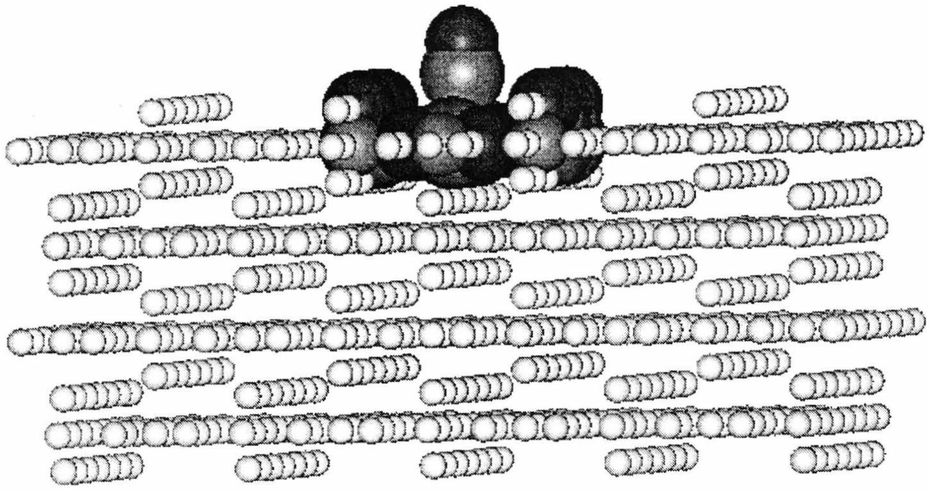

Figure 8.46: CO adsorbed on a Sn_7O_{14}–Sr_6 cluster embedded in PCs, the QM treated part is shown with bigger spheres

8.3 CO/SnO$_2$ basis set

The CO molecule has been described in all cases using a [9s5p/4s3p] basis for both C and O (DZ quality) [128]. Also in this case the inclusion of d polarization functions on C and O has been examined (DZP basis), but the calculations reported were done with the standard DZ basis. This allows a direct comparison of the present results with those obtained previously for the same molecule adsorbed on the TiO_2(110) surface [127] as well as on other substrates, MgO, NiO [129, 130], and Cu_2O [131, 132]. The SnO_2 basis set is reported on sect. 7.1.1.

8.4 CO adsorption energetics and frequency shifts

8.4.1 Unrelaxed surface adsorption

The adsorption properties of CO on SnO_2 have been calculated first at the HF level with three clusters, of increasing size embedded in (+2/-1) PCs, table 8.35. Sn_3O_7, Sn_7O_{14}, $Sn_{13}O_{26}$.

The CO molecule was adsorbed with the molecular axis perpendicular to the surface. Only CO adsorption with the C end oriented towards the surface was considered, since this is the experimentally observed bonding of oxide surfaces [117][133]-[136]. So far, only one case of O-down CO has been reported for the case of exposed cations in zeolite cavities [137].

8.4.1.1 Sampling strategies

The search for the CO equilibrium position with respect to the pentacoordinated Sn for each model was done by either of two means: *via* geometrical optimizations or, "by points". Geometrical optimizations are performed by analytical gradient calculations, while "by points" optimizations are done by calculating energies for a geometrically frozen CO molecule at different distances of the surface, in this way the potential well, or an approximation since the CO is frozen, of CO with respect to the surface is obtained. This is interpolated by a polynomial of order $n-1$ (where n is the number of sampled points) that yields the energy minimum and the vibrational frequency Surface–CO, considering all the atoms in the surface static, i.e. with infinite mass. At this minimum, the CO bond is stretched with the centre of masses fixed, in order to get an approximation of the distortion of the molecule geometry due to the presence of the surface and the adsorbed CO stretching vibrational frequency.

The "by points" optimizations are generally much less computationally intensive than the calculation of analytical first and second derivatives used to calculate the optimized geometries and frequencies. This scenario worsens in cluster DFT calculations, Gaussian98 [26], since the code cannot use integral symmetry in optimizations when PCs are present.

Both methods of optimization and vibrational analysis yield quite similar results since the Sn–CO and C–O stretching modes are quite different in frequency and therefore relatively uncoupled. The "by points" optimization is very feasible in this case due to the reduced number of variables.

The selection of the sampling points, or distances has to be done with care. The potential curves are deformed parabolas and considering points where the potential well is very anharmonic yields frequencies that are not representative of the ground state vibrational mode which mainly samples the harmonic region.

In order to check the consistency of our approach we have for the smaller cluster probed the harmonic and anharmonic regions of a rigid CO molecule relative to the surface and calculated the frequencies with different combination of sampling points. As expected at distances relatively close to the minimum, i.e. the harmonic part, the results were relatively invariant on different combinations and number of points yielding very similar results to the ones obtained by gradients.

In order to reduce to a minimum the sources of numerical noise in the "by points" optimizations we have undertaken the following strategy:

1. The same set of sampling points, always relative to the Sn–O layer of the unrelaxed surface, was systematically used in all subsequent calculations, periodic (relaxed and unrelaxed) and cluster.

2. Although the binding energies are calculated with respect to the optimized gas phase CO with the corresponding Hamiltonian which imply slightly different CO distances, the chosen frozen CO distance for the sampling was set in all cases equal to the experimental value of 2.15 bohr (1 bohr = 0.529167 Å ~ half Angstrom).

8.4.1.2 Results

The three clusters provide basically similar answers although some oscillations with cluster size are found, the distance C–Sn is obtained to be 4.6±0.05 bohr

	$[Sn_3O_8]^{2-}$	Sn_7O_{14}	$Sn_{13}O_{26}$
PCs	+2/-1	+2/-1	+2/-1
z_e(Sn–CO)/bohr	4.603	4.558	4.650
D_e/eV	0.75	0.95	0.73
D_e(BSSE)/eV	0.57	0.82	—
ω_o(Sn–C)/cm^{-1}	187	195	183
r_e(CO)/bohr	2.103	2.097	—
ω_o(C–O)/cm^{-1}	2380	2409	—
$\Delta\omega$/cm^{-1}	+110	+139	—

By points optimization

Table 8.35: Properties of CO adsorbed on cluster models of $SnO_2(110)$ (HF results)

	Sn_7O_{14}		
PCs	+4/-2	+2/-1	+1/-0.5
Opt.	Grad.	Points	Grad.
z_e(Sn–CO)/bohr	4.551	4.558	4.558
D_e/eV	0.93	0.95	0.89
r_e(CO)/bohr	2.097	2.098	2.096

Table 8.36: Dependence of the surface–CO distance, z_e(Sn–C), and adsorption energy, D_e, on the PC embedding (HF results)

and the adsorption potential curve is relatively flat. This is shown by the low value of ω_e(Sn–CO), 188±7 cm^{-1}. The binding energy, defined **positive** when the bound molecule is more stable than the isolated fragments, oscillates from 0.75 eV with the smaller cluster, to 0.95 eV with the medium one, being 0.73 eV with the larger model. These values are not corrected by the BSSE, sect. 2.4.2. This correction has been estimated with the small and medium models, and a similar error, $\sim$ 0.15 eV, has been determined. Thus, the BSSE corrected adsorption energy computed at the HF level with cluster models is between 0.6 and 0.8 eV. It is interesting to note that similar values of the adsorption energy were obtained with the comparable models and wave functions for CO on TiO_2(110) [127].

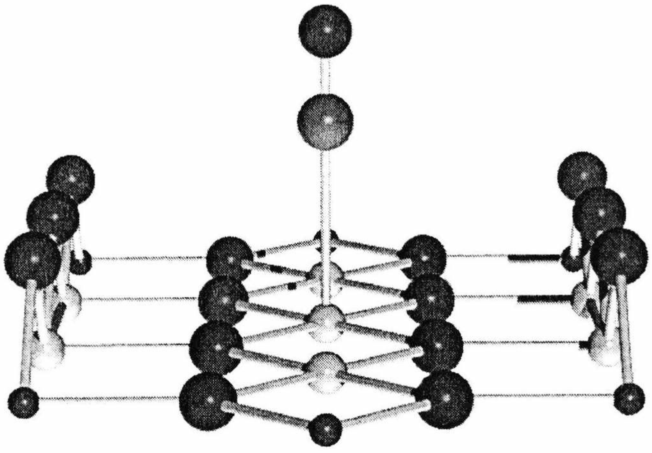

Figure 8.47: CO physisorbed on a Sn_7O_{14}–Sr_6 cluster ,
C and O atoms: bigger light and dark spheres, respectively,
Sn and Sr atoms: smaller light and dark spheres, respectively

The adsorption is accompanied by a considerable shift in the vibrational frequency of adsorbed with respect to free CO. With the small model we compute a $\Delta\omega$ of +110 cm^{-1}, with the medium cluster the shift is even higher, +139 cm^{-1}. Also in this case we notice that similar high shifts were found for CO on TiO_2(110) [127].

The HF calculations have been repeated with periodic models, table 8.37. We have first considered the unrelaxed SnO_2 surface using 2L and 3L slabs. These results are directly comparable with those of the cluster since surface relaxation is not present in the cluster. The CO molecules are adsorbed at 4.66 bohr from the five-coordinated Sn, with an adsorption energy of 0.66 eV. This value is reduced to 0.49 eV after the inclusion of BSSE, from clusters we obtained 0.6-0.8 eV. The reason for this is partly coming from the fact that in this case we are modelling a full monolayer coverage (θ=1) and there is a repulsive interaction CO–CO in contrast with the cluster models were an isolated CO molecule is considered. In fact, a slab calculation with half coverage (θ=0.5) results in an adsorption energy of 0.63 eV (BSSE corrected); the repulsive adsorbate interaction from θ=1 to θ=0.5 is $\sim$ 0.1 eV/molecule. The other properties, in particular the vibrational frequencies are surprisingly close in slab and cluster calculations. The CO ω shift with the 2L slab is +122 cm^{-1}, in between the values computed with the small and medium cluster models. Reducing the coverage from θ=1 to θ=0.5 results in no significant shift of the CO vibration, table 8.37

Sn-O layers	2L	3L	2L	2L	3L	4L
Slab	Unrelaxed	Unr.	Unr.	Relaxed	Rel.	Rel.
CO Coverage, Θ	1	1	0.5	1	1	1
z_e(Sn–C)/bohr	4.660	4.659	4.610	4.927	4.844	4.844
$z_e(Sn_{unr.} - C)^*$/bohr	—	—	—	4.617	4.614	4.613
ω_o(Sn–C)/cm^{-1}	192	193	201	137	151	152
D_e/eV	0.66	0.66	0.81	0.32	0.44	0.43
D_e(BSSE)/eV	0.49	—	0.63	—	0.30	—
ω_o(C–O)/cm^{-1}	2392	—	2394	—	2369	—
r_e(CO)/bohr	2.104	—	2.102	—	2.108	—
$\Delta\omega$/cm^{-1}	+122	—	+124	—	+99	—

(*) Respect the *virtual* unrelaxed Sn-O layer plane

Table 8.37: Properties of CO adsorbed on, relaxed and unrelaxed slab models of SnO_2(110) (HF "by points" calculations)

The HF slab calculations show the same result for unrelaxed 2L and 3L slabs.

8.4.2 Relaxed Surface CO Adsorption

So far we have considered results obtained for the, ideal, unrelaxed (110) face of SnO_2 while it is quite possible that surface relaxation will play a role also on the CO physisorption properties.

The effect of the surface relaxation on the CO adsorption is non-negligible. At the HF level with the 3L, we observe a decrease in the CO adsorption energy from 0.66 eV (unrelaxed) to 0.44 eV (relaxed). Once the BSSE correction is introduced, the value of the adsorption energy is further reduced to 0.30 eV, table 8.37. In the relaxed surface the decrease of the adsorption enery is accompanied by an increase of about 0.2 bohr of the Sn–CO distance. This change in bond distance is largely due to the fact that in the relaxed surface the Sn atoms move down, towards the interior of the material, decreasing the distance to the underlying layer. Remarkably, with respect to a virtual plane defined by the unrelaxed Sn-O layer the CO molecule is practically at the same height, with a small but systematic difference of $\approx$0.04 bohr. This is a very interesting feature, since there is a non negligible difference of displacement of the Sn atom passing from 2L and 3-4L, 0.07 bohr, and regardless the CO appears at the same height. This seems to indicate that the adsorption position does not depend so much on the vertical relaxation of the surface.

The longer distances and the weaker bonds have direct effects on the vibrational frequencies. On the relaxed surface ω_e(Sn–CO) is +151 cm^{-1}, about 40 cm^{-1} less than for the unrelaxed case. Also, the CO vibrational frequency decreases by about 20 cm^{-1} and the shift respect to free CO becomes +99 cm^{-1}, table 8.37. Despite these differences, however the general features of the interaction are maintained, namely, a relatively weak bonding accompanied by a large positive shift in the C–O frequency. We will show that these properties are largely determined by electrostatic effects with some contribution from chemical bonding mechanisms, sect. 8.4.4.

8.4.3 Correlation effects

Most of the calculations described so far have been performed at the HF level. While this approach provides a reasonable description of the interaction of CO with oxide surfaces, correlation effects can play a non-negligible role in the bonding. This is particularly true for transition metal, TM, oxides. For instance, recently it has been shown that the vibration shift of CO adsorbed on the $Cu_2O(111)$ surface has a different sign when computed at HF or DFT levels [132], in particular while HF predicts a positive shift, DFT gives a negative shift, in agreement with experimental observations. In this latter case, the change in sign of the shift is due to the interaction of the filled 3d states on Cu with the empty levels of CO, a mechanism which is quite sensitive to the inclusion of correlation effects [132]. In SnO_2 the Sn 4d levels are too deep to be involved in the bonding with CO, and are not explicitly considered, but nevertheless it is possible that the correlation may affect some of the bonding mechanisms. For this reason we have computed correlation effects in various ways. In the cluster models, these have been introduce through second-order Møller-Plesset perturbation theory, MP2. The results have been performed with two clusters, $[Sn_3O_8]^{2-}$, and Sn_7O_{14}; in both cases the clusters are embedded in ECPs and (+2/-1) PCs. In principle, a CO basis set with d polarization functions is needed for MP2 calculations; in order to make a direct comparison with the other correlated calculations we used the DZ basis set described in sect 7.1.1. We have also used the Sn_7O_{14} cluster with the DFT-B3LYP approach, table 9.42. For the slab calculations correlation effects have been introduced by performing B3LYP calculations with the 2L slab model, both relaxed and unrelaxed, but also with the pure BLYP exchange-correlation functional, table 9.42. Although the results of these calculations are not identical, not surprisingly given the different models and methods adopted to include correlation, the trends are the same and some general conclusions can be drawn.

First of all, the adsorption energy computed at the DFT level is similar to that found in HF, for the slab calculations the difference is negligible. On the relaxed slab, the BSSE corrected DFT adsorption energy, 0.25 eV, table 9.42, is nearly the same as found at the HF level, 0.30 eV table 8.37. Larger oscillations have been found in MP2, but the B3LYP results are extremely stable and essentially the same values are obtained with a Sn_7O_{14} cluster and with a 2L slab. This is true also for the geometrical parameters like the height of the molecule from the surface and for the CO vibration: the shift in CO ω_e is $\approx$+120 cm^{-1}, in line with the HF results. At the MP2 level the CO ω_e shift, +56 cm^{-1} and +90 cm^{-1} with $[Sn_3O_8]^{2-}$, and Sn_7O_{14} respectively, is smaller than at the HF level. In any case, a large positive shift is predicted for the unrelaxed surface.

The results on table 9.42 show that the inclusion of correlation does not change significantly the HF results. This provides an indirect but strong indication that the bonding is not dominated by covalent interactions, but rather by electrostatic mechanisms. These latter are usually described with sufficient accuracy already at the HF level.

	$[Sn_3O_8]^{2-}$ +2/-1	Sn_7O_{14} +2/-1	Sn_7O_{14} +2/-1	SnO_2(2L) Unrelaxed	SnO_2(2L) Relaxed	SnO_2(2L) Unrelaxed
Method	MP2	MP2	B3LYP	B3LYP	B3LYP	BLYP
z_e(Sn-C)/bohr	4.673	4.519	4.584	4.640	4.847	4.631
D_e/eV	0.64	1.131	0.76	0.65	0.45	0.57
D_e(BSSE)/eV	0.33	—	0.57	0.46	0.24	—
ω_e(Sn-C)/cm^{-1}	160 ± 10	210	180	178	136	169
r_e(CO)/bohr	2.187	2.191	2.148	2.156	2.158	—
ω_e(C-O)/cm^{-1}	1959	1993	2170	2142	2131	—
$\Delta\omega/cm^{-1}$	56	90	120	92	81	—

Table 8.38: Effect of electron correlation on adsorption properties of CO/SnO_2(110)

8.4.4 Bonding analysis

One important question in the description of the bonding of small molecules like CO with the acid sites of oxide surfaces is the extent of electrostatic and chemical bonding contributions to the adsorption energy but also to other measurable properties, in particular the vibrational frequencies and the frequency shifts with respect to the gas phase.

A very useful technique to answer these question is the Constrained Space Orbital Variation (CSOV) [138, 139]. This procedure allows one to decompose the interaction energy, but also other properties, into the sum of various contributions: Pauli or exchange repulsion, intra-unit polarization, charge-transfer or covalent bonding, etc. This technique has been used in several studies of adsorbates on surfaces based on HF wavefunctions, and recently extended also to DFT calculations [140, 141]. More details about the computational procedure can be found in refs. [138, 139].

Here we describe the results of a CSOV analysis obtained with the $[Sn_3O_8]^{2-}$, and Sn_7O_{14} clusters from HF calculations, table 8.39. The first step of the CSOV consists in the superposition of the wavefunctions of the separated fragments A and B, i.e. cluster and CO, at a distance close to equilibrium, 4.6 bohr. A zero-order wavefunction for the system AB is constructed by Schmidt orthogonalization of the occupied orbitals on fragment A to the occupied orbitals of fragment B, or *vice versa*.

No mixing between the two sets of orbitals is allowed and the step is called frozen orbital (see FO in table 8.39). The interaction energy, E_{int}, at this step arises from two mechanisms, the electrostatic attraction between the cluster and the CO charge distributions and the Pauli repulsion due to the non-bonding overlap of the occupied orbitals. In our case, the combination of these two contributions leads to a weakly repulsive interaction (by 0.3-0.4 eV). Very pronounced is the effect of the FO interaction on the CO vibrational frequency which exhibits a blue shift of 180-220 cm^{-1} depending on the cluster. This large blue shift can be mainly understood from the Pauli repulsion of the CO lone pair and the "rigid wall" formed by the SnO_2 orbitals, sometimes referred to as the "wall effect" discussed in refs. [127, 130]. The electrostatic contribution arising from the CO multipoles and the electric field of the $SnO_2(110)$ surface can been approximated by placing the CO molecule at the same distance above an array of

(+2/-1) point charges placed at the $SnO_2(110)$ lattice positions. The electrostatic interaction between the surface electric field and the CO charge distribution leads to a $\Delta\omega_e$(C–O) of +92 cm^{-1}. The rest of the shift is therefore arising from the Pauli repulsion, as already found for other oxide surfaces [127, 129, 132].

In the CSOV step 2 the occupied and unoccupied orbitals of the SnO_2 cluster are allowed to mix. This represents the polarization of the SnO_2 surface in response to the presence of the CO molecule. From table 8.39 it can be seen that the polarization of the oxide has only a minor effect on the interaction energy and on the CO vibrational frequency. In the third CSOV step the occupied SnO_2 cluster orbitals can mix with the virtual orbitals of the CO molecule. This accounts for the π back donation from the surface orbitals, mainly of the central Sn atom, into the unoccupied CO $2\pi^*$ orbitals. This effect is quite important when the d shell in TM oxides is partially filled, as for instance in TiO_2 [127] and Cu_2O [142]. Here, the effect of charge transfer from the SnO_2 substrate to CO is not large; ΔE_{int} at this step is 0.14–0.18 eV and is partially due to BSSE effects. Also the change of ω(C–O) due to the back donation is very small, 5–8 cm^{-1}. The fact that the charge transfer from the oxide to CO is negligible can also be measured by the change in the dipole moment ν. Since the nuclei are fixed during all the CSOV steps, a change in ν, $\Delta\nu$, reflects the polarization of the electric density towards or away from the surface (in particular a positive indicates charge flow from CO to the surface and vice versa). At the $SnO_2 \rightarrow$CO charge transfer step $\Delta\nu$ is nearly zero, showing that the stabilization measured by ΔE_{int} is indeed an overestimation due to the BSSE.

In the fourth CSOV step mixing between the occupied and unoccupied orbitals of CO is allowed. This step corresponds to the polarization of the CO molecule in the presence of the surface and leads to a substantial stabilization of the surface complex, from 0.3 to 0.45 eV depending on the cluster. This is a real net contribution since there is no BSSE at this step. The substantial polarization of CO is shown also by $\Delta\nu$ which is +0.4/+0.5 a.u., indicating a polarization of the CO electrons towards the surface, as one should expect given the attractive potential of the underlying cation. This mechanism does not alter significantly the CO frequency which is lowered by less than 30 cm^{-1} with a total net shift of ω(C–O) with respect to the free molecule of +140/+180 cm^{-1}, table 8.39. In the next CSOV step the occupied CO orbitals are mixed with the empty states of SnO_2. This step describes the CO→SnO_2 donation, mainly occurring from the CO σ orbital.

This mechanism is very dependent on the geometrical structure of the surface and on the nature of the cation in the oxide. It is negligible on MgO and NiO [129, 130], and becomes significant on TiO_2 [127] and Cu_2O [131, 132]. In SnO_2 the CO σ donation is the most important bonding contribution as it accounts for 0.5-0.6 eV of bonding in the two models considered, table 8.39. Being of inter-unit nature, this step suffers from the occurrence of the BSSE but even considering this aspect, it is clear that the CO donation is an important term. The flow of charge from CO to the surface is clearly shown by the sign and the value of $\Delta\nu$. As found for other oxides [127, 129, 132], the effect of the CO σ donation on ω(C-O) is a moderate negative shift of -26 cm^{-1} with the small model and -38 cm^{-1} with the large one.

After inclusion of the most important bonding mechanisms the frequency shift of the adsorbed CO molecule is still very high, table 8.39. The last CSOV step corresponds to a full self-consistent calculation. The difference to the previous step is a measure of the completeness of the analysis. Neither the energy nor the frequency or the dipole moment of the surface complex show relevant changes at the last step, indicating the absence of important coupling terms between the individual bonding mechanisms. To summarize, the bonding and vibrational frequency shift of CO adsorbed on SnO_2 are due to three dominating effects: the wall effect or Pauli repulsion leading to an upward shift of CO ω_e, the CO polarization, mainly contributing to the complex stability, and the CO σ donation which is the most important bonding term. We notice the unimportance of the Sn→CO back donation which is consistent with the absence of filled d levels in the valence of the cations. It is interesting to make a direct comparison between the CSOV results for $SnO_2(110)$ and those obtained with a cluster of the same size and using a very similar basis set for CO adsorbed on $TiO_2(110)$ [127]. The main difference is that on TiO_2 there is evidence of a charge transfer from the oxide to CO. This is shown in particular by the sign of $\Delta\nu$ which is negative, i.e. consistent with an electron flow from Ti to CO. The other contributions, CO polarization and CO donation, are similar. Similar is also the conclusion that the large shift computed on both TiO_2 and SnO_2 at the HF level, $+147$ cm^{-1} and $+139$ cm^{-1}, respectively, arise from the FO interaction which is purely electrostatic. The CSOV analysis has been performed at the HF level and one should mention that some mechanisms are more sensitive than others to the inclusion of correlation effects. One of these terms is the π back donation from filled d states of the cation to the empty $2\pi^*$ levels of CO. In fact, while the wall effect and other contributions to the overall $\Delta\omega$(C–O) are described in the same manner in HF and DFT methods, there is a substantial increase in the back donation when electron correlation is considered [132]. Where present, the back donation partially reduces the large blue shift due to the wall effect. On SnO_2, however, this mechanism seems to be less important than in Cu_2O and TiO_2 which also explains the similarity of the results obtained at the HF and DFT levels, table 9.42.

8.4.5 Electrostatic potential

The results described in previous sections show unambiguously that cluster and slab models give a similar description of the interaction between CO and the SnO_2 surface. The analysis of the bonding mechanisms and of the origin of the CO vibrational shift suggests that this can be attributed to the fact that the bonding has a large electrostatic component and that this component is well described even with a cluster of finite size. The largest changes in the bonding are found when the surface relaxation is introduced in the calculations.

These conclusions prompted us to analyze in more detail the electrostatic potential (EP) generated by the cluster and the slab models. To this end we have generated the EP in a region outside the surface and extending from the plane

			$[Sn_3O_8]^{2-}$				
CSOV step	E_{int}/eV	ΔE_{int}	ν/au	$\Delta\nu$	ω/cm^{-1}	$\Delta\omega$	r_e(CO)/bohr
FO	-0.30	—	-0.82	—	2451	+181	2.089
Pol. SnO_2	-0.25	+0.05	-0.79	+0.03	2447	-4	2.090
$SnO_2 \rightarrow CO$ c.t.	-0.07	+0.18	-0.82	-0.03	2439	-8	2.091
Pol. CO	+0.23	+0.30	-0.40	+0.42	2411	-28	2.095
$CO \rightarrow SnO_2$ c.t.	+0.71	+0.48	-0.18	+0.22	2385	-26	2.101
full SCF	+0.74	+0.03	-0.07	+0.11	2380	-5	2.103

			Sn_7O_{14}				
CSOV step	E_{int}/eV	ΔE_{int}	ν/au	$\Delta\nu$	ω/cm^{-1}	$\Delta\omega$	r_e(CO)/bohr
FO	-0.44	—	-16.75	—	2488	+218	2.092
Pol. SnO_2	-0.38	+0.06	-16.81	-0.06	2483	-5	2.083
$SnO_2 \rightarrow CO$ c.t.	-0.24	+0.14	-16.84	-0.03	2478	-5	2.084
Pol. CO	+0.22	+0.46	-16.31	+0.53	2451	-27	2.089
$CO \rightarrow SnO_2$ c.t.	+0.84	+0.62	-16.04	+0.27	2413	-38	2.096
full SCF	+0.90	+0.06	-16.04	+0.00	2409	-4	2.097

Table 8.39: CSOV analysis results

containing the five-coordinated Sn and the basal O atoms up to 20 bohr from the surface for the unrelaxed 2L slab and the Sn_7O_{14}(+2/-1) cluster, figure 8.48.

The qualitative features are similar, but significant differences can be seen. In order to have a clearer picture, a section of the EP function has been extracted, that gives us the EP on the Sn atom on the (110) adsorption vector, fig. 8.49.

In particular, a wide region starting at about 8 bohr above the surface is practically zero in the periodic case while it begins being slightly negative in the cluster plus PCs. This is probably due to the presence of the protruding oxygens which, outside the cluster region are represented by negative PCs, fig. 8.49.

In fact, the use of (+4/-2) PCs results in even larger deviations from the periodic results; in a symmetric way, (+1/-0.5) PCs shows a better behavior at long distance from the surface. This suggests that cluster models of SnO_2 embedded in PCs cannot be used for the description of the long range interactions.

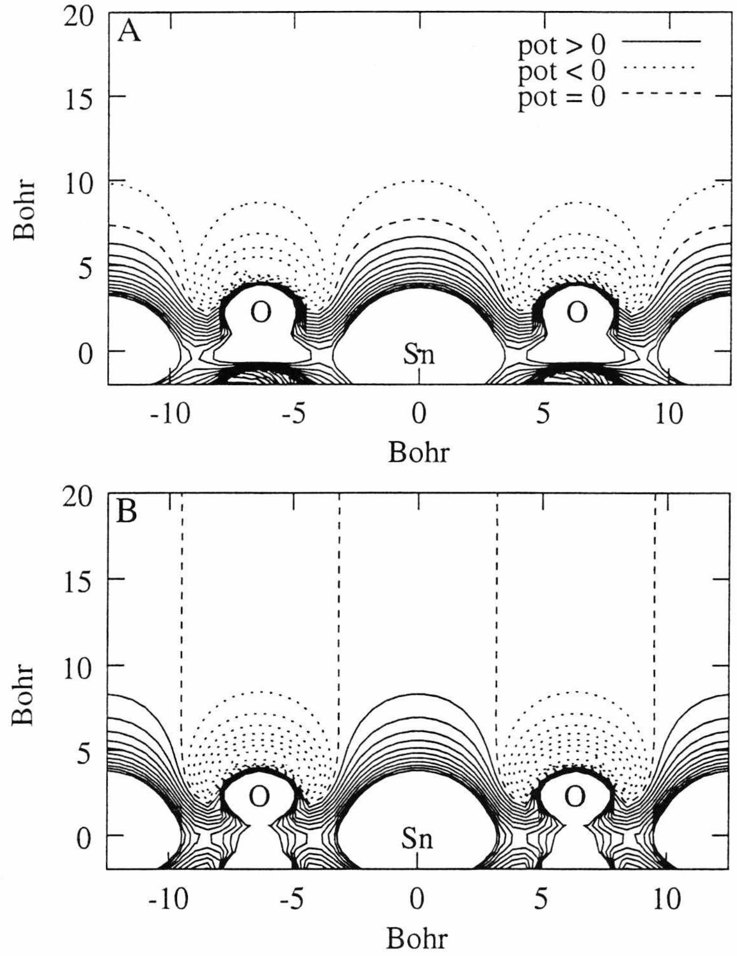

Figure 8.48: Electrostatic potential in the adsorption region. (a) Sn_7O_{14}(+2/-1); (b) SnO_2 2L slab. The contour lines are drawn in intervals of 0.5 eV

8.4.5.1 Electrostatic potential on the adsorption region

One open question is why the results are so similar when obtained with clusters and slabs despite the differences in EP. In the adsorption region near the Sn cation the EP becomes very attractive and the slope of the curve is similar (although not identical) for slab and cluster models. This is clearly shown in fig 8.51 where a more detailed section of the EP is reported. 2L and 3L slab models of the unrelaxed surface give practically the same EP, thus further confirming the stability of the results versus slab thickness. The Sn_7O_{14}(+2/-1) cluster gives a slightly lower value of the EP in this region. The fact that the final adsorption energy

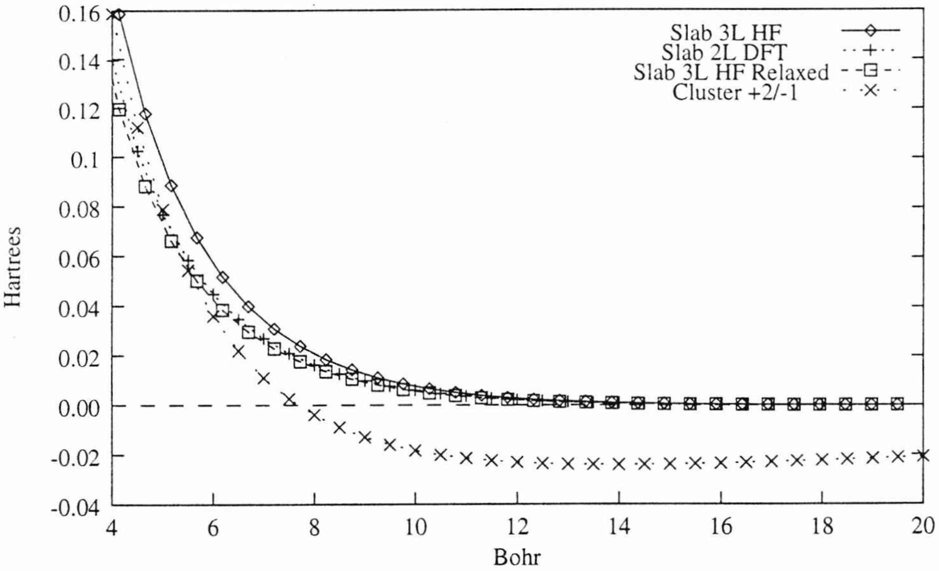

Figure 8.49: Section of the electrostatic potential in a plane normal to the five-coordinated Sn atom where CO is adsorbed. The four curves refer to an unrelaxed 3L slab (HF results), a relaxed 3L slab (HF results), an unrelaxed 2L slab (DFT results) and a $Sn_7O_{14}(+2/-1)$ cluster (HF results)

and CO vibrational frequency are nearly the same in slab and cluster models is probably due to a compensation of effects (e.g. an increased Pauli repulsion). Two significant differences in the EP are found when we compare HF and DFT results and relaxed with unrelaxed surfaces. The DFT EP is always lower than the HF one; this is consistent with the general tendency of DFT to reduce the charge separation in oxides compared to HF [143]. The lowest value of the EP in the adsorption region is given by the relaxed surface. In this case, the ion displacement at the surface has the effect of reducing the surface energy and at the same time to decrease the EP, thus resulting in a lower binding energy, a lower Pauli repulsion, bigger distance Sn–CO, and a smaller CO vibrational shift.

From figure 8.51 it would seems there is a sort of qualitative correlation between the value of the electric field on the chemisorption region and the binding energy, this is denied by different PCs cluster calculations where the EP is different but not, notably, the binding energy.

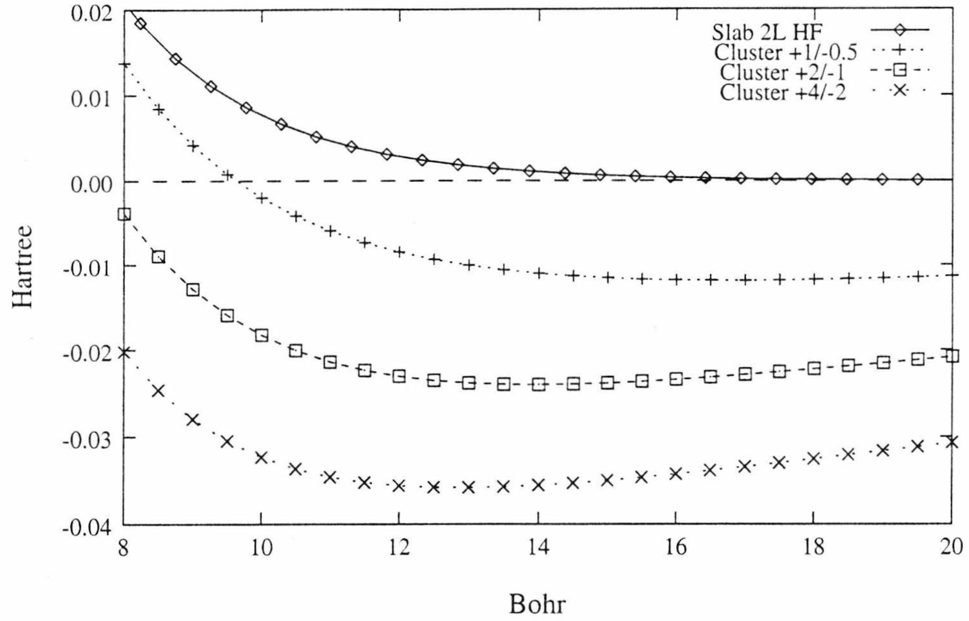

Figure 8.50: Section of the electrostatic potential in a plane normal to the five-coordinate Sn atom where CO is adsorbed. The four curves refer to HF results on, an unrelaxed 3L slab, a Sn_7O_{14}(+4/-2), Sn_7O_{14}(+2/-1), Sn_7O_{14}(+1/-0.5) clusters

8.5 Conclusions

Hartree-Fock and Density Functional Theory calculations of adsorption of CO molecules on pentacoordinated Sn ions of different clusters and slabs representing the SnO_2 (110) yielded very similar results. DFT binding energies are systematically lower than HF. The binding energy has been shown not to depend strongly on the values of the clusters PCs. The repulsion between adsorbed CO molecules is not very strong at the maximum coverage. The bonding and vibrations of adsorbed CO have been analyzed by decomposing the interaction energy into the sum of various contributions. This analysis shows that the interaction of CO with the five-coordinated Sn ions of the surface has a large electrostatic character reinforced by a substantial donation of charge from CO to the cation. The CO adsorption is rather weak but is accompanied by a large shift of the vibrational frequency towards higher values.

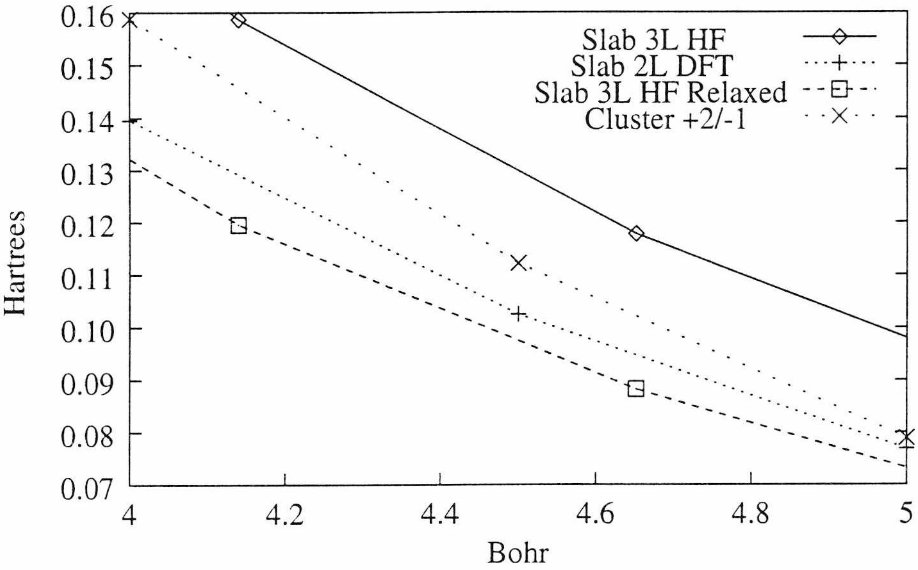

Figure 8.51: Section of the electrostatic potential in a plane normal to the five-coordinated Sn atom where CO is adsorbed. The four curves refer to an unrelaxed 3L slab (HF results), a relaxed 3L slab (HF results), an unrelaxed 2L slab (DFT results) and a Sn_7O_{14}(+2/-1) cluster (HF results)

Chapter 9

Adsorption of CO_2 on $SnO_2(110)$

9.1 Introduction

The interaction of carbon dioxide with oxide surfaces is involved in a number of relevant processes in heterogeneous catalysis [144]. The acidic or basic nature of a metal oxide largely determines its catalytic activity towards an adsorbed species, and, the characterization of acid-basic properties of a metal oxide is of considerable practical importance. The basic strength of a solid surface is usually defined as the ability of the surface to convert an adsorbed electrically neutral acid, from solution or from gas phase to its conjugate base. For instance, the amount of CO_2 irreversibly adsorbed on the surface of a thermally pretreated and dehydroxylated CaO surface may provide a measure of the density of basic sites, considered to be the O^{2-} sites on the surface [145]. An important aspect of the basicity of an oxide is also connected to the nature of the density of the surface defects. It is well known that surface defects, are the sites where most chemistry takes place [146].

Experimentally, different kinds of adsorbed CO_2 species have been observed on the surface of oxides. CO_2 can be physisorbed, where it remains fairly unaltered, or chemisorbed creating a surface carbonate according with the following chemical reaction:

$$CO_2 + O^{2-}_{surf} \rightarrow CO_3^{2-} \tag{9.58}$$

Carbonates formation after the introduction of oxide samples in CO_2 atmospheres has been observed on a number of oxides, see [117] and therein, and specifically on SnO_2 [147] where IR adsorption on polycrystalline samples has been extensively studied. Unfortunately, polycrystalline samples studies although fairly representative of industrial catalysts present intrinsic difficulties of interpretation of data. The surfaces may be very defective and certainly heterogeneous so that unambiguous assignments cannot be obtained due to the lack of characterization and control of the substrate surfaces.

The main objective of this work is to characterize some of the possible adsorption modes of CO_2 in different sites (basic and acid) of the perfect SnO_2(110). The methods used are similar to the ones used in similar studies making possible a direct comparison with other model oxides [148, 149].

9.2 CO_2 basis set

The IR absorption, i.e. vibrational, frequencies may be calculated under the cluster approach and compared with experimental results. To validate the choice of basis sets we have initially calculated the optimized free molecule vibrational frequencies.

The equilibrium geometries and vibrational frequencies of both species have been calculated with three theoretical methods, HF, MP2 and DFT-B3LYP. The same basis set used for CO [9s5p/4s3p] with and without polarization functions on both C and O, α_d(C)=0.657, α_d(O)=0.74, i.e. a [9s5p/4s3p] DZ basis and a [9s5p1d/4s3p1d] DZP basis, have been used.

These calculations yielded quite bad results with the DZ basis on all correlated techniques, while HF showed the closest geometry and frequencies to experiment. At the same time, with the inclusion of polarization functions, MP2 and DFT-B3LYP results were much closer to experiment, see table 9.40, as expected.

The same calculations were performed with 6-31G and 6-31G* basis sets, in order to see if the trend of the results was something specific to our basis set or something more general. Overall very similar results were obtained, table 9.40. In both cases, when electronic correlation is considered, the frequencies differ only by 1–2%.

Normal Modes Hamiltonian	Basis	ν_1 /cm^{-1}	ν_2 /cm^{-1}	ν_3 /cm^{-1}	r_e(CO) /bohr
HF	DZ	1380	617	2302	2.19
HF	DZP	1510	778	2565	2.16
MP2	DZ	1193	512	2210	2.28
MP2	DZP	1316	664	2408	2.23
B3LYP	DZ	1256	564	2213	2.24
B3LYP	DZP	1368	678	2415	2.20
exp		**1340**	**667**	**2349**	**2.19**
HF	6-31G	1407	657	2374	2.19
HF	6-31G*	1517	749	2582	2.15
MP2	6-31G	1226	521	2292	2.28
MP2	6-31G*	1337	641	2455	2.22
B3LYP	6-31G	1282	563	2283	2.25
B3LYP	6-31G*	1367	645	2430	2.20
exp		**1340**	**667**	**2349**	**2.19**

Table 9.40: CO_2 vibrational frequencies and distances calculated at the HF, MP2, and B3LYP levels with different basis sets

The selection of the DZP basis set is based on this results, as well as the possibility of a direct comparison with previous similar calculations [148, 149].

9.2.1 CO_3^{2-} frequencies

CO_2 reacts with surface oxygen ions to form carbonates, we have calculated the vibrational frequencies on the DZP set optimized trigonal D_{3h} free CO_3^{2-} carbonate ion, table 9.41. The experimental frequencies and the notation used can be found in [150].

For the carbonate, HF overestimates the frequencies as much as 153 cm^{-1}. The results for B3LYP are very good in comparison, most frequencies are only

Normal Modes Hamiltonian	ν_1 /cm^{-1}	ν_2 /cm^{-1}	ν_{3a} /cm^{-1}	ν_{3b} /cm^{-1}	ν_{4a} /cm^{-1}	ν_{4b} /cm^{-1}
HF	1126	1004	1568	1568	732	732
B3LYP	1009	884	1407	1408	663	663
exp	**1063**	**879**	**1415**	**1415**	**680**	**680**
			Differences Exp.-Calc.			
HF	-63	-125	-153	-153	-52	-52
B3LYP	54	-5	8	7	17	17

Table 9.41: CO_2 vibrational frequencies, HF, and DFT-B3LYP results versus experiment

slightly underestimated (1–2%) but the first one, +54 cm^{-1} (5%). The distances obtained were fairly similar, HF, 1.286 Å, and B3LYP 1.312 Å. These results further confirms the use of a DZP basis set for this study.

9.3 Cluster embedding

The cluster embedding in this case is slightly different from the CO case. It has been shown, that the 2L truncated-bulk slab is as good a representation of the unrelaxed surface as any thicker slab, consequently some calculations have been performed on clusters embedded on 2L charges slabs, fig. 9.52.

We have used four qualitatively different clusters for this adsorption study:

- Sn_6O_{12}, O_{2c} centred, embedded on a 2L slab of PCs.
- Sn_6O_{12} (II), centred in between two Sn_{5c}, embedded on a 2L slab of PCs.
- Sn_7O_{14}, Sn_{5c} centred, embedded on a 4L slab of PCs.
- $Sn_{13}O_{26}$, Sn_{5c} and O_{2c} centred, embedded on a 2L slab of PCs.

The $Sn_{13}O_{26}$ cluster, fig. 9.52, is what we call a slab cluster. It has two surfaces and two adsorbing sites, Sn_{5c} and O_{2c}, are centred on the same cluster, and only the sides are embedded on PCs. This allows us to directly compare results from

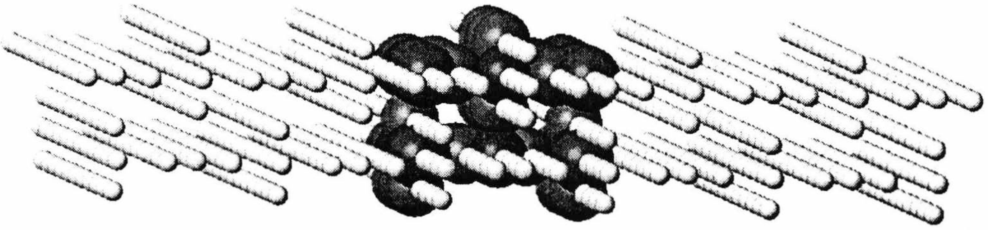

Figure 9.52: $Sn_{13}O_{26}$–Sr_{12} cluster embedded in PCs, the QM treated part is shown with bigger spheres

two different sites, the main basic and the acid sites, with the same cluster. This avoids uncertainties on the binding energy coming from cluster size effects.

9.4 Physisorption versus chemisorption

Physisorption can be defined as all the adsorptions of molecules on any substrate at longer distances than typical chemical bonds. Although, strictly speaking, this is not physisorption, since in most cases there are non-negligible chemical bonding contributions to the binding, this allows us to clearly define very different bonding scenarios in the description of different systems.

In this study, we will consider the energetics and properties of different modes of adsorption of CO_2 on the under-coordinated, usually more reactive, acid (physisorption) and basic (chemisorption), surface sites, Sn_{5c} and O_{2c} respectively.

9.5 CO_2 on Sn_{5c} acid sites

9.5.1 Cluster results

We have studied the adsorption of CO_2 molecules with its axis perpendicular to the surface on Sn pentacoordinated acid sites, fig. 9.53. Two different clusters and different coverage levels on unrelaxed slabs as well as the effect of surface relaxation have been explicitly considered.

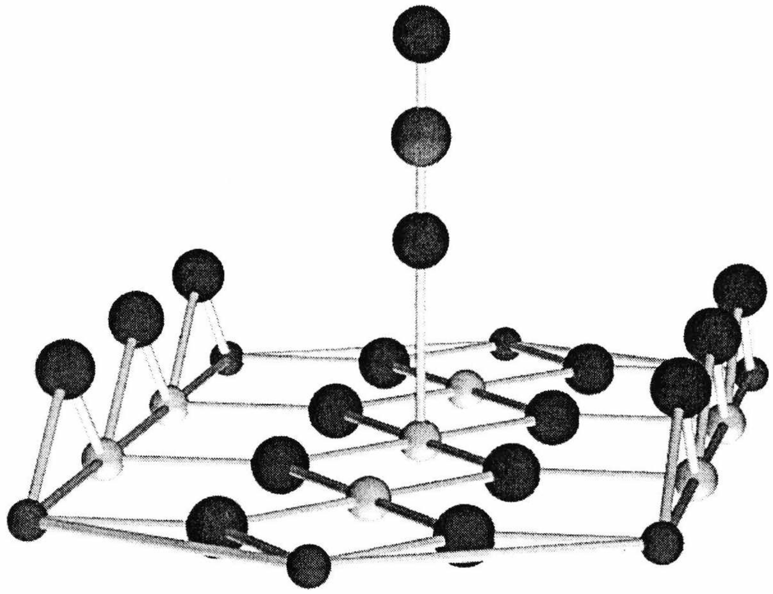

Figure 9.53: CO_2 physisorbed on a Sn_7O_{14}–Sr_6 cluster ,
C and O atoms: bigger light and dark spheres, respectively,
Sn and Sr atoms: smaller light and dark spheres, respectively

Initial studies were performed with the smaller cluster, Sn_7O_{14} at the HF level, where full optimization yielded a Sn–OCO distance of 4.11 bohr and a binding energy of 1.04 eV. Further studies at a higher level of theory, MP2 and B3LYP, yielded systematically higher distances and $\sim$ 50% lower binding energies.

In our previous study of CO, on the contrary, HF, although slightly overestimating the energies, produced very similar geometries to the correlated methods. The difference comes from the fact that CO is a dipolar molecule, and the highest contribution to the interaction comes from an electrostatic term. Conversely, free CO_2 does not have a permanent dipole and due to this, the bonding mechanism can in principle be described by intra-unit polarization and/or charge transfer terms. In order to see how important is the CT we have performed a qualitative, HF level, CSOV analysis. The results show that, as expected, the CO_2 polarization is the dominant mechanism, 0.5 eV, and that the CT from CO_2 to SnO_2 is small, 0.2 eV (and overestimated because of the BSSE).

Only in one case, Sn_7O_{14} cluster, full geometry optimization has been performed. In all other cases only the rigid molecule OCO-Surface distance has been optimized. In comparison, full optimization, and constraint optimization on Sn_7O_{14} give essentially the same result. In the full optimization, the molecule gets only slightly distorted with respect to free CO_2 (the bond closer to the surface gets elongated by 0.02 bohr while the other bond shortens by 0.03 bohr). The adsorption energy, OCO-surface vibrational frequencies[1] and the distance to the surface differ only by 0.02 eV, 4 cm^{-1}, and 0.03 bohr, respectively.

By increasing the cluster size to $Sn_{13}O_{26}$ one finds only a small change in the surface-CO_2 distance, 0.06 bohr.The frequency and binding energy are practically identical.

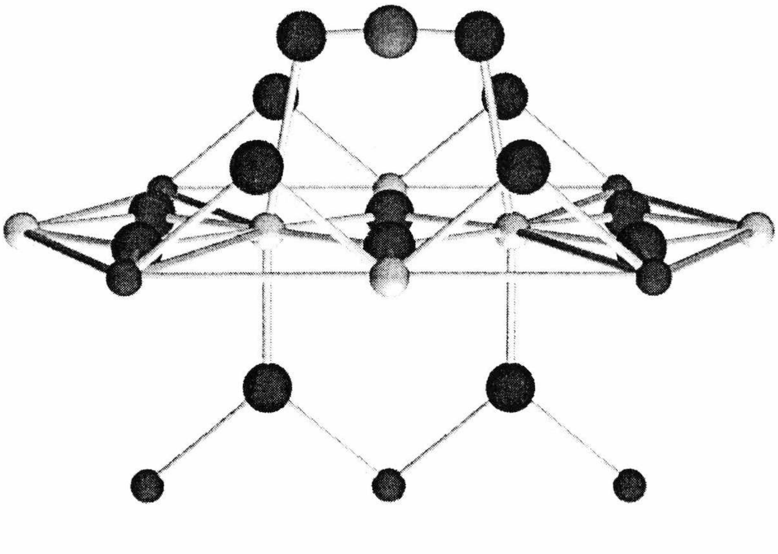

Figure 9.54: CO_2 physisorbed parallel to the surface on a Sn_6O_{12}–Sr_7 (II) cluster, C and O atoms: bigger light and dark spheres, respectively,
Sn and Sr atoms: smaller light and dark spheres, respectively

Geometry optimization at the B3LYP level on the Sn_6O_{12} (II) cluster for a CO_2 molecule parallel to the surface as seen in fig. 9.54 was performed. The CO_2

---

[1] The comparison is not strictly direct since, the frequency calculation is analytical and the surface vibrations may be partially coupled with the normal mode.

molecule bounds to the surface with a binding energy of 0.35 eV (no BSSE) and is slightly bent towards the surface, α(OCO)=174°, the distance O–C gets as well slightly reduced (by 0.04 bohr). CO_2 binds by 0.2 eV more in the perpendicular to the surface case which, consequently, should be the favored one. This contrasts with findings in MgO [148] which established the parallel adsorption mode as more favored than the perpendicular one.

The CO_2 was not found to bind with parallel orientations with the C atom directly on the Sn_{5c} cation at the HF level.

9.5.2 Periodic slab calculations

Surface	$Sn_7O^*_{14}$ Unr.	$Sn_{13}O_{26}$ Unr.	2L Unr.	2L Unr.	2L Rel.	3L Rel.
CO_2 Coverage, Θ			1	0.5	1	1
z_e(Sn-OCO)/bohr	4.352	4.410	4.608	4.457	4.909	4.809
$z_e(Sn_u - OCO)^\dagger$/bohr	—	—	—	—	4.665	4.649
D_e/eV	0.59	0.54	0.32	0.50	0.19	0.23
D_e(BSSE)/eV	0.36	—	0.21	—	—	—
ω_e(Sn-OCO)/cm^{-1}	143	142	119	136	87	96

(*) Gradients optimization

(†) Respect the *virtual* unrelaxed Sn-O layer

Table 9.42: Properties of CO2 adsorbed on Sn_{5c} (B3LYP results)

The comparison of cluster and slab results, table 9.42 shows non-negligible differences; specifically the unrelaxed slab shows a binding energy smaller by 50% and a distance longer by 0.2 bohr than the cluster. However this apparent discrepancy almost disappears, by decreasing the coverage. In fact, going to larger cells, corresponding to a coverage of 0.5 monolayers, the binding energy increases to 0.5 eV and the distance decreases to 4.46 bohr (very close to the cluster result). This shows the crucial importance of the lateral interaction in the adsorption properties of CO_2 (in comparison, in the CO case, only the binding energy changed).

Calculations of frequency and binding energy increasing the range of distances of sampling have been performed in one of the cases[2]. These calculations yielded virtually the same results[3] showing that the observed results are not an artifact of the sampling strategy.

Besides coverage, other important effect is that of surface relaxation. A similar effect of that found on the CO case is found here, the distance Sn-OCO increases mostly due to the fact that the Sn atoms move inwards in the relaxation, the position respect to a virtual unrelaxed layer Sn-O is relatively constant and slightly higher than in the unrelaxed case around 0.04 bohr (similar value but opposite sign than what found with CO at the HF level). Regardless of very different relaxations of the Sn adsorbing atoms in the 2L and the 3L (0.1 bohr) the position of the CO is relatively constant. The binding energy decreases[4] on slab relaxation, by $\sim$ 0.1 eV and the frequencies by 30-40 cm^{-1}.

9.6 CO_2 on O_{2c} sites

CO_2 has been theoretically shown to bind exothermally to the surface oxygens of CaO to form a carbonate [148]. This is known, experimentally to happen as well in many other systems [117] included polycrystalline SnO_2 [147]. For the $SnO_2(110)$ we have studied the adsorption of CO_2 on top of bridging oxygens (O_{2c}) within the cluster and periodic approaches.

The free carbonate ion is a planar molecule with C–O bonds at 120° and all O atoms equivalent by symmetry. Surface carbonates can be seen as deformed CO_3^{2-} ions. The symmetry of the deformation depends on the symmetry of the adsorbing atom in the plane defined by the bridging O and the CO_2 molecule. Due to the symmetry of the bridging O, there are two different possible limit orientations in which the CO_2 molecule may approach the surface; parallel, fig. 9.55, or perpendicular, fig. 9.56, to the rows of bridging oxygens.

---

[2] Relaxed 3L monocell, i.e. the one showing the higher distance surface–OCO.

[3] The energy is virtually the same, and the frequencies and distances differ only by 4 cm^{-1} and 0.01 bohr.

[4] Qualitatively similar as well to the our findings on CO at the HF level.

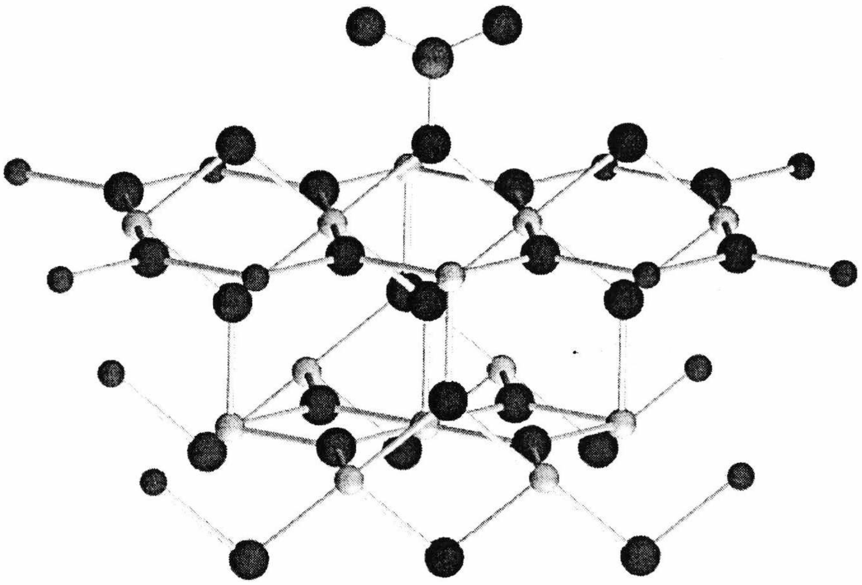

Figure 9.55: CO_2 carbonate, parallel orientation on a $Sn_{13}O_{26}$–Sr_{12} cluster,
C and O atoms: bigger light and dark spheres, respectively,
Sn and Sr atoms: smaller light and dark spheres, respectively

In this case, in comparison with the CO and CO_2 physisorption studies the basis set used for SnO_2 was slightly different. The polarization d function on Sn atoms was not included, while other polarization function, with the same value as the one used on the CO_2 O atoms, $\alpha_d(O)=0.74$ was introduced on all slab O and on the cluster adsorbing O_{2c} atom.

9.6.1 Cluster results

9.6.1.1 HF results

Two clusters, $Sn_{13}O_{26}$ and Sn_6O_{12} have been used for this study. As a first step, we sampled different distances with a linear, geometrically frozen, CO_2 molecule parallel to the surface on the two possible orientations obtaining a weak binding,

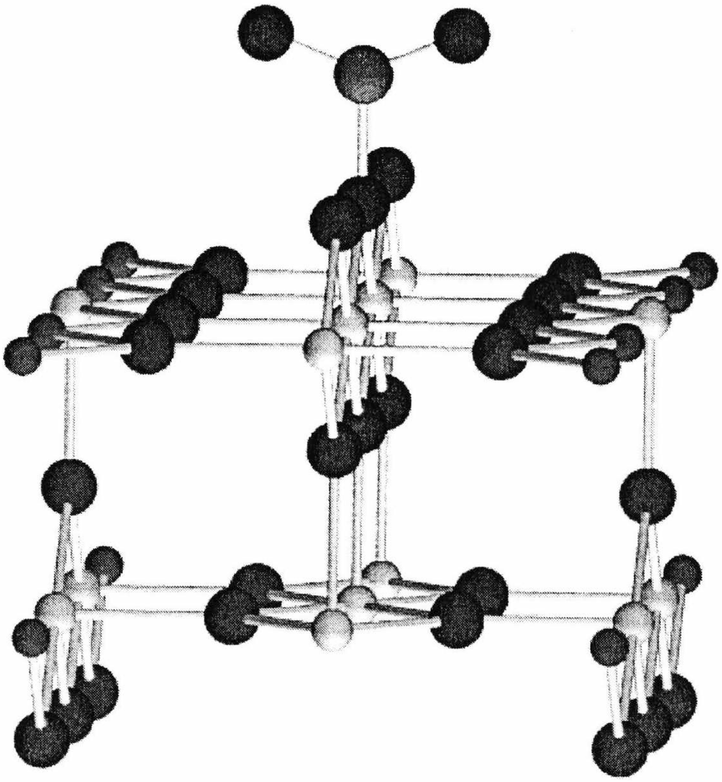

Figure 9.56: CO_2 carbonate, perpendicular orientation on a $Sn_{13}O_{26}$–Sr_{12} cluster,
C and O atoms: bigger light and dark spheres, respectively,
Sn and Sr atoms: smaller light and dark spheres, respectively

0.35 eV, at typical physisorption distances, ~ 5 bohr, for the perpendicular orientation and no binding at all for the parallel one. Full CO_2 optimizations, starting with a linear CO_2 yielded similar results.

In order to form a carbonate from this calculations, the CO_2 molecule must be geometrically activated, i.e. bent, indicating the presence of an activation barrier for the carbonation formation process. Geometry optimizations on the Sn_6O_{12} cluster for both orientations were performed starting with bent CO_2 molecules. In these calculations, the CO_2 angle, the O_{surf}–C distance, and the z coordinate of the O_{surf} were, with symmetry constraints, allowed to relax. For both orientations it was found that the CO_2 binds to a bridging O forming a carbonate. However the results were not reproduced on the $Sn_{13}O_{26}$ cluster where it was found to be only physisorbed, regardless of the fact that the initial geometry of the optimization was the carbonate one obtained from the smaller cluster, table 9.43.

Orientation	Perp.	Perp.	Para.	Para.
cluster	Sn_6O_{12}	$Sn_{13}O_{26}$	Sn_6O_{12}	$Sn_{13}O_{26}$
$r_e(CO_2)$/bohr	2.289	2.161	2.282	2.158
$\alpha_e(CO_2)/^\circ$	137	174	137	177
$r_e(O_{surf} - C)$/bohr	2.791	4.882	2.783	5.605
D_e^*/eV	0.62	0.42	0.23	-1.46
$z(O^\dagger_{surf})$/bohr	-0.064	-0.398	-0.064	-0.377

(*) All energies computed with respect to the central O_{2c} relaxed cluster

(†) Relaxation of the O_{2c} on adsorption with respect to the truncated bulk

Table 9.43: Cluster calculations of CO_2 adsorption on oxygen sites (HF results)

The energy of the Highest Occupied Molecular Orbital, HOMO, is found to change notably from one cluster to the other. The $Sn_{13}O_{26}$ HOMO is 1.57 eV more stable than in the smaller cluster. This molecular orbital has a major contribution from the bridging oxygens[5] atomic p orbitals, specifically the donor orbital p_z, that contributes mostly to the carbonate forming bond. The fact that this molecular orbital is more stable in energy implies that it is less "available" for the CO_2 molecule to form the chemical bond.

In previous sections the embedded cluster approach has been shown to be reasonably effective in bonding involving mainly electrostatic and polarization interactions. When a chemical bonding is introduced, where CT from the SnO_2 plays a major role [149] the situation is more delicate. It has just been shown that the results at the HF level depend strongly on cluster size, it remains to check if, at least, the bigger cluster is a reasonable representation, for carbonate formation on the (110) surface.

We have produced Density Of States, DOS, diagrams of both clusters and the 2L slab. In the cluster models these have been calculated from the eigenvalues of

---

[5] This has been checked on a detailed population analysis, although this was expected from the fact that these oxygens are under-coordinated.

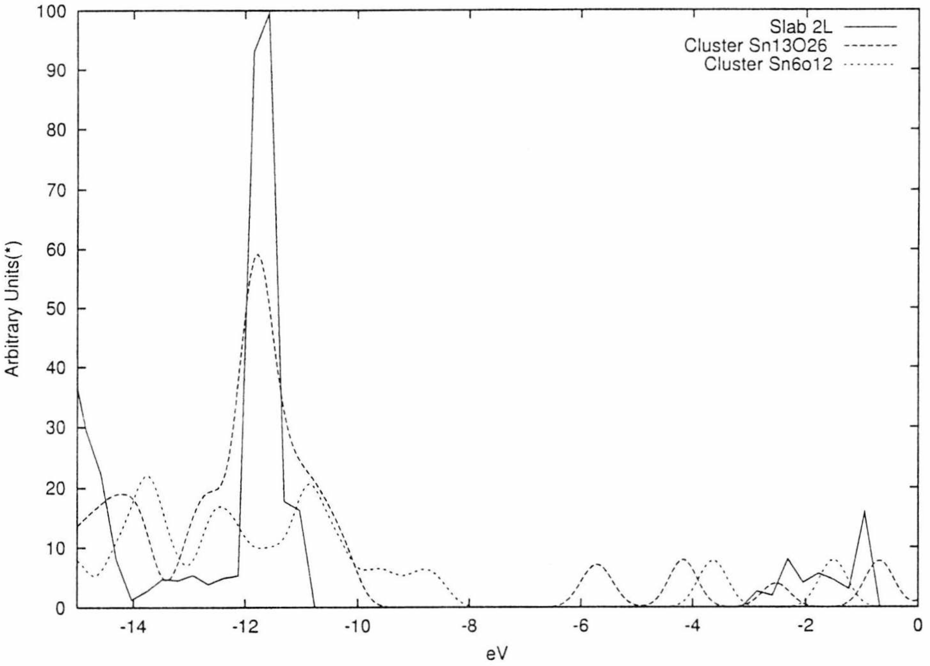

Figure 9.57: HF 2L Slab, $Sn_{13}O_{26}$ and Sn_6O_{12} DOS comparison
(*) The Slab results are rescaled by a factor of 1/9

the SCF converged wave functions multiplied by Gaussians of 0.25 eV width. In the slab model these are calculated with the Fourier-Legendre technique [151].

Considering the fact that clusters produce molecular orbitals in comparison with the 2D periodic crystalline orbitals implies that this comparison is relatively qualitative, the larger cluster and the slab in the valence bands, fig. 9.57 appear in relatively good agreement. The HOMO-LUMO gaps are for both clusters underestimated by around 50% in relation to the crystalline band gap. This probably comes from cluster border effects. No direct effect from this underestimation is expected in the binding, projection of DOS on atomic orbitals in the slab shows that the conduction band comes mostly from Sn atom, which, spatially, cannot accept charge from the CO_2 in the carbonate formation. This was further checked on the cluster, on the virtually zero contribution of the lower energy virtual molecular orbitals from the adsorbing O atom.

The data on the smaller cluster shows a preferential orientation for the formation of the carbonate on the perpendicular orientation, with a binding of 0.6 eV. The carbonate geometric parameters of both orientations are very similar.

The physisorption results shown are just presented in order to show the divergence from both clusters. They have not been confronted with periodic calculations and being at relatively high distance from the surface and with the molecule located parallel to the surface[6] are not well described, as shown on sect. 8.4.5, with a cluster model.

9.6.1.2 B3LYP results

We have performed analogous calculations at the DFT-B3LYP level. In this case the results, although certainly different, do not differ so much between clusters, table 9.44, as in the HF calculations.

For both clusters the parallel carbonate shows smaller distances and angles than the perpendicular one. However when comparing binding energies this trend disappears; while for the smaller cluster both configurations are bound with binding energies equal to 0.36 eV (parallel orientation) and 0.23 eV (perpendicular orientation), for the large cluster the binding energy is negative, so, repulsive in comparison with the separated components, and is -0.34 eV (parallel orientation) and -0.01 eV (perpendicular orientation). Really, in the smaller cluster, within the approximations of the method, a difference of 0.1 eV is rather too small (less than a typical BSSE value) to be considered. The discrepancy in the energetic results with cluster size is mainly caused by the same reason found in the HF calculations, the HOMO in the $Sn_{13}O_{26}$ cluster is more stable by 0.19 eV than in the smaller cluster. This is about one tenth of the HF difference, which explains the observed differences in binding energy but the fact that still both clusters form the carbonate.

---

[6] Calculated contour plots of the electrostatic potential field with different point charges, show quite clearly that there is a non-negligible influence of the point charges in the morphology of the field, and that this increments the further we are from the surface.

Coming back to the geometries, the distances C–O corresponding to the former CO_2 molecule, are very similar in all cases 2.322–2.358 bohr and in between the DFT values for the free CO_2 and free CO_3^{2-}, 2.203 and 2.431 bohr respectively. The O_{surf}–C bond distance is systematically higher than the obtained for the free carbonate ion and so is the OCO angle; the large cluster values are higher than for the smaller cluster (since the bond is more difficult to form and, therefore the surface carbonate should be qualitatively less similar to the free carbonate). For the large cluster, the O_{surf}–C distances are 2.703 (parallel) and 2.817 bohr (perpendicular)[7]. The angles for the large cluster are 129° and 135° for parallel and perpendicular orientations, respectively.

The relaxation of the adsorbing O_{2c} in the "free", i.e. without adsorbate, large cluster adds a change in energy amounting to 0.34 eV, this actually adds a bigger divergence in the energetic results, since the relaxation was smaller in the smaller cluster (change in energy 0.05 eV).

In summary, in the large cluster carbonate the parallel geometry is closer to the one of the free ion carbonate, however the formation is energetically slightly less favorable ~0.3 eV than the perpendicular one. Both products are metastable with respect to the free CO_2 and the clean $SnO_2(110)$ surface.

Orientation	Para.	Para.	Perp.	Perp.
cluster	Sn_6O_{12}	$Sn_{13}O_{26}$	Sn_6O_{12}	$Sn_{13}O_{26}$
$r_e(CO_2)$/bohr	2.358	2.336	2.342	2.322
$\alpha_e(CO_2)/^\circ$	127	129	130	135
$r_e(O_b - C)$/bohr	2.601	2.703	2.663	2.817
D_e^*/eV	0.36	-0.34	0.26	-0.01
$z(O_{surf})^\dagger$/bohr	0.092	-0.010	0.167	-0.096

(*) All energies computed with respect to the central O_{2c} relaxed cluster

(†) Relaxation of the central O_{2c} on adsorption with respect to truncated bulk

Table 9.44: Cluster calculations of CO_2 adsorption on oxygen sites (B3LYP results)

---

[7] In this case, the fact that the orientations are different and so are the electrostatic attractive/repulsive interactions with the rest of surface, implies that a qualitative comment cannot be done on the bond-length/strength correlation.

9.6.2 Energy barrier on the formation of carbonates

The fact that the binding energies are negative but the carbonate is in a minimum implies that this minimum must be local and consequently there must be an energy barrier. The presence of such a barrier in carbonate formation in CO_2/metal oxide systems has already been found in previous computational studies on MgO [148, 149]. It also has been shown that this barrier is not present in all oxides and even for the same oxide it depends on adsorption site [149]. As far as we know this is the first study addressing CO_2 adsorption on a rutile structure (110) surface.

We have calculated at the DFT-B3LYP level the interaction energies of CO_2 and the Sn_6O_{12} cluster[8] at different fixed O_{surf}–C distances. The full study has been restricted to the parallel orientation[9]. Some exploratory calculations have been performed as well on the perpendicular one in which, also the barrier was observed. In all the calculations the distance O_{surf}–C was fixed while the CO_2 C–O distance and angle were allowed to relax with symmetry constraints. The adsorbing, O_{surf}, atom has not been optimized, as it has been found that in the bound state is not strongly displaced from its unrelaxed position. Comparing these results with the full optimization, also, allows to show, that at least for the smaller cluster, the displacement of the adsorbing O atom does not play a significant role in the formation of the carbonate; being the energy difference only of 0.02 eV (considering the same energetic reference).

The angles decrease continuously from 180° (at 10 bohr) of the slightly bound CO_2 to the 128° of the equilibrium carbonate. The distances C–O of the CO_2 molecule show the same trend from the free CO_2 distance of 2.203 bohr to a more carbonate like value of 2.406 bohr. There is not direct correlation in the trend of this values, monotonic, and the energies obtained, non-monotonic.

The origin of the barrier in the curve becomes clear when, for each SnO_2-CO_2 distance z, the interaction energy, $E_{int}(z)$, is decomposed into the sum of two

---

[8] Although this is not the best representation of the system it is the only one computationally feasible for this study.

[9] The perpendicular orientation geometry optimization was much more difficult to converge.

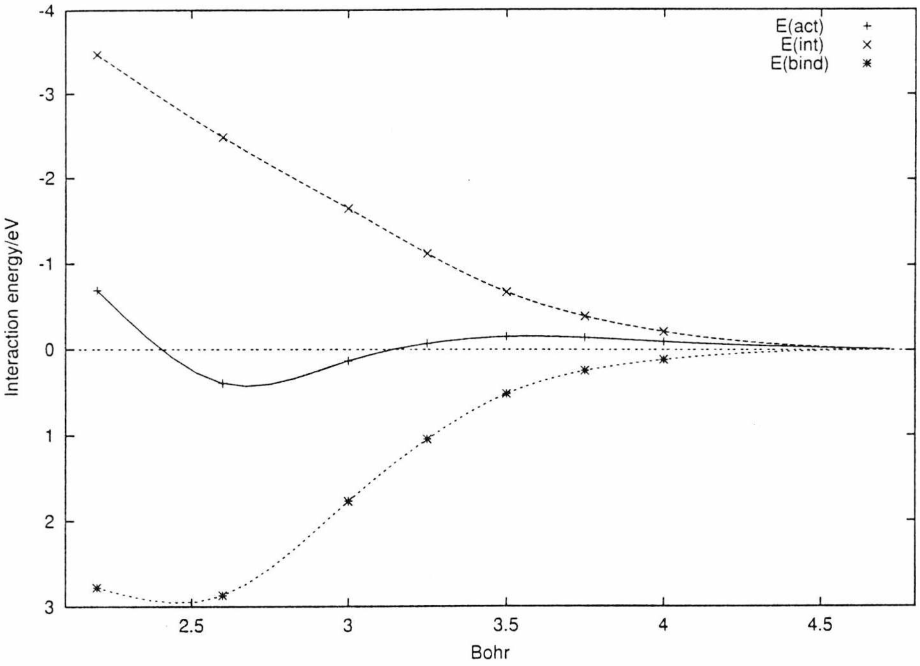

Figure 9.58: Energy decomposition of carbonate formation on oxygen sites on $SnO_2(110)$

contributions. The first term is the energy necessary to "activate" the free CO_2 molecule to form the carbonate, $E_{act}(z)$. This has been determined by computing the energy of a free CO_2 molecule with the same geometry that CO_2 assumes when it is adsorbed on the cluster for a particular distance z. The second term is the binding energy, $E_{bin}(z)$, between this "activated" CO_2 molecule and the surface, thus:

$$E_{int}(z) = E_{act}(z) - E_{bin}(z) \tag{9.59}$$

Clearly the first term, the deformation of the CO_2, is purely repulsive while the second term is attractive, at least when the surface-CO_2 distance is not too short. At very short distances in fact also the interaction between the "promoted" molecule and the surface is dominated by the Pauli repulsion. The three curves, $E_{int}(z)$, $E_{act}(z)$, $E_{bin}(z)$ are shown in fig. 9.58 and the corresponding data is shown in table 9.45.

$z_e(O_b - C)$/bohr	2.200	2.600	3.000	3.250	3.500
r_e(CO)/bohr	2.406	2.358	2.315	2.287	2.259
$\alpha(CO_2)/^\circ$	119	128	137	144	152
E_{int}/eV	0.69	-0.39	-0.13	0.07	0.15
E_{act}/eV	3.47	2.48	1.64	1.12	0.67
E_{bin}/eV	-2.78	-2.87	-1.77	-1.05	-0.52
r_e(CO)/bohr		3.750	4.000	5.000	10.000
$r_e(O_b - C)$/bohr)		2.237	2.223	2.205	2.203
$\alpha(CO_2)/^\circ$		158	164	176	180
E_{int}/eV		0.14	0.09	-0.11	-0.01
E_{act}/eV		0.39	0.21	0.01	0.00
E_{bin}/eV		-0.25	-0.12	-0.13	-0.01

Table 9.45: Energy decomposition of carbonate formation on oxygen sites on SnO_2(110)

The cost to bend and stretch the CO_2 molecule as in the surface SnO_2/CO_2 complex for $z \simeq z_e$ is about 2.5 eV. The energy gain for the interaction of this activated CO_2 molecule with the cluster is about 2.9 eV and the total result in net bonding is about 0.4 eV. Also the origin of the small barrier becomes clear from the analysis of the curve of fig. 9.58. At a surface-CO_2 distance of about 4 bohr, where the small barrier is found, the CO_2 molecule begins to bend significantly (the O–C–O angle becomes 164° and smaller) and the activation energy increases faster than the binding energy does decrease giving rise to the barrier. The activation energy for the carbonate formation process on the Sn_6O_{12} cluster is very small, around 0.2 eV. Assuming relatively similar geometries for the CO_2 activation, the binding depends mostly in the interaction with the substrate as shown by Pacchioni et al. in CaO and MgO [149].

9.6.3 Frequency calculations

We have calculated all the vibrational frequencies and IR intensities of free and adsorbed molecules at the DFT-B3LYP level with the Sn_6O_{12} and Sn_7O_{14} clusters, table 9.46. The intensities are in Km/mole. The experimental frequencies and the notation used can be found in [150].

The free molecule vibrational frequencies are very close to experiment. Even assuming intensities are good in comparison with experiment, there are certain points that have to be considered. On free CO_2 both active bands, are well documented and can be easily seen experimentally. In this cases the absorption background is flat and basically zero and the resolution depends only on concentration of CO_2. However, when we pass to a supposedly ideal solid surface the presence or absence of IR adsorbate bands will depend on concentration of adsorbate[10] as well as on the presence of substrate absorption bands on the adsorbate absorption region.

Normal Mode(Int.)	ν_1	ν_3	ν_{2a}	ν_{2b}		
	$/cm^{-1}$	$/cm^{-1}$	$/cm^{-1}$	$/cm^{-1}$		
Free CO_2 theo.	1368(0)	2415(614)	678(34)	678(34)		
Free CO_2 exp	1340	2349	667	667		
CO_2/SnO_2	1392(44)	2462(887)	667(61)	644(6)		
Normal Mode(Int.)	ν_1	ν_2	ν_{3a}	ν_{3b}	ν_{4a}	ν_{4b}
CO_3^{2-} Theo.	1008(0)	883(22)	1407(662)	1407(662)	662(0)	662(0)
CO_3^{2-} exp.	1063	879	1415	1415	680	680
SnO_2/CO_2 par.	942(14)	784(19)	1336(1)	1533(763)	633(11)	716(21)
SnO_2/CO_2 perp.	878(83)	827(0)	1310(45)	1573(43)	611(4)	519(0)

Table 9.46: CO_2 adsorbed on SnO_2 vibrational frequencies and intensities)(DFT-B3LYP results)

On the surface, physisorbed CO_2 shows a blue shift of the asymmetric stretching (ν_3) of 47 cm^{-1}; the band is intense and 44% more intense on adsorption than in free CO_2. The presence of the surface breaks the symmetry of the stretching mode (ν_1), inactive in the free molecule, and the degeneracy on the OCO bending modes modes (ν_1), resulting in relatively weak adsorptions in all cases and small shifts, to the red in the bending modes, -45–34 cm^{-1} and to the blue in the stretching mode, 25 cm^{-1}. The presence of the stretching mode in the spectrum can be used as an indicator of the CO_2 physisorbed species on SnO_2.

---

[10] The absorbance due to the adsorbate is directly proportional to the concentration of adsorbate traversed by the IR beam.

The surface carbonates show different vibrational properties when different orientations are considered. This is not surprising, since the electric field seen by the vibrating atoms must be very different in the two orientations.

Both orientations show a blue shift of more than 100 cm^{-1} in the high frequency, ν_{3b} mode, however the intensity in the perpendicular adsorption is reduced by a factor of ~150. The shift of the rest of the bands is not homogeneous, and the intensity is predicted to be generally quite low.

Experimentally, very few data have been reported. In ref [122], the authors looked at polycrystalline SnO_2 as a function of CO_2 pressure and different thermal pre-treatments of the samples, in the 1100-1800 cm^{-1} spectroscopic range. There is not information about surface morphology, sample purity or defect concentration and the frequency assignment was done based on previous assignments on *relatively* similar compounds, basically: bicarbonate, carbonate (uni and bidentate) and some typical organic group CO vibrations.

Very qualitative assignments, also, based on our results may be postulated. In the cited experimental work, regardless of thermal treatment, a weak band/s at 1430 cm^{-1} was observed that mostly disappeared in absence of CO_2 (which implies a very weak adsorption). This has been assigned to a possible bicarbonate but may be assigned as well to our calculated Sn_{5c} adsorbed CO_2, 1392 cm^{-1}. The cation is supposed to be less reactive than the oxygen, therefore it should not be affected by annealing/dehydroxilation of the surface. The assignment of bands 1375-70 cm^{-1} to carbonate agrees with our calculations (about 1310-36 cm^{-1}), the intensity of these bands do not highly depend on CO_2 pressure which suggests a chemisorpted molecule with maybe an activation energy. In contrast the band at 1585-1595, a possible carbonate as well, depends strongly on CO_2 pressure and thermal treatment indicating a different surface carbonate, or other species, less bound to the surface.

9.6.4 Periodic slab calculations

9.6.4.1 HF calculations

Cluster calculations show that at the DFT-B3LYP level, on a perfect $SnO_2(110)$ unrelaxed surface, the carbonates are formed as metastable species on top of O bridging sites. We have extended this calculation to slab models to see how coverage affects binding and to check the reproducibility of the results within a periodic approach.

In this study we have mainly used 2L slabs, which as has been shown, give an accurate description of the unrelaxed slab. At the same time, most of the studies are restricted, due to computational resources, to HF. At the HF level the molecule was not found to bind to the larger cluster, this result was reproduced on the periodic calculations, where a geometry optimization starting from a surface carbonate geometry from the smaller cluster, yielded a chemically unbound state were the CO_2 molecule was linear and at a typical physisorption distance.

Optimizations for this system are computationally very demanding due to the presence of d orbitals[11], the high number of parameters as well as the relative complexity of the parameter space[12]. We have opted in most cases for single point calculations, which, in our opinion suffice to show the point we are trying to demonstrate here.

In comparison with cluster calculations, both orientations are not indistinct, since in the parallel adsorption, coverages of θ=1 cannot be achieved due to repulsion and convergence problems due to the strong overlap of the former CO_2 O atoms (r(O–O) $\approx$2 bohr), and only a 0.5 ML is accessible for this orientation. For perpendicular orientation both, 1 and 0.5 ML, have been considered.

Preliminary calculations were done for a fixed adsorbate geometry obtained with a Sn_6O_{12} cluster geometry optimization at the HF level. The perpendicular orientation at 1 ML coverage is unbound by 1.77 eV. In order to establish if

---

[11] Gaussian d orbitals are constructed by 1 s and four p orbitals.

[12] The geometry convergence in analogous cluster systems has shown to be slow and difficult to reach

there was a minimization search problem, for instance if the optimization to the chemically unbound state was due to the presence of a rather too small barrier, and to estimate what part of the instability might come from the lack of relaxation of the molecule, a partial optimization, of only the two terminal O atoms of the adsorbed CO_2, was performed. This resulted in a carbonate-like molecule with a OCO angle of 145° and r(CO) = 2.255 bohr, this compares well with the same optimization on the bigger cluster, α=139° and r(CO)=2.278 bohr, and the smaller cluster full optimization values 137° and r(CO) = 2.289 bohr). The constrained relaxation on the slab lowered the energy by, relatively, very little, 0.18 eV.

It seems unlikely that a full geometry optimization will result in a bound state and the difference between cluster and slab calculations had to be looked for in the adsorbate-adsorbate repulsion. In order to check this we have repeated the calculations with the obtained geometry for 0.5 ML. The size of the cell has been doubled along the (100) direction, which corresponds to the direction of the rows of bridging oxygens, i.e perpendicular orientation half coverage. The repulsive interaction decreases and a binding energy of -0.78 eV per adsorbed molecule is obtained. Thus, a repulsive interaction of 0.8 eV/molecule is estimated. The coverage has been further reduced by tripling the size of the unit cell along the same direction and the interaction energy decreases only[13] to 0.62 eV. The repulsion is largely due to the fact that when CO_2 forms a surface carbonate electrons are transferred from SnO_2 to CO_2 and negative charge is localized at the O-ends of the carbonate. The fact that the large adsorbate-adsorbate repulsion is due to the negative character of the CO_3^{2-} adsorbate is shown by the calculations of an array of bent CO_2 molecules on at 1, 0.5 and 0.33 ML coverages without the SnO_2 slabs where the repulsion is 0.23, 0.03, and 0.02 eV, respectively.

The interaction is even more repulsive when CO_2 is in the parallel orientation; for 0.5 ML the interaction is -1.67 eV, for 0.33 ML -1.47 eV. This high value at a smaller coverage, is fully explained by the minimum distance between different

---

[13] The small decrease from 0.5 ML to 0.33 ML is due to the similar minimum distances between carbonates at both coverages.

adsorbed molecules which is in both cases, perpendicular 1ML and parallel 0.5 ML, reasonably similar.

A combination of both orientations simultaneously on a 2x1 slab has been tested, single point, with the same geometries used for both orientations shown in the present calculations. This yielded a repulsive energy inferior to the perpendicular and parallel cases, -1.44 eV but although less repulsive than in the mono-orientations the repulsion still dominates the binding.

Calculations at the HF level on a Sn_7O_{14} cluster with two CO_2 adsorbed molecules with the used geometries in the perpendicular orientation periodic calculations resulted on a binding energy of around -1 eV.

Geometry Orientation	Part. Opt. perp.	Fixed para.	Part. Opt. perp.	Fi pa
Supercell	Slab + CO_2	Slab + CO_2	CO_2 monolayer	CO_2 m
2L Slab 1x1	1.59	—	0.23	–
3L Slab 1x1	1.59	—	—	–
2L Slab 1x2	1.20	—	0.20	–
2L Slab 2x1	0.78	1.67	0.03	0.
2L Slab 3x1	0.62	1.47	0.02	0.
2L Slab 2x2				0.

(a x b):a. direction of the bridging oxygen rows
(a x b):b. perpendicular direction to the bridging oxygen rows
multicolumn5 l All energies in eV

Table 9.47: Carbonate formation, 2L slab calculations (HF results)

9.6.4.2 DFT-B3LYP calculations

Single point calculations have been performed also at the DFT-B3LYP level with the geometries obtained with the bigger cluster in the perpendicular orientations on (1x1) and (2x1) slabs. Although, a high level shift of the occupied bands has to be used for convergence, 1 Hartree, test calculations give an estimate of the error introduced in the energy < 0.05 eV.

The energies obtained were for the monocell and supercell, -1.13 and -0.89 eV respectively. The repulsion from 1ML to 0.5ML is much lower, around 0.3 eV, this can be rationalized from the well known characteristic of DFT with respect to HF of larger delocalization of the electronic charge.

An optimization attempt of the (1x1) perpendicular orientation carbonate formation at the DFT-B3LYP level, from the geometry obtained with the bigger cluster, was undertaken with a slab with no polarization functions[14]. The calculation of numerical gradients implies the systematic negative and positive displacement of all optimised coordinates by an user defined value, in our case 0.01 Å (0.019 bohr). The energies obtained with all single displacements were 0.1-0.2 eV higher than the input geometry strongly suggesting that this conformation is a local minimum.

9.7 Conclusions

From all the previous calculation a clear picture emerges. At the highest level of theory, in the ideal (110) surface, cluster calculations, show that, at the dilution limit although the surface carbonate may form, it forms as a metastable species and the adsorption of perpendicular CO_2 is far more stable. This metastable carbonate gets unstable at high coverages where repulsion dominates. The formation of the carbonate has been shown to depend quite strongly on the position of the Fermi level of the substrate in different models of the ideal perfect surface. It is likely that the presence of surface defects, for instance O_{2c} vacancies, will affect the position, and *availability*, of the band, making the carbonate formation reaction more favourable.

CO_2 physisorbs with its axes perpendicular to the cation. Correlation is of special importance to describe the binding, geometrically and energetically. Cluster and 0.5 ML coverage slab calculations show good agreement. At higher coverages the binding energy, distance and Surface-OCO frequencies for the CO_2 are visibly

---

[14] Single point calculation tests show a negligible energetic difference with the presence or absence of the d functions in the binding energy.

affected, the molecule binds less strongly and at a longer distance, in contrast what was found on CO. A CSOV, qualitative, HF, analysis shows that the fundamental bonding mechanism is CO_2 intra-unit polarization, explaining the sensibility of the adsorption to repulsive interactions and level of theory. The relaxation of the substrate plays a role decreasing the binding energy and, consequently, the frequencies. However the CO_2 molecule is found to bound mostly at the same distance than in the unrelaxed slab, as previously found for CO.

Part IV

Overall Conclusions and Appendices

Chapter 10

Conclusions

10.1 General remarks

In the work presented in this thesis a wide variety of computational techniques, static and dynamic, classical and quantum mechanical, have been applied in order to model different atomic processes in different materials.

Simulations of perfect bulk, defective bulk, and perfect surfaces as well as the interaction of small molecules with these surfaces have been performed. These calculations yield direct atomic information that is very useful to explain or interpret different effects and phenomena observed experimentally. All the results of the calculations have been compared with experimental results, when available. Comparisons with similar previous literature studies have been presented when considered of interest.

The work presented can be divided in two main parts (parts II and III in this thesis) based on the very different nature of the methods used for the calculations, molecular mechanics (MM) and quantum mechanical (QM) studies. In the following sections we will briefly review the most important features of the work presented.

10.2 Molecular mechanics studies

Molecular mechanics methods are much more economic computationally than quantum mechanical methods. This fact makes them very well suited for the study of relatively large systems and dynamic calculations as well as for point defects studies. However they have limited applicability and there are sources of error intrinsic to the method that cannot be directly addressed since doing so would imply performing higher level calculations, that, if feasible, could have been undertaken in the first place. The comparison with experimental results, is, consequently, of capital importance to establish the reliability of the method and the approach used in any system under study.

In the work presented in this thesis, three different kinds of systems have been studied; metal hydrides, specifically β-CaH_2 for its high conductivity, olivines, in which diffusion of metal ions is important in mechanical properties of these widely present minerals, and Cu/CeO_2, a catalyst and a very promising material for fuel cells.

The olivine diffusion studies and molecular dynamics studies of β-CaH_2 constrain the study to MM methods. In the Cu/CeO_2 case the use of MM methods is not extremely clear, mostly due to the difficulties of modeling Cu^{2+} ions with current empirical models, but the results have proved to be very valuable in interpreting most of the available experimental data and represent a good starting point for QM clustering and surface MM calculations.

Two new novel, to our knowledge, methods have been developed, coded and tested in this work. The multifit method which allows the systematical exploration, and in some cases improved, empirical potential fitting, and the Constrained Coordinate Biased Sampling (CCBS) which is a method to obtain the spatial diffusion paths of ions in asymmetric crystal structures.

10.2.1 Metal hydrides

The multifit approach has been applied to different metal hydrides to develop a completely new set of potential parameters that seems to overcome the limitations of previous parameters sets. The source of these limitations has been shown to come from a lack of flexibility of the Buckingham potential function. The results of the fitting of potentials to only very symmetric structures and properties have been shown to be not very reliable.

Results of the multifit of different hydride systems clearly justify the transferability of potentials for those system. Different potentials sets have been developed and tested in diffusion of LiH and CaH_2 yielding results that correlate very well with experiment. The very high ionic conductivity of β-CaH_2, in comparison with similar systems, seems to come mainly from a higher mobility of the species diffusing, namely the hydrogen ion.

10.2.2 Diffusion in olivines

Diffusion of cation metals in olivines is a relatively complex problem; the structure is asymmetric, there are two different crystallographic cation sites and there are many possible different linear paths between the metal cations at possible jump-diffusion distances. Saddle point energies of cation vacancy diffusion for this paths have been studied with two different methods, transition state search and CCBS, yielding the same results. The formation of vacancies on M_1 sites is much more favored than the formation on M_2 sites and most diffusion will be due to nearest neighbours M_1-M_1 jumps. However, thermodynamically M_2 vacancies have to occur in the system (and the number may be increased by a configurational entropy term[1]) and, assuming perfect single crystals, diffusion due to exchange of sites has to occur to explain the experimental observations. This diffusion,

---

[1] In this thesis only the theory concerning crystals with one anionic and one cationic site defects has been considered but its applicability to other types of crystals, like olivines, has not yet been studied and the different sites vacancy populations showed in previous chapters are very qualitative.

according with our computations, must be due to combinations of the two sites, M_1 and M_2, jump exchange paths. All these results have been obtained for fayalite but preliminary results show that same mechanisms should operate for forsterite crystals.

10.2.3 Clustering of Cu^{2+} in ceria

MM calculations have been performed in order to study the difference in configurational binding and formation energy of different copper dimers in ceria. While energetics results are not conclusive indicating that the most stable dimers involve copper interstitials, the geometries of these interstitial dimers are, conclusively, very similar to those found experimentally. In non oxidizing conditions, however, polaron compensated Cu^{2+} interstitials are expected to dominate, but in this case, the clustering energy and the higher number of forming defects per dimer/cluster hinders the clustering (as observed experimentally). The interstitial site has been shown also to be the more energetically stable for Cu in strongly reducing conditions.

10.3 Quantum mechanics studies

We have studied quantum mechanically the SnO_2 (110) surface and its interaction with CO and CO_2. This is the most thermodynamically stable surface of rutile structured tin oxide. This material is of capital importance as a reducing gases sensor and catalyst. The present study is mostly a preliminary study towards simulations more relevant to the technological applications of this material.

In most cases[2] the interaction of molecules with surfaces is studied by quantum mechanical methods. There are different contributions of the bonding of electronic nature, that *a priori*, cannot be easily modeled by atomistic, i.e. MM, methods. Quantum mechanical methods in scalar, i.e. non parallel, computers can only be

---

[2] But not all, for instance [152].

applied to systems with a small number of atoms (in our case the maximum was 42). In order to study surface coverage effects two different approaches, cluster and periodic slabs under the LCAO approach, have been used, and the results for both models have been systematically compared. Different Hamiltonians, uncorrelated (HF) and correlated (MP2 and/or DFT-B3LYP) have been used in all interesting cases.

10.3.1 SnO_2 (110) surface

B3LYP bulk periodic calculations have reproduced very well the experimental bandgap of SnO_2. Relaxation of the surface has been studied at the HF and B3LYP levels on different thickness slabs models and has been found to be qualitatively different for both Hamiltonians. The smaller representation of the surface with a truncated bulk slab corresponds to a slab of 6 atomic layers. The smaller representation of a relaxed slab corresponds to a slab of 9 atomic layers.

10.3.2 CO on SnO_2 (110)

Correlated and uncorrelated Hamiltonians yielded very similar results for CO molecules on pentacoordinated Sn ions of clusters and slabs. Although DFT binding energies were found to be systematically lower than HF, the obtained geometries were very similar, this similarity comes from the electrostatic nature of the bonding. The binding energy has been shown not to depend strongly on the values of the clusters point charges affirming the validity of the method for this systems. The repulsion between adsorbed CO molecules has been found to be rather weak at the maximum coverage. The bonding and vibrations of adsorbed CO have been analyzed by decomposing the interaction energy into the sum of various contributions (CSOV analysis). This analysis shows that the interaction of CO with the five-coordinated Sn ions of the surface has a large electrostatic character reinforced by a substantial donation of charge from CO to the cation. Relaxation plays a role in the adsorption, decreasing the binding energy and the frequency shift, however the CO binds virtually at the same distance with respect to a virtual unrelaxed layer. The CO adsorption is, at all levels, rather weak but is accompanied by a large shift of the vibrational frequency towards higher values.

10.3.3 CO_2 on SnO_2 (110)

Cluster calculations at the highest level of theory (DFT-B3LYP) in the ideal (110) surface show that at the dilution limit although the surface carbonate may form, it forms as a metastable molecule and the adsorption of perpendicular CO_2 is more energetically likely. The metastable carbonate becomes unstable at high coverages where repulsion dominates. The formation of the carbonate has been shown to depend quite strongly on the position of the Fermi level of the substrate of different models of the ideal perfect surface. It is likely that the presence of surface defects, for instance O_{2c} vacancies, will affect the position, and *availability*, of the band, making the carbonate formation reaction more favorable.

CO_2 physisorbs with its axes perpendicular to the cation. Correlation is of special importance to describe the binding, geometrically and energetically. Cluster and 0.5 ML coverage slab calculations show good agreement. At higher coverages the binding energy, distance and Surface-OCO frequencies for the CO_2 are visibly affected, the molecule binds less strongly and at a longer distance, in contrast what was found on CO. A CSOV, qualitative, HF, analysis shows that the fundamental bonding mechanism is CO_2 intra-unit polarization, explaining the sensibility of the adsorption to repulsive interactions and level of theory. The relaxation of the substrate plays a role decreasing the binding energy and, consequently, the frequencies. However the CO_2 molecule is found to bound mostly at the same distance than in the unrelaxed slab, as previously found for CO.

10.4 Concluding remarks

The presented work in this thesis shows the high degree of sophistication of different computational methods and codes and how these can be applied to very specific problems in materials chemistry and physics.

The computer simulations presented are a very powerful tool to help interpreting experimental data and to gain direct insight in some of the atomic processes that rule the behaviour and properties of complex materials.

Appendix A

Soft Modes on the Rutile (110) Surface

Although there is not any experimental measure of the relaxation of the $SnO_2(110)$ surface to compare the results of our calculations with, this information is available for the isostructural $TiO_2(110)$ [153].

In $TiO_2(110)$, computational DFT periodic high quality calculations by two different methods by Harrison et al. [125] at best underestimated by 0.1 Å the experimentally found displacement on the bridging oxygens. This underestimation by QM calculations is quite systematic as shown by previous studies, see sect. 7.2.4.1.

In the same work, the authors, *postulated* this as coming from a possible very soft mode for the bridging oxygen that would imply a highly anisotropic vibration and displacements of ~0.15 Å at room temperature. The strong difference in the bridging oxygen position as a function of other atoms relaxation, in our case for $SnO_2(110)$, may well be an exponent of this. The presence of such a mode gives raise to very interesting points:

- Model optimization problems: if the curve is very flat a far away position from the minimum can be considered as the minimum one, since the gradient at this position may be already quite low.

- Experimental data analysis problems: most structure determination software assumes isotropic (thermal and configurational) Debye-Waller factors. A high anisotropy may affect strongly the results of the analysis.

- The static approximation may not be completely adequate for the modeling of such oxides, and calculations considering vibrations and consequently thermal effects might be necessary[1].

In order to further clarify this and to have an estimate of the same effect on $SnO_2(110)$. We have classically studied with the package MARVIN [154] TiO_2 and $SnO_2(110)$ surface relaxations with different sets of potentials and different, shell and rigid ion, models obtaining relaxation displacements in reasonable agreement with other computational methods. Specifically, in the TiO_2 case one of the potentials chosen, Matsui et al. [155], has been widely used in classical simulations of $TiO_2(110)$ surface, see [156] and therein, with results in fair agreement with the rest of theoretical techniques.

We have then extended, always under the classical approach, in an analogous manner, the calculation of Harrison et al. [125] of the potential well of bridging oxygen to each atom in the first 2 atomic layers in all the surface relaxation directions.

In order to calculate this, a full, symmetry constrained, minimization of the rest of the slab[2] is done at different fixed positions on the relaxation directions of each atom. It is important to notice that this although approximating somehow the part of the vibrational modes of the corresponding atoms that occurs in the given direction, it can only suggest the presence of the soft mode. For instance in this method, the motions of all surface atoms in the periodic slab is completely correlated. So effectively, in the case of bridging O atoms, we are taking away from the surface at the same time all the atoms. This without any doubt, is a

---

[1] The minimum of energy may not be the most, static (i.e. time averaged), representative position of the atom.

[2] Actually, our classical calculations were not done in slabs, but assuming certain thickness of slab the methods should be completely equivalent.

sampling of the relaxation curve as a function of the displacement of the atoms, but might be far from the thermal vibrational "sampling" the occurs in the real system.

As, what it may be an exponent of this, all our results, independently of modél, potential and system, show not only a soft mode in the bridging oxygens but also a soft mode, slightly softer on the basal O for both relaxing directions y and z. There are not any general systematic discrepancies of the experiment with theoretical methods for that basal oxygen.

For the SnO2 (110), as shown by the divergence in the HF/DFT bridging oxygen displacement, the interactions involving the bridging oxygens seem to be quite sensitive to the calculation method and the reliability of empirical interatomic potentials for this interaction and, more generally, for this systems, may need to be carefully assessed before continuing.

We believe that the existence of the flat potential wells may not be specifically connected with the presence of a soft mode. Although, still further testing has to be conduced, and the work, is still in a fairly preliminary stage, this theory is supported by the MD calculations on $TiO_2(110)$ slabs by San Miguel at al. [156], in comparison with molecular mechanics static calculations on the same material and with the same potentials, that do not show any considerable divergence in the positions of any of the O atoms. We intend to check further this in more focused MD simulations.

Appendix B

Experimental Structures Selection Criteria

All the structures used in our studies were obtained from Daresbury's Inorganic Crystallographic Structure Database, ICSD. In this database, the compounds are indexed at various levels and can be retrieved based on different combined criteria. Good comprehension if its use has proved to be extremely useful for the development of potentials, specifically in the work of hydrides.

From database search results, in many cases, there is more than one experimental structure determination for the crystallographic phase of the same compound, and although generally, as expected, the results do not differ much, since, at least ideally, they are expressions of the same physical reality, they are not completely equivalent (since the quality of data yielded by various techniques, samples and analysis methods is intrinsically different).

The selection of the structure is only relevant on the derivation of empirical potentials and on any QM calculation where the structure is not optimized. Although our knowledge of crystallography is very limited, we have used some thumb rules to choose structures:

- Since all the simulations where structure selection is crucial fall under the static, 0 K approximation, ideally the lower the experiment temperature the better.

- Also neutron diffraction data if possible is preferred. Neutrons are scattered by the nuclei and not by the electronic distribution (like X-rays).
- Single crystals are preferred than powder (less experimental uncertainties, for instance packing dependence).
- X-ray synchrotron source (more intensity of radiation).
- Synthetic materials are preferred than mineralogical samples (*a priori* purer and, in most cases, annealed).

Appendix C

Static Comparison of Metal Hydrides-Deuterides?

Hydrogen and deuterium are isoelectronic and have the same nuclear charge, so the static interaction under the Born-Oppenheimer principle H-H and D-D should be exactly the same. Since they only differ in mass only dynamic properties and properties that have a dynamic contribution will be affected. In a static calculation this would mean, low frequency dielectric constant (since it has a nuclear and electronic contribution) and phonons.

There has been a serious of papers, [46, 54, 55], where, statically, defects and diffusion activation energies for NaH, LiH, NaD and LiD have been calculated. The real, free energy, defects energetics should be expected to be different, since the entropic vibrational contributions are different (so are the vibrational frequencies), and it would be interesting to see how much properties change, or are predicted to change by the model. Experimentally the change is rather small. For instance the LiD Schottky defect energy is higher than the LiH one by only 0.1 eV [54], presumably coming from the more rigid anion sublattice.

However, on the cited works, calculated energies are configurational and are, extremely similar between hydrides and deuterides[1], and the Schottky formation

---

[1] The only difference in the model coming from the different dielectric constant, that affects the polarization of region IIb and the screening of region IIa.

energy found for LiD is lower. This clearly shows, that the application of static methods to calculate variations on properties of systems due to an isotopic substitution is not at all adequate, and MD simulations are necessary for the good evaluation of the difference.

Appendix D

Relative Defect Population as a Function of Configurational Energies

The concentration of defects follows a Boltzmann distribution, sect. 3.1.3. The relative concentration of two defects involving the same species distributed on two crystallographic sites, independently of the form of the associated defect, and assuming the entropy of both isolated defects[1] to be either zero or very similar in both sites, give us, in both cases, the next equation:

$$\frac{c_{(site_2)}}{c_{(site_1)}} \simeq exp\left(\frac{E_{(site_1)} - E_{(site_2)}}{kT}\right) \tag{D.60}$$

---

[1] The variation of entropy due to one isolated defect can be understood as how the vibrations of the nearest neighbours atoms are affected by its presence. For instance, the atoms bordering a vacancy should vibrate more slowly than perfect bulk atoms since their restoring force in the direction of the vacancy is more reduced, while frequencies around an interstitial should be increased by its presence [28].

Appendix E

Hardware

The calculations presented in this thesis have been performed in a variety of machines:

- Molecular mechanics static calculations have been performed in Sun, Linux (AMD, PII, dual PIII) and Silicon Graphics Octane workstations.
- Molecular mechanics dynamic calculations have been performed in Daresbury's laboratory IBM-SP2.
- Quantum mechanical cluster calculations have been performed in IBM powerPC R6000, IBM (dual R6K power3 II) and Linux (PI, dual PIII) workstations.
- Quantum mechanical periodic calculations have been performed in IBM (dual R6K power3 II) and Linux (dual PIII) workstations as well as in the Compaq Alphaservers cluster at the Rutherford-Appleton laboratory.

Bibliography

[1] M.P Allen and D.J. Tildesley, Computer Simulation of Liquids, (Clarendom 1987).

[2] G.C. Maitland, Intermolecular Forces (Clarendon 1981).

[3] M.J. Sanders, M. Leslie and C.R.A. Catlow, J. Chem. Soc. Chem. Comm. (1984) 1271.

[4] M. Matsui and G.D. Price, Phys. Chem. Min. 18 (1992) 365.

[5] N.F. Mott, M.J. Littleton, Trans. Faraday Soc., 34 (1938) 389.

[6] B.G. Dick and A.W. Overhauser, Phys. Rev. B 112 (1958) 90.

[7] A.M. Stoneham, Physica B & C 131 (1985) 69.

[8] J.D. Gale Phys. Mag. B 73 (1996) 3.

[9] J.D. Gale J. Chem. Soc. Faraday Trans. 4 (1997) 629.

[10] J.D. Gale, GULP 1.2 Manual (1999).

[11] C.R.A. Catlow and W.C. Mackrodt, Computer Simulation of Solids (Lecture notes in Physics, vol 166, Springer, Berlin 1982).

[12] W. J. Hehre, L. Radom, P.V.R. Shleyer and J.A. Pople, Ab initio molecular orbital theory (John Wiley & Sons, 1986).

[13] E.J. Baerends and O.V. Gritsenko, J. Phys. Chem. 100 (1996) 12974.

[14] P. Hohemberg and W. Kohn, Phys. Rev. B. 136 (1964) 864.

[15] W. Kohn and L.J. Sham, Phys. Rev. A 140 (1965) 1133.

[16] A.D. Becke, J. Chem. Phys. 98 (1993) 5648.

[17] C. Lee, W. Yang, and R.G. Parr, Phys. Rev. B 37 (1988) 785.

[18] S. Boys and F. Bernardi, Mol. Phys. 19 (1970) 553.

[19] A. Devita, M.J. Gillan, J.S. Lin, M.C. Payne, I. Stich, L.J. Clarke , Phys. Rev. Lett. 68 (1992) 3319.

[20] R. Dovesi, V.R. Saunders, C. Roetti, M. Caus, N.M. Harrison, R. Orlando, and E. Aprá, CRYSTAL98 User's Manual (Universitá di Torino, Torino 1996).

[21] G. Pacchioni, in: Point defects in SiO_2, G. Pacchioni and L. Skuja (Eds.), NATO ASI Series E, in press (Kluwer, Dordrecht 2000).

[22] D. Ricci, D. Erbetta and G. Pacchioni, submitted (2000).

[23] M.A. Nygren, L.G.M. Pettersson, Z. Barandiaran, and L. Seijo, J. Chem. Phys. 100 (1994) 2010.

[24] G. Pacchioni, in: Chemisorption and Reactivity on Supported Clusters and Thin Films, R.M. Lambert and G. Pacchioni (Eds.), NATO ASI Series E, 395 (Kluwer, Dordrecht 1997) 331.

[25] M. Dupuis, F. Johnston and A. Marquez, HONDO 8.5 for CHEMStation (IBM Co., Kingston 1994).

[26] Gaussian 98, M.J. Frisch, G.W. Trucks, H.B. Schlegel, G.E. Scuseria, M.A. Robb, J.R. Cheesman, V.G. Zakrzewski, J.A. Montgomery, R.E. Stratmann, J.C. Burant, S. Dapprich, J.M. Millam, A.D. Daniels, K.N. Kudin, M.C. Strain, O. Farkas, J. Tomasi, V. Barone, M. Cossi, R. Cammi, B. Mennucci, C. Pomelli, C. Adamo, S. Clifford, J. Ochterski, G.A. Petersson, P.Y. Ayala,

Q. Cui, K. Morokuma, D.K. Malick, A.D. Rabuck, K. Raghavachari, J.B. Foresman, J. Cioslowski, J.V. Ortiz, B.B. Stefanov, G. Liu, A. Liashenko, P.Piskorz, I. Komaromi, R. Gomperts, R.L. Martin, D.J. Fox, T. Keith, M.A. Al-Laham, C.Y. Peng, A. Nanayakkara, C. Gonzalez, M. Challacombe, P.M.W. Gill, B.G. Johnson, W. Chem, M.W. Wong, J.L. Andres, M. Head-Gordon, E.S. Repogle, and J.A. Pople, (Gaussian Inc., Pittsburgh, PA 1998).

[27] A.V. Chadwick, Ionic Conduction and Diffusion in Solids, Encyclopedia of Applied Physics 193 (VCH Publihers 1994) 8.

[28] A.B. Lidiard, Ionic Conductivity, Handbuch der Phisik, 246 (Springer Verlag, Berlin 1957) 20.

[29] A.R. West, Solid State Chemistry and its Applications (John Wiley & Sons 1984).

[30] T.S.Bush, J.D.Gale, C.R.A.Catlow and P.D. Battle, J. Mater Chem. 4 (1994) 831.

[31] G.G. Libowitz, Solid-State Chemistry of Binary Metal Hydrides (Benjamin, New York 1965).

[32] Thermodynamic Properties of Individual Substances: Handbook, Vol. 3, Book 1 (Nauka, Moscow 1981).

[33] V.P. Gorelov and F. Pal'guev, Soviet Electrochemistry (English edition) 28 (1992) 1294.

[34] M. Faraday, Faraday's Diaries 1820-1862 Vol II (G. Bell, London).

[35] M.J. Gillan, J. Physics C. 19 (1986) 3517.

[36] N.T. Wilson, M. Wilson, P.A. Madden and N.C. Pyper, J. Chem. Phys. 105 (1996) 11209.

[37] Chung-Yun Xiao, Jin-Long Yang, Kai-Ming Deng, Zu-He Bian and Ke-Lin Wang, J. Phys. Condens. Mat. 6 (1994) 8539.

[38] I. Baraille, C. Pouchan, M. Causa and C. Pisani, Chem. Phys. 179 (1994) 39.

[39] N.G. Alexandropoulos, I. Theororidou and M.J. Cooper, J. Phys. C. 20 (1987) 1201.

[40] I. Theororidou and N.G. Alexandropoulos, Z. Phys. B, 54 (1984) 22.

[41] J. Bergsma and B.O. Loopstra, Act. Cryst. 15 (1962) 92.

[42] G.C. Shull, E.O. Mollan, G.A. Morton and W.L. Davidson, Phys. Rev. 73 (1948) 842.

[43] R.S. Calder, W. Cochram, D. Griffiths and R.D. Lowde, J. Phys. Chem. Solids 23 (1962) 621.

[44] F.H. Ellinger, C.E. Holley, B.B. McInteer, D. Pavone, R.M. Potter, E. Staritzky and W.H. Zacharsiasen, J. Am. Chem. Soc. 77 (1955) 2647.

[45] G.J. Snyder, H. Borrman and A. Simon, Zeitschrift fuer Kristallographie 209 (1994) 458.

[46] E. Haque and A.K.M.A. Islam, Phys. Stat. Sol. 158 (1990) 457.

[47] M. Melle-Franco, M.Sc. Thesis, University of Kent (1997).

[48] T.S.Bush, C.R.A.Catlow and P.D. Battle, J. Mater. Chem. 5 (1995) 1269.

[49] S.M. Woodley, P.D. Battle, J.D.Gale and C.R.A.Catlow, Phys. Chem. Chem. Phys. 1 (1999) 2535.

[50] G.D. Barrera, M.B. Taylor, N.L, Allan, T.K.H.Barron, L.N. Kantorovich and W.C. Mackrodt, J. Chem. Phys. 107 (1997) 4337.

[51] R. Pandey and A.M. Stoneham, J. Phys. C. 18 (1982) 5289.

[52] C.R.A. Catlow, K.M. Diller and M.J. Norgett, J. Phys. C, 10 (1977) 1395.

[53] C.R.A. Catlow, M.J. Norgett and T.A. Ross, J. Phys. C, 10 (1977) 1627.

[54] E. Haque and A.K.M.A. Islam, J. Phys. Chem. Sol. 53 (1992) 377.

[55] A.K.M.A. Islam, J. Phys. Chem. Sol. 55 (1994) 517.

[56] M. Ikeya, J. Phys. Soc. of Japan 42 (1977) 168.

[57] F.E. Pretzel and C.C. Rushing, J. Phys. Chem. Sol. 17 (1961) 232; F.E. Pretzel et al., J. Phys. Chem. Sol. 16 (1960) 10.

[58] P.A. Varotsos and S Mouriksis, Phys. Rev. B 10 (1974) 5220.

[59] K. Funke and H. Richtering, Ber Bunsenges Phys. Chem. 72 (1968) 619.

[60] F.A. Kröger, The chemistry of imperfect crystals (North-Holland 1974).

[61] G. Vineyard, J. Phys. Chem. Sol. 3 (1957) 157.

[62] J. Brice, A. Courtois and J. Aubry, J. Sol. St. Chem. 24 (1978) 381.

[63] P. Ehrlich, B. Alt and L. Gentsch, Zeitschrift fuer Anorganische und Allgemeine Chemie 283 (1956) 58.

[64] E. Zintl and A. Harder, Zeitschrift fuer Elektrochemie 33 (1935) 41.

[65] R. Leveque, M. Zanne, D. Vergnat-Grandjean and J. Brice, J. Sol. St. Chem, 33 (1980) 233.

[66] W. Smith and T. Forester, J. Molec. Graphics 14 (1996) 136.

[67] M.J. Gillan, Sol. St. Ion. 166 (1982) 275.

[68] K. Wright and G.D. Price, J. Geophys. Res., 22245 (1993) 98.

[69] R.A. Jackson and C.R.A. Catlow, Mol. Sim. 1 (1988) 207.

[70] G.W. Watson, Ph.D. Thesis, University of Bath (1996).

[71] G.V. Lewis and C.R.A. Catlow, J. Phys. C. 18 (1985) 1149.

[72] S. Wiβmann and K.D. Becker, submitted (2000).

[73] D.K. Buening and P.R. Buseck, J. Geoph. Res. 78 (1973) 6852.

[74] T.L. Tsai and R. Dieckmann, Mater. Sci. Forum 239 (1997) 399.

[75] K.D. Becker, Dreher S. and Wiβmann, Ber. Bunsenges. Phys. Chem. 96 (1992) 1778.

[76] R. Dieckmann, J. Phys. Chem. Sol. 59 (1998) 507.

[77] J. Brodholt, Amer. Mineralogist 82 (1997) 1049.

[78] M. Miyamoto and H. Takeda, Nature 303 (1983) 602.

[79] A. Trovarelli, Catalysis Rev.-Sci. & Eng. 38 (1996) 439.

[80] J.A. Rodriguez, T. Jirsak, A. Freitag, J.C. Hanson, J.Z. Larese and S. Chaturvedi, Cat. Lett. 62 (1999) 113.

[81] P. Bera, S.T. Aruna, K.C. Patil and M.S. Hedge, J. Catal. 186 (1999) 36.

[82] D. Courcot, E. AbiAad, S. Capelle and A. Aboukais, Stud. Surf. Sci. Catal. 116 (1998) 625.

[83] E.P. Murray, T. Tsai and S.A. Barnett, Nature 400 (1999) 649.

[84] S.D. Park, J.M. Vohs and R.J. Gorte, Nature 404 (2000) 265.

[85] A. Aboukais, A. Galtayries, E. AbiAad, D. Courcot, and J. Grimblot, Coll. Surf. A 154 (1999) 335.

[86] A. Aboukais, A. Bennani, C.F. Aissi, G. Wrobel, M. Guelton and J.C. Vedrine, J. Chem. Soc. Faraday Trans. 88 (1992) 615.

[87] S. Gennard, F. Cora and C.R.A. Catlow, J. Phys. Chem. B 103 (1999) 10158.

[88] J. Andres and A. Beltran, Chem. Phys. Lett. 221 (1994) 249.

[89] T.X.T. Sayle, C.R.A. Catlow, D.C. Sayle, S.C. Parker and J.H. Harding, Phis. Mag. A 68 (1993) 565.

[90] G. Balducci, M.S. Islam, J. Kapar, P. Fornasiero and M. Graziani, Chem. Mat. 12 (2000) 677.

[91] H. Inaba, R. Sagawa, H. Hayashi and K. Kawamura, Sol. St. Ion. 122 (1999) 95.

[92] L. Minervini, M.O. Zagate and R.W. Grimes, Sol. St. Ion. 116 (1999) 339.

[93] G. Balducci, M.S. Islam, J. Kapar, P. Fornasiero and M. Graziani, J. Phys. Chem B 102 (1998) 557.

[94] G. Balducci, M.S. Islam, J. Kapar, P. Fornasiero M. Graziani and J.D. Gale, J. Phys. Chem B 101 (1997) 1750.

[95] A.K.A. Pryde, S. Vyas, R.W. Grimes, J.A. Gardner and R.P. Wang, Phs. Rev. B 52 (1995) 13214.

[96] D.C. Sayle, T.X.T. Sayle, S.C. Parker and C.R.A. Catlow, Surf. Sci. 334 (1995) 170.

[97] J.C. Conesa, Surf. Sci. 339 (1995) 337.

[98] T.X.T. Sayle, S.C. Parker and C.R.A. Catlow, J. Phys. Chem. 98 (1994) 13625.

[99] T.X.T. Sayle, S.C. Parker and C.R.A. Catlow, Surf. Sci. 316 (1994) 329.

[100] S. Ling, Phys. Rev. B 49 (1994) 864.

[101] S.B. Adler and J.W. Smith, J. Chem. Soc. Faraday Trans. 89 (1993) 3123.

[102] A.D. Murray, G.E. Murch, C.R.A. Catlow, Sol. St. Ion. 98 (1986) 196.

[103] R.C. Baetzold, Mol. Sim. 12 (1994) 77.

[104] M. Leslie, SERC Daresbury Report, DL/SCI/TM3IT SERC Daresbury Laboratory (1982).

[105] A. Aboukais, personal communication.

[106] P.A. Cox, The Electronic structure and Chemistry of Solids (Oxford Science Publication, Oxford 1987).

[107] S.M. Woodley, personal communication.

[108] A.A. Bolzan, C. Fong, B.J. Kennedy, and C.J. Howard, Actaa Cryst. B 53 (1997) 373.

[109] D. Fröhlich, R. Klenklies and R. Helbig, Phys. Rev. Lett. 41 (1978) 1750.

[110] J. Goniakovski, J.M. Holender, L.N. Kantorovich, M.J. Gillan and J.A. White, Phys. Rev. B 53 (1996) 957.

[111] T.T. Rantala, T.S. Rantala, and V. Lantto, Surf. Sci. 420 (1999) 103.

[112] M. Ramamoorthy, D. Vanderbilt, and R.D. King-Smith, Phys. Rev. B 49 (1994) 16721.

[113] D.C. Sorescu and J.T. Yates, Jr., J. Phys Chem. B. 102 (1998) 4556.

[114] W.R. Wadt and P.J. Hay, J. Chem. Phys. 82 (1985) 284.

[115] S. Huzinaga (Ed.), Gaussian Basis Sets for Molecular Calculations (Elsevier, Amsterdam 1984).

[116] R. Ditchfield, W.J. Hehre, and J.A. Pople, J. Chem. Phys. 54 (1971) 724.

[117] V.E. Henrich and P.A. Cox, The Surface Science of Metal Oxides (Cambridge University Press, Cambridge 1994).

[118] P.A. Mulheram and J.H. Harding, Mol. Sim. 39 (1992) 1.

[119] P.W. Tasker, J. Phys. C 12 (1979) 4977.

[120] I. Manassidis, J. Goniakovski, L.N. Kantorovich, and M.J. Gillan, Suf. Sci. 339 (1995) 258.

[121] M.C. Payne, M.P. Teter, D.C. Allan, T.A. Arias and J.D. Joannopoulos, Rev. Mod. Phys 64 (1992) 1045.

[122] F.H. Jones, R. Dixon, J.S. Foord, R.G. Edgell and J.B. Pethica, Surf. Sci 376 (1997) 367.

[123] M. Calatayud, J. Andrs, and A. Beltran, Surf. Sci. 430 (1999) 213.

[124] T. Bredow, E. Aprá, M. Catti, G. Pacchioni, Surf. Sci. 418 (1998) 150.

[125] N.M. Harrison, X.G. Wang, J. Muscat and M. Scheffler, Faraday Discuss. 114 (1999) 305.

[126] M.I. Zaki and H. Knözinger, J. Catal. 119 (1987).

[127] G. Pacchioni, A.M. Ferrari and P.S. Bagus, Surf. Sci. 350 (1996) 159.

[128] F.J. van Duijneveldt, IBM Res. Rep. RJ 945 (1971).

[129] G. Pacchioni, G. Cogliandro, and P.S. Bagus, Surf. Sci. 255 (1991) 344.

[130] G. Pacchioni, G. Cogliandro, and P.S. Bagus, Int. J. Quant. Chem. 42 (1992) 1115.

[131] T. Bredow, G. Pacchioni, Surf. Sci., 373 (1997) 21.

[132] T. Bredow, A.M. Marquez, and G. Pacchioni, Surf. Sci. 430 (1999) 137.

[133] See articles in: The Surface Science of Metal Oxides, Faraday Discuss. 114 (1999).

[134] H.J. Freund, Faraday Discuss. 114 (1999) 1.

[135] H.J. Freund, H.K. Kuhlenbeck, and V. Staemmler, Rep. Prog. Phys. 59 (1996) 283.

[136] R.M. Lambert and G. Pacchioni (Eds.), Chemisorption and Reactivity on Supported Clusters and Thin Films, NATO ASI Series E, Vol. 331, (Kluwer, Dordrecht 1997).

[137] C. Otero Arean, A.A. Tsyganenko, E. Escalona-Platero, E. Garrone, and A. Zecchina, Angew. Chem. Int. Ed. 37 (1998) 3161.

[138] P.S. Bagus, K. Hermann and C.W. Bauschlicher, J. Chem. Phys. 80 (1984) 4378.

[139] P.S. Bagus and F. Illas, J. Chem. Phys. 96 (1992) 8692.

[140] P.J.D. Lindan, J. Muscat, S. Bates, N.M. Harrison, and M. Gillan, Faraday Discuss. 106 (1997) 135.

[141] A.M. Marquez, N. Lopez, M. Garcia-Hernandez, and F. Illas, Surf. Sci. 442 (1999) 463.

[142] C. Pisani, R. Dovesi and C. Roetti, in: Hartree-Fock Ab-initio Treatment of Crystalline Systems, Lecture Notes in Chemistry, Vol. 48, (Springer, Heidelberg, 1988).

[143] G. Pacchioni, K. Neyman, N. Röosch, J. El. Spectr. Rel. Phen. 69 (1994) 13.

[144] K. Taneba, Catalysis-Science and Technology (Springer, Berlin, 1981).

[145] M. Ai, J. Catal. 54 (1978) 223.

[146] H.H. Kung, Transition Metal Oxides: Surface Chemistry and Catalysis (Elsevier, Amsterdam, 1989).

[147] P.G. Harrison and B.M. Maunders, J. Chem. Soc. Faraday Trans. 80 (1984) 1357.

[148] G. Pacchioni, Surf. Sci. 281 (1993) 207.

[149] G. Pacchioni, J.M. Ricart and F. Illas, J. Am. Chem. Soc. 116 (1993) 10152.

[150] G. Herzberg, Molecular Spectra and Molecular Structure Vol. 1 (Van Nostrand, Princeton 1950).

[151] C. Pisani, E. Apra and M. Causa, Int. J. Quantum Chem. 38 (1990) 395.

[152] S.C. Parker, N.H. deLeeuw and S.E. Redfern, Faraday Discuss. 114 (1999) 381.

[153] G. Charlton, P.B. Howes, P. Steadman, J.S.G. Taylor, C.A. Muryn, S.P. Harte, J. Mercer, R. McGrath, D. Norman, T.S. Turner, G. Thornton, Phys. Rev. lett. 78 (1997) 495.

[154] D.H. Gay and A.L. Rohl, J. Chem. Soc. Faraday Trans. 915 (1995) 925.

[155] M. Matsui and M. Akaogi, Mol. Sim. 6 (1991) 239.

[156] M.A. San Miguel, C.J. Calzado and Javier Fdez. Sanz, Surf. Sci. 409 (1998) 92.